Acoustic Metamaterials and The Angular Momentum of Sound

by

Chengzhi Shi

A dissertation submitted in partial satisfaction of the

requirements for the degree of

Doctor of Philosophy

in

Engineering - Mechanical Engineering

in the

Graduate Division

of the

University of California, Berkeley

Committee in charge:

Professor Xiang Zhang, Chair
Professor Oliver M. O'Reilly
Associate Professor Chris Dames
Assistant Professor James Analytis

Spring 2018

Acoustic Metamaterials and The Angular Momentum of Sound

Copyright 2018
by
Chengzhi Shi

Abstract

Acoustic Metamaterials and The Angular Momentum of Sound

by

Chengzhi Shi

Doctor of Philosophy in Engineering - Mechanical Engineering

University of California, Berkeley

Professor Xiang Zhang, Chair

Acoustic metamaterials are artificial materials designed to realize unprecedented properties such as super-resolution imaging, asymmetric wave transport, cloaking, etc. The critical material parameters considered for the design of acoustic metamaterials are mass density and bulk modulus. Previous studies have demonstrated the existence of acoustic metamaterials with negative effective mass density and/or bulk modulus. In this thesis, the realization of acoustic metamaterials with extreme materials parameters including simultaneous zero effective mass density and infinite bulk modulus as well as complex-valued parameters is discussed. Metamaterials with simultaneous zero density and infinite bulk modulus exhibit zero refractive index properties called acoustic double zero index metamaterials in which the propagating sound wave has an infinite phase velocity. This infinite phase velocity results in an infinite wavelength, such that the propagating acoustic wave has a uniform phase inside the metamaterial, which can be used for the realization of acoustic wave tunneling and collimation. Our designed acoustic double zero index metamaterial is induced by a Dirac-like cone dispersion at the Brillouin zone center associated with triply degenerated monopolar and dipolar modes. The monopolar and dipolar modes induce an infinite bulk modulus and a zero mass density, respectively. Meanwhile, the simultaneous zero density and infinite bulk modulus induce a finite acoustic impedance, which can be designed to match with the background medium and enhance the transmission through the boundaries between the metamaterial and the surroundings.

On the other hand, metamaterials with complex-valued material parameters are related to the attenuation and amplification of acoustic waves. When the loss and gain inside the metamaterial are exactly balanced, the medium is parity-time (PT) symmetric so that the wave propagation is invariant under PT operator. Such PT symmetric systems contain two phases: “exact” and “broken” phases, with exceptional points where the system exhibits unidirectional transparency marking the transition between these two phases. Even though the real parts of the material parameters are usually non-dispersive, the imaginary parts can vary significantly with changing frequencies. In this case, the PT symmetric condition is satisfied only within a narrow frequency band, while the exceptional points can appear

at different frequencies. This limitation challenges the observation of the exceptional points and the realization of unidirectional transparency. A systematic method to access these exceptional points can be achieved by tuning the spacing between the loss and gain materials, which modulates the multiple scattering inside the system to realize unidirectional transparency.

In most cases, acoustic metamaterials consists of deep subwavelength resonators operating around their resonance frequencies. When these resonators are arranged in a two-dimensional surface, they form a metasurface which modulates the phase of acoustic wave and reshape the propagating wavefront. This property can be used for the design of an ultrathin acoustic carpet cloak or diffuser, as shown by the metasurface formed by 3D printed Helmholtz resonators in this dissertation. In the case where the target object contains rapidly changing profiles, the cloaking effect of the designed carpet cloak is preserved. However, the design of acoustic diffuser with rapidly changing profiles requires resonators that can independently modulate the amplitude and phase of the reflected wave.

The control of the phase of acoustic waves enables the generation of vortex beams, which carry orbital angular momentum (OAM) of sound. A topological charge is defined to characterize the amount of OAM carried by the wave. Acoustic vortex beams with different topological charges are orthogonal to each other, which form independent channels to convey information when being multiplexed. Such OAM multiplexing technique increases the information capacity and spectral efficiency for acoustic communication, which holds the potential to increase the communication speed significantly. Besides OAM, acoustic spin defined as sound waves with rotating particle velocity field can be generated. Spin dependent propagation can be observed in a metamaterial waveguide formed by periodic grooves. When a probe meta-atom with acoustic dipole resonance is placed in wave with acoustic spin, a torque induced by spin matter interaction can be measured. The difference between the OAM and spin can be observed by the motion of probe particle. A probe particle moves along a circular trajectory centered at the field center when placed in wave with OAM, while rotates about its own axis when placed in wave with spin.

To my parents,

Changxin Shi and Jinyu Dong,
and all of those who support me throughout this effort,
without whom none of my success would be possible.

"Man will fly through the power of his mind, not through the strength of muscles."
–Nikolay Yegorovich Zhukovsky

Contents

Contents **iii**

List of Figures **vi**

1 Introduction **1**
1.1 A Brief Overview of Acoustics 1
1.2 The History of Acoustic Metamaterials 2
1.3 Overview of the Dissertation 4

2 Fundamentals of Acoustic Wave Propagation **5**
2.1 Derivation of Acoustic Wave Equation 5
2.2 Snell's Law 7
2.3 Waveguide 10
2.4 Diffraction Limit 10
2.5 Helmholtz Resonators 11
2.6 Spherical Waves and Huygens Principle 12

3 Acoustic Double Zero Refractive Index **13**
3.1 Introduction 13
3.2 Design of an Acoustic Double Zero Refractive Index Metamaterial 14
3.3 Acoustic Collimation Achieved by the Double Zero Index Metamaterial . . . 15
3.4 Observation of the Dirac-Like Cone at the Brillouin Zone Center 16
3.5 Single Zero Index Metamaterial 20
3.6 Effective Medium Model 20
3.7 The First Order Waveguide Mode and its Sound Speed 20
3.8 Directivity 23
3.9 Discussions 23
3.10 Methods 25

4 Parity-Time Symmetry in Acoustics **26**
4.1 Introduction 26
4.2 Design of PT Symmetry in Acoustics 27

4.3 Scattering from PT Symmetric Structures 27
4.4 Directional Cloaking with PT Symmetry 31
4.5 Discussions 34

5 Exceptional Points of PT-Symmetric Acoustics 36
5.1 Introduction 36
5.2 Tailoring the Exceptional Points of PT Symmetric Structure 37
5.3 Experimental Demonstration of Unidirectional Transparency 38
5.4 Accessing Exceptional Points at Multiple Frequencies 39
5.5 Reversing the Orientation of Unidirectional Transparency 42
5.6 Measured Scattering Matrix at 5.3 kHz 42
5.7 Method of Control the Artificial Gain Material 44
5.8 Calibration of Unidirectional Microphone Pairs 46
5.9 Experimental Result without Spacing Control 47
5.10 Difference between Exceptional Points and Accidental Degenerate Points . . 48
5.11 Response of Broadband Pulse Signal 50
5.12 Exceptional Points of PT Symmetric Periodic Structures 50
5.13 Control of Exceptional Points in Systems Formed by Multiple Non-Hermitian Materials without PT Symmetry 51
5.14 Discussion on Previous Demonstration of PT Symmetric Acoustics 52
5.15 Discussions 53
5.16 Methods 54

6 Acoustic Metasurfaces 55
6.1 Introduction 55
6.2 Design of Acoustic Metasurfaces 56
6.3 Carpet Cloaking 58
6.4 Virtual Diffuser 60
6.5 Influence of Air Viscosity and Thermoviscous Boundary Layer 61
6.6 Experimentally Measured Bandwidth 66
6.7 Influence of Incident Angle 66
6.8 Discussions 67
6.9 Methods 67

7 Orbital Angular Momentum Multiplexing 70
7.1 Introduction 70
7.2 Significance 71
7.3 Acoustic OAM 72
7.4 OAM Multiplexing 72
7.5 Demultiplexing with Inner Product Algorithm 74
7.6 Generation of Acoustic Vortex and Multiplexed Beams 74
7.7 Bit Error Rate 76

7.8 Experimental Measurement of Bit Error Rate and Signal to Noise Ratio . . . 78
7.9 Design of Receiver Array . . . 78
7.10 Time Interval between Two Sequential Letters . . . 79
7.11 Discussions . . . 80
7.12 Methods . . . 82

8 Acoustic Spin **83**
8.1 Introduction . . . 83
8.2 Existence of Acoustic Spin . . . 84
8.3 Derivation of Acoustic Orbital and Spin Angular Momentum . . . 84
8.4 Generation of Acoustic Spin in Interference Pattern . . . 86
8.5 Acoustic Spin Induced Torque . . . 86
8.6 Dipole Resonance of the Cylindrical Coiled Space Meta-Atom . . . 88
8.7 Measurement of the Spin Induced Torque . . . 89
8.8 Response of the High Power Speakers Used for Torque Measurement . . . 90
8.9 Relations between the Torque, Input Amplitude, and Spin Density . . . 90
8.10 Acoustic Spin Dependent Propagation . . . 91
8.11 Wave Supported by the Acoustic Metamaterial Waveguide . . . 93
8.12 Rotating Acoustic Dipole Created by Four Speakers . . . 94
8.13 Discussions . . . 95

9 Conclusions and Future Works **96**
9.1 Summary of Results and Contributions . . . 96
9.2 Recommendations for Future Works . . . 99

Bibliography **101**

List of Figures

2.1 *An acoustic wave p_i incident normally onto an interface between two materials with impedance Z_1 and Z_2, resulting in reflection p_r and transmission p_t at the boundary.* 8
2.2 *An acoustic wave p_i incident with an oblique angle θ_i onto an interface between two materials with impedance Z_1 and Z_2, resulting in reflection p_r with reflected angle θ_r and transmission p_t with refractive angle θ_t at the boundary.* 9
2.3 *A Helmholtz resonator consisting of a cavity of fluid with volume V and a neck with effective cross-section area S and effective length L.* 11

3.1 *Acoustic metamaterial with simultaneous zero effective mass density and infinite effective bulk modulus. (a) Photography of the fabricated sample with square lattice of 10 × 10 symmetric blind holes constituting an array of cylindrical scatterers. A through hole provides access to the centre of zero index metamaterial for a point source to excite the first order waveguide mode. Four spacers located at the corners of the sample ensure the height of the air channel in the waveguide and the alignments of the top and bottom plates. (b), (c) Top and side views of a unit cell of the zero refractive index metamaterial, respectively. Grey areas mark the solid structures of the waveguide. The light grey circle in the top view denotes the blind holes on the top and bottom plates inside the waveguide. The top and bottom plates are symmetric about the central plane. $D = 16$ mm, $h_0 = 10$ mm, $h_1 = 14.5$ mm, and $a = 30$ mm.* 16

3.2 *Dirac-like cone dispersion of designed double zero index metamaterial. (a) Calculated band structure of the zero index metamaterial. A Dirac-like cone is located at Brilliouin zone centre for the first order waveguide mode at 18.7 kHz. It is formed by the three bands highlighted with red curves. These three bands are degenerate at the Dirac point. (b) Zoom in of three-dimensional dispersion surfaces near the Dirac-like cone. The dispersion surfaces below and above the Dirac point (blue) have negative and positive group velocity, respectively. The metamaterial has zero refractive index at the Dirac point. The flat band (cyan) is not excited in our experiment due to symmetry. (c), (d) calculated pressure fields of the first order waveguide mode showing degenerate monopolar and dipolar behaviors at the Dirac point, respectively. The fields are anti-symmetric along the out-of-plane direction, as expected for the first order waveguide mode. Monopolar and dipolar behaviors modulate the bulk modulus and density of the material, respectively. These modulations enable simultaneous zero effective density and infinite effective bulk modulus at the Dirac point. (e) Full-wave simulation of a plane wave propagating through eight unit cells at 18.7 kHz. The solid side walls are equivalent to periodic boundary conditions forming a two dimensional square lattice. (f) Corresponding simulated (red) and measured (black) normalized transmissions between 18 kHz and 19.4 kHz. The simulated transmission including standard viscous loss over this frequency band is* 91%*, and the measured transmission is* 86%*. The absence of a bandgap and near total transmission demonstrates impedance matching between the double zero index metamaterial and surrounding waveguide.* 17

3.3 *Acoustic plane wave generation from a point source in the zero refractive index metamaterial. (a) Measured pressure field radiated by acoustic point source embedded in zero refractive index metamaterial. The zero refractive index metamaterial collimates the emission from a point source to a plane wave. (b) Measured pressure field radiated by an acoustic point source in the empty waveguide. Without zero refractive index material, a cylindrical wave pattern is obtained in the waveguide. (c) Directivity of a collimated plane wave. The blue circles and red curve are directivities corresponding to the pressure field radiations shown in (a) and (b), respectively. The black curve is the calculated directivity of an ideal line source with the same size (10 unit cells, i.e. 6.5 wavelengths). The zero index metamaterial collimates the acoustic pressure field within* 11 ± 1 *degrees, close to 10.6 degrees given by the theoretical limit of the line source. The noise observed on both experimental results is due to the spurious reflection from the waveguide edges.* 18

3.4 *Measurement of the Dirac-like cone and the associated interface acoustic refraction. (a) Experimentally resolved reciprocal space of the zero index metamaterial near the Brillouin zone centre at different frequencies. A ring is observed at low frequencies and shrinks to a point at 18.7 kHz. The ring opens again as frequency increases. The black dashed circles represent the calculated equifrequency contours of the Dirac-like cone shown in Figure 3.2 and agree well with the measurement. (b), (c), (d) Measured pressure fields outside the metamaterial at 19.1 kHz, 18.7 kHz, and 17.9 kHz, respectively. The black dashed lines and white arrows indicate the acoustic beam profiles and propagation directions. A focusing pattern is observed at 17.9 kHz due to the double negative index property. An acoustic plane wave is obtained at 18.7 kHz as a result of the double zero index metamaterial. The acoustic beam expands when propagating at 19.1 kHz because the material parameters are both positive.* 19

3.5 *Comparison of single and double zero index metamaterials. (a), (b) Dispersion relations of one-dimensional arrays of cylindrical scatterers with lattice constant 2.7 cm and 3 cm, respectively. The frequencies are normalized with the zero index frequency f_0 of the associated structure. For lattice constant 3 cm, the same as the structure in the main text, a Dirac cone is observed, giving double zero index properties. The three bands forming this Dirac cone are highlighted with red curves. Once the lattice constant is detuned to 2.7 cm, the Dirac cone opens up to a bandgap, resulting in single zero index properties. (c), (d) Full wave simulation of transmissions of one-dimensional double and single zero index metamaterials with eight unit cells for normal incidence, respectively. High transmission can be observe for double zero index metamaterial. A large portion of acoustic energy is reflected by the single zero index metamaterial, resulting in a low transmission through the medium. (e) Simulated (red) and measured (black) transmission through the double zero index metamaterial and simulated transmission through the single zero index metamaterial (blue) between 0.97 f_0 and 1.03 f_0 for normal incidence. The simulated and measured transmissions of the double zero index metamaterial are* 91% *and* 86%*, respectively. This high transmission is a result of impedance matching between our designed double zero index metamaterial and the surrounding waveguide. Due to impedance mismatch, only* 30% *transmission can be observed for the single zero index metamaterial.* 21

3.6 *Effective medium model of the double zero index metamaterial for the first order waveguide mode. (a) Normalized effective density and inverse bulk modulus. At 18.7 kHz, the effective density and inverse bulk modulus are simultaneously zero. (b) Normalized refractive index and impedance. The imaginary part of the refractive index is about 2.5×10^{-3} represented by the blue dashed line. At 18.7 kHz, the refractive index is zero and the impedance matches the background waveguide. Both (a) and (b) are sufficient to demonstrate double zero index properties.* . . . 22

3.7 *Dispersion relation of the first order waveguide mode. The red and blue curves correspond to the thinner and thicker waveguides with air channel thickness* $h_0 = 10$ *mm and* $h_1 = 14.5$ *mm, respectively. At 18.7 kHz, the thinner waveguide has smaller wave vector, resulting in larger phase velocity. The ratio between the refractive indices, inversely proportional to the associated phase velocities, is* $n_1/n_0 = 1.94$. 23

3.8 *Theoretical limits of directivity. (a), (b) Normalized fields of plane waves generated by the zero index metamaterial in our experiment and a line source with the same size in simulation, respectively. The directivity of our experimental result shown in (a) is* 11 ± 1 *degrees, close to the simulation of the line source shown in (b). (c) Theoretical limits of directivity with varying line source dimension. Line source with larger dimension generates plane waves with better directivity. The line source with length 6.5 wavelengths shown as the star in (c) corresponding to (b) has a limit 10.6 degrees.* 24

4.1 *Schematic of the acoustic PT symmetric medium. The scattering domain composed of eleven sections, three gain regions (red), three loss regions (green) and five passive regions in between. The length of the active parts is 0.148 m while the length of the passive sections is 0.015 m. The transmission and reflection of acoustic waves incident from left (blue) and right (red) are shown. This PT symmetric medium is designed to be reflectionless for acoustic waves incident from the left.* 28

4.2 *Phases and intensities of left reflected, right reflected, and transmitted waves of the PT acoustic symmetric medium are shown in (a) and (b), respectively. The absolute value of the eigenvalues and the second component of the eigenvectors of the corresponding scattering matrix of this PT acoustic symmetric medium are shown in (c) and (d). We normalized the eigenvectors such that the first component is always unitary.* 30

4.3 *The normalized amplitude of pressure field for the left and right incidences at the exceptional point, respectively.* 31

4.4 *The pressure field maps in the virtual space (a), (b) and the physical space (c), (d) one-way invisible PT symmetric cloak. In (a) and (c) where the plane wave is incoming from left, strong backscattered reflection can be observed due to the satisfied phase matching and therefore the observers on the left can sense the existence of the cloak. However in (b) and (d) where the plane wave is incident from right, the waves propagate without any scattering due to phase mismatching and thus an arbitrary object is perfectly concealed in the white region.* 33

4.5 *(a) Scattering cross section versus frequency, where the blue (upper) and red (lower) curves describe the scattering cross section of the PT-symmetric cloak when the light is incoming from the left and right, respectively. (b) Scattering cross section versus the incident angle at the frequency 6 kHz, where* $\theta = 0$ *corresponds to the parallel propagation along the* z *direction from left to right.* . . . 34

4.6 *The pressure field maps in the virtual space (a), (b) and the physical space (c), (d) for one-way invisible PT symmetric acoustic ground cloak. In (a) and (c) where the plane wave is incoming from left, strong back reflection can be observed due to the satisfied phase matching and therefore the observers on the left can sense the existence of the ground cloak. However in (b) and (d) where the plane wave is incident from right, the waves propagate without any scattering due to phase mismatching and thus an arbitrary object can be concealed in the bump region.* . 34

5.1 *Accessing the exceptional point of acoustic PT system by tuning the spacing between loss and gain materials. (a) Imaginary parts of the refractive indices of loss and gain materials are typically dispersive, so the PT symmetric condition could only be satisfied at single frequency f_b where the loss and gain materials are exactly balanced. (b) Loss and gain materials assembled with spacing. (c) Amplitude of the reflection from the loss side as a function of frequency and the spacing between the loss and gain materials. Exceptional point (EP) occurs at frequency f_b and a specific spacing L_0 when the reflection vanishes. (d) The normalized transmissions (blue, i), reflections from the loss (green, ii) and from the gain (red, iii) in logarithmic scale without spacing, no exceptional point observed. (e) Similar representation to (d) with spacing L_0, an exceptional point observed at f_b.* 38

5.2 *Experiment demonstration of unidirectional transparency of the PT symmetric system at 5.3 kHz. (a) The photo of an experimental sample including loss and gain units. (b), (c) The calculated (solid curves) and measured (marked dots) transmissions and reflections when the incident wave is coming from the loss side. (d), (e) Similar representation to (b), (c) when the incident wave is from the gain side. Black, green, red, blue, and gray colors denote the incidence, reflection from the loss side, the reflection from the gain side, the transmission, and the reflection from the end of the waveguide, respectively. All results have been normalized with the amplitude of incidence. The two calibrated unidirectional microphones are mounted at $l_1 = 15.5$ cm and $l_2 = 13$ cm away from the boundaries of our PT symmetric materials. The spacing between the loss and gain materials is $L = 1.24$ cm. No reflection is observed from the loss side (green curve and dots in (b)), about 330% reflection is observed from the gain side (red curve and dots in (d)), and total transmissions ($|t| = 1$) have been observed on both sides, resulting in unidirectional transparency from the loss side.* 40

5.3 *Taming exceptional points at different frequencies. (a) The measured complex-valued refractive indices of the loss material formed by the leaky waveguide at 5 kHz, 5.3 kHz, 5.7 kHz, and 6 kHz (open marks). The active gain material is tuned to have the refractive indices that are complex conjugate of those of the loss material at the corresponding frequencies (filled marks). (b) The measured amplitudes of the scattering matrices for the controlled exceptional points at these four frequencies with the appropriately tuned spacing between the loss and gain materials. The reflections from the loss side almost vanish and total transmissions are observed for all of the frequencies. The reflections from the gain side are nonzero.* 41

5.4 *Reversing the unidirectional transparency at 5.3 kHz. (a) Calculated transmission (blue) and reflections from the gain side (orange) and the loss side (red) with varying spacing between the loss and gain materials from zero to half wavelength. Two exceptional points are observed when the spacing is 1.24 cm and 1.71 cm, respectively. (b), (c) Transmission and reflections from the gain and loss sides associated with 1.24 cm spacing. Black, blue, red and green colors denote the incidence, transmission, reflection from the gain side, and reflection from the loss side, respectively. Solid curves are calculated values and marked dots are from measurements. The same as Figure 5.2, unidirectional transparency is observed from the loss side. (d), (e) Similar representation to (b), (c), but with 1.71 cm spacing. The direction of unidirectional transparency is reversed. Nearly zero reflection from gain side and* 70% *reflection from the loss side are observed.* . . . 43

5.5 *Seven experimental steps of realizing unidirectional transparency and observing exceptional points in PT symmetric systems. (1) Measuring the scattering matrix of the loss material. (2) Retrieving the effective parameters of the loss material. (3) Calculating the effective parameters of the gain material. (4) Deriving the scattering matrix of the gain material using the calculated effective parameters. (5) Tuning the active gain unit to mimic the actual gain material needed in the system when the entire structure is assembled. (6) Satisfying the PT symmetric condition where the loss and gain materials are precisely balanced. (7) Tuning the spacing between the loss and gain materials by apply opposite electrical phase shifts to the two active emitters to control the exceptional point and realize unidirectional transparency.* 45

5.6 *Calibration of unidirectional microphone pair. (a) Microphone pair mounted in a waveguide with reflectionless ends to measure the back-front-ratio of each microphone. (b) Microphone pair assembled in a waveguide where the structures cause reflection of the incident wave, and hence left and right propagating waves exist in the waveguide.* 47

5.7 *Transmission and reflections from the loss and gain sides of a PT symmetric system consisting of loss and gain units without gap in between. The calculated values are represented by curves and the measured values are represented by marked dots, respectively. Black color shows the incidence, green color shows the reflection from the loss side, red color shows the reflection from the gain side, blue color shows the transmission, and grey color shows the wave reflected from the end of the waveguide, respectively. All waves are normalized by their inputs. The system has small transmission. Reflections can be observed on both sides.* 48

5.8 *Equivalence of two definitions of PT phases. (a) The norm of the eigenvalues of the system scattering matrix varying with spacing between the loss and gain materials. (b) The transmission (blue) and reflections from the gain side (orange) and the loss side (red) varying with spacing between the loss and gain materials from zero to half wavelength at 5.3 kHz. Two exceptional points are observed when the spacing is 1.24 cm and 1.71 cm.* 49

5.9 *Difference between exceptional points and accidental degenerate points. Transmissions (blue curves) and reflections from the gain side (red curves) and from the loss side (green circles) of systems where (a) two exceptional points are observed and (b) one accidental degenerate point is observed. All amplitudes are normalized by their inputs.* 50

5.10 *Transmission and reflections from the gain and loss sides of a pulse incidence with central frequency at 5.5 kHz and bandwidth 2 kHz. The pulse incidence, transmission, and reflections from the gain and loss sides are shown by blue, green, black, and red curves, respectively. The reflection from the loss side vanishes while the reflection from the gain side is obtained. Because the transmission phases at different frequencies are different, the transmitted pulse is slightly distorted, but the transmitted energy remains* 100%. 51

5.11 *Transmissions (blue) and reflections from loss side (green) and gain side (red) of systems with one and a thousand PT symmetric units. Effective loss and gain materials with mass density 1.4 kg/m^3 and refractive indices* $1.4 \pm 0.1j$ *are used. In both cases, two exceptional points are observed. The exceptional points of these two systems appear at the same frequencies.* 52

5.12 *Contrast between the two reflections as a function of frequency and spacing in a system with two loss materials. Each of the loss materials is 10 cm with mass densities 1.4 kg/m^3 and 1 kg/m^3 and refractive indices* $1.4 - 0.1j$ *and* $1.2 - 0.05j$*, respectively. High contrast can be observed along several curves.* 53

6.1 *Acoustic surface engineering for reflected waves. (a) The actual reflected field of a simple bump. The scattering pattern allows acoustic wave to detect the existence of the bump. (b) Acoustic cloaking of a bump with metasurface. The metasurface modulates the phase to flatten the reflected wavefront. Thus, the bump is invisible through acoustic wave. (c) Acoustic diffuser formed by metasurface on a flat surface. With the inverse phase mask of the cloak in (b), the scattering pattern in (a) is created. Therefore, the flat surface with decorated metasurface mimics the bump structure, resulting in a virtual acoustic diffuser. (d), (e) Sketch of structure inducing, respectively, small and large in plane phase gradient. (f) Detailed view of the well structure formed in (e) because of the height variation. (g) Calculated additional phase and amplitude in the reflection R from the well structure for a ratio $m = S_1/S_2 = 3$ as a function of the well depth L normalized by the incident wavelength.* 57

6.2 *Unit cells of metasurface used for acoustic surface engineering. (a) A unit cell formed by a Helmholtz resonator. The unit cell has dimensions 16 mm × 16 mm × 10 mm with a 10 mm × 10 mm × 5 mm cavity and a cylindrical neck, whose diameter is D and height is 2 mm. (b) Numerically calculated relation between reflection phase and neck diameter at 2.9 kHz with COMSOL. By varying the neck diameter, the resonance of the Helmholtz resonator is shifted. For the same working frequency, this shift of resonance results in a different reflection phase. Six different neck diameters are chosen to realize 60, 120, 180, 240, 300, and 360 degrees reflection phase shifts as marked by the dotted lines. (c) Measured (dotted lines) and numerically calculated (dashed lines) resonances of the six selected Helmholtz resonators. Viscosity loss and thermoviscous boundary layers are considered in the COMSOL simulations (see Section 6.5). The resonances are characterized by the dips of the transmission in an acoustic tube waveguide with a corresponding Helmholtz resonator assembled on the side wall of the waveguide. The resonant frequencies of the six resonators shift from the designed values as a result of fabrication errors. The resulted reflection phase modulations are* 4% *within the desired values.* 59

6.3 *Acoustic cloaking with metasurface. (a) Actual structure used in experiments. The complex random structure is constructed from LEGO bricks. This complex random structure is decorated by 3D printed Helmholtz resonators forming an ultrathin metasurface for acoustic surface engineering. (b) Measured reflection field of normal incidence from a flat reflection surface at 2.9 kHz. A flat wavefront is observed. This scan serves as the control experiment for the comparison with cloaking experiment. (c) Measured reflection field of normal incidence from a complex random structure at 2.9 kHz. The reflection field presents multi-scattering pattern as a result of the height variation of the reflection surface and impedance mismatch due to the variation of cross-section area. (d) Measured reflection field of normal incidence from the complex random structure decorated with cloaking metasurface at 2.9 kHz. The cloaking metasurface modulates the reflective surface by manipulating the reflection phase such that the height of each column is reduced virtually to the based surface (flat surface in (a)). Thus, the acoustic wave detects a flat surface and reflected with flat wavefront. Consequently, the complex random structure is cloaked by the metasurface.* 60

6.4 *Acoustic diffuser created by metasurface. (a) Measured reflection field of normal incidence from a circular bump at 2.9 kHz. The circular bump results in wave scattering that diffuses the incident acoustic wave in all directions. (b) Measured reflection field of normal incidence from a flat reflection surface decorated with diffusive metasurface. The metasurface modulate the reflection phase such that the local reflection surface presents a virtual height variation identical to the circular bump in (a). This virtual height variation results in the same scattering pattern that diffuses the acoustic wave in all directions. Thus, the metasurface creates an acoustic diffuser from a flat reflection surface. (c) Measured reflection field of normal incidence from a complex random structure as shown in Figure 6.3b. The multi-scattering pattern is a result of the combination of the reflections due to the rough surface and impedance mismatch. (d) Measured reflection field of normal incidence from a flat reflective surface decorated with the inverse phase mask used for cloaking in Figure 6.3c. The scattering pattern is different from the complex random structure. Thus, the inverse phase mask cannot recreate the scattering of the complex random structure.* 62

6.5 *Inverse phase mask for large in plane phase gradient. (a) Sketch of the well like structure emerging from the large in plane phase gradient objects. (b) Sketch of the virtual diffuser configuration. The amplitude and phase of the purple element are chosen such that the new structure presents the same reflection R as in (a). (c) Analytically calculated amplitude A and phase ϕ obtained from (Eq.* (6.3)*) with $m = 3$ as a function of the well depth L normalized by the incident wavelength. (d) Numerical simulation of the field reflected by a triple well structure at 2.9 kHz with the experimental dimensions (width of 7.5λ). (e) Reproduction of the reflected field with three active elements highlighted in green. Amplitude and phase are taken from (c) respectively to the well depth.* 63

6.6 *Amplitude (a) and phase (b) of the reflected field from Helmholtz resonator with varying radius excited at 2.9 kHz. Blue solid line shows results from simulations without viscous loss. Red open circle shows corresponding simulations while taking loss into account.* 64
6.7 *Reflected field with (bottom line) and without (top line) viscous loss. Plane wave excitation at 2.9 kHz and colorbars are identical for each reflected field represented. The dashed rectangle depicts the field of view used in the experimental results presented in the manuscript.* 64
6.8 *Simulated resonant frequency of each resonator with thermoviscous model (dash) and bulk loss model (solid).* 65
6.9 *Reflected phase in function of the neck diameter when excited at 2900 Hz with thermoviscous model (dash) and lossless model (solid).* 65
6.10 *Reflected field from the decorated profile at 2900 Hz with lossless (left) and thermoviscous (right).* 66
6.11 *Measured reflected field from the rapidly changing profile for different frequencies. The white arrows indicate the upward propagation direction of the reflected field.* 67
6.12 *Reflected field from the rapidly changing profile at 2.9 kHz with varying angle of incidence. Structures and colorbars are identical in every set of simulations.* . . 68
6.13 *Reflected field from the slowly changing profile at 2.9 kHz with varying angle of incidence. Structures and colorbars are identical in every set of simulations.* . . 68

7.1 *Acoustic communication using vortex beams with OAM charges -4 to +4. (a) Experimental setup of acoustic communication with vortex beams. A computer controlled digital to analog circuit generates signal to control four rings of transducers (with sixteen transducers equally spaced on each ring) and emit information encoded into multiplexed acoustic vortex beams into free space at 16 kHz. The radii of these four rings are 3, 6, 9, and 12 wavelengths. (b) Measured orthogonality relations between the bases formed by acoustic vortex beams with OAM charges -4 to +4. Each of the bars is calculated by forming the inner products between the measured pressure fields of the two corresponding bases. The norm of each basis is normalized to unity. The crosstalk between the bases is less than -8.54 dB. (c) Measured pressure field amplitudes and phases of acoustic vortex beam bases with OAM charges -4 to +4 at 100 wavelengths (2.14 m) away from the emitting plane in air. The scanning area covers 22.4 wavelengths by 22.4 wavelengths (48 cm by 48 cm) with 26 by 26 resolutions. Thermal and rainbow scale colorbars are used for the measured amplitude and phase fields, respectively.* 73

7.2 *Experimental demonstration of acoustic communication using multiplexed acoustic vortex beams. (a) Binary (ASCII) representations of the letters in the word "Berkly". Each letter contains eight bits (one byte) of information. Each byte contains the same amount of total amplitude, i.e. the signal bars in each letter sum up to unity. This amplitude amount is equally distributed into the vortex beams forming the multiplexed signal. A multiplexed beam formed by the eight orthogonal vortex beams with OAM charges -4 to +4 is capable to convey the information of each letter. (b) Measured signals of the letters in the word "Berkly". The bars are calculated by forming the inner product between the measured pressure fields of the multiplexed signal and the bases. The norms of the bases are normalized to unity. Like (a), each letter contains the same amount of total amplitude, which is equally distributed in the on-channels when sending. (c) Calculated pressure field amplitudes and phases of the multiplexed signal of the letters in the word "Berkly". The field patterns of the letters are superimposed that one cannot judge the information without demultiplexing through inner product. (d) Measured pressure field amplitudes and phases of the multiplexed signal of the letters in the word "Berkly". The experimental results match with the calculated fields in (c). Colored scale bars are used for the amplitude and phase fields, respectively.* 75

7.3 *Active phase array used in our experiment. (a) Experimental setup. The digital processor on the left drives the speakers mounted on the plastic frame. (b) Pattern of the emitting array containing 64 speakers. Each circle represents a speaker. These speakers form four rings with radii 3, 6, 9, and 12 wavelengths. Each ring contains 16 equally spaced speakers.* 76

7.4 *Measured bit error rate (BER) versus signal to noise ratio (SNR) of acoustic OAM communication with 26 × 26 sensor array used in the receiver. The squares are measured data with all bytes have the same total amplitude, which is equally distributed in the on-channels of the byte. The BER decreases with increasing SNR. At 20 dB SNR level, the BER is* $10^{-6.5}$*, which is smaller than the forward error correction (FEC) limit and can still be corrected by standard FEC approaches [152], confirming that our communication system with acoustic OAM is reliable. The blue curve is a regression curve of the experimental data. The measured results fit with this regression curve* $BER = 1/2erfc(\sqrt{SNR/(8.0 \pm 0.4)})$*, indicating the spectral efficiency to be* 8.0 ± 0.4 *(bit/s)/Hz. The theoretical limit of the spectral efficiency is given by the number of orthogonal channels used for data transmission, in this case is 8 bit/s/Hz. Therefore, our acoustic communication device with eight OAM charges employed for information encoding is already working at the theoretical limit.* 77

7.5 *Method used for BER calculation. The two curves are Gaussian with average μ_1 and μ_0 and standard deviation σ_1 and σ_0 for on (blue) and off (red) channels, respectively. C is the crossing of the two curves and is set as the criterion to judge if the signal is on or off. The error bits are on channels below C and off channels above C. The BER is given by the ratio of the green area and the area below the two curves.* 78

7.6 *Examples of receiver arrays used to measure the BER versus SNR response. Each circle represents a microphone. The array contains (a) 61, (b) 62, (c) 63, and (d) 64 microphones. These microphones form four rings with radii 5.4, 6.7, 8, and 9.3 wavelengths. For array with $N = 4n+r$ (n and r are integers and $r < 4$) sensors, the inner r rings have $n + 1$ equally spaced sensors and the outer $4 - r$ rings have n equally spaced sensors.* 79

7.7 *Measured BER dependence of number of sensors. The circles are measured data with all bytes have the same total amplitude, which is equally distributed in the on-channels of the byte. The BER decreases with increasing number of sensors in the receiver array from 8 to 68 microphones with the pattern of the array shown in the Section 7.8. The dashed line marks the FEC limit which determines the maximum error rate that can still be corrected by standard FEC approaches, which is BER = $2\times10^{-}3$ [152]. This BER limit corresponds to a minimal required receiver array with 34 sensors in our experiment. Further increasing the number of receivers will not improve the BER significantly.* 80

7.8 *Full wave simulation of acoustic communication with orbital angular momentum multiplexing with three-cycle pulse. (a) The pulse profile of the three-cycle pulse used for simulation. (b) Obtained amplitude and phase patterns for the word "Berkly" using the two-cycle pulse for communication.* 81

7.9 *Bit error rate (BER), which characterize the communication performance of the system, with varying number of receivers for the two integration time intervals. It can be seen that the BER performances for these two cases are the same.* . . . 82

8.1 *Acoustic spin as a rotating particle velocity field. (a) A rotating particle velocity (black arrow) can be decomposed into two components v_x (blue arrow) and v_y (red arrow) along x and y directions. The two components shown as the blue and red lines are 90 degrees out-of-phase. (b) Acoustic spin in the interference of two acoustic beams. Two beams with equal amplitudes propagating along x and y directions contribute v_x and v_y components of the particle velocity field, respectively. The phase difference between v_x and v_y is the function of the position. The zoomed-in region shows an area where the phase difference between v_x and v_y changes from 0^o to 360^o. When the phase difference is 90 or 270 (equivalent to -90) degrees, the local particle velocity field is rotating circularly, resulting in spin up (blue) or spin down (red) acoustic field; When the phase difference is 0, 180, or 360 degrees, the particle velocity field is oscillating along a line. In other cases, the local particle velocity rotates elliptically.* 85

8.2 *Experimental observation of acoustic spin. (a) Experimental setup for the measurement of acoustic spin resulted from the interference of two perpendicular beams and the spin induced torque acting on a coiled space acoustic meta-atom. Two pairs of high power speakers at two neighboring edges emit at 870 Hz with a 90-degree phase difference. The transparent glass walls at the top and the bottom confine acoustic waves propagating at the fundamental mode, mimicking an ideal two-dimensional scenario extended infinitely in the perpendicular direction. The coiled space meta-atom is hanged at the center using a thin copper wire. (b) Simulated and (d) measured pressure fields show a 90-degree phase difference at the center of the interference pattern where the local particle velocity rotates clockwise, resulting in a spin up field. (c) Simulated and (e) measured spin density distributions show that the spin density reaches its local maximum at the center where the meta-atom is located. (f) Measured pressure field when only one speaker is on. (g) Measured spin density when only one speaker is on. No spin exists in this case. The measured area for (d), (e), (f), (g) is 40 cm × 40 cm. (h) Measured torques acting on the coiled space meta-atom (inset) versus input voltage amplitude loaded on the speakers. The spin up or spin down acoustic wave applies a negative or positive torque (with respect to z axis in Figure 8.1b) on the particle. The torques induced by the spin up and spin down waves are equal in amplitude and follow a quadratic relation with the input amplitude, in agreement with our theoretical prediction that the torque is proportional to the spin density.* 87

8.3 *Symmetric coiled space meta-atom. (a) The meta-atom fabricated by 3D printer with ABS plastic. (b) The pressure field of the dipole mode shape of the meta-atom. (c) Calculated with thermo-viscous effect (blue curve) [47] and measured (black circles) of the normalized transmission through the meta-atom. From the calculation, the dipole resonance occurs at 890 Hz. The experimental result shows that this dipole resonance occurs at 870 Hz, which is chose for the measurement of the spin induced torque.* 89

8.4 *Speaker response with varying input voltage amplitude of the high power speakers used for spin induced torque measurement. A microphone is fixed at a location far away from the speakers to avoid the saturation of the microphone response. The speakers behave linearly before the saturation occurs at 250 mV input voltage.* 90

8.5 *Spin dependent propagation in acoustics. (a) Schematic of local particle velocity field of an evanescent acoustic wave supported by a metamaterial waveguide composed of periodic grooves. The acoustic field outside the waveguide decays exponentially along y axis and propagates along x axis.* $\mathbf{v}(t_1)$ *(red),* $\mathbf{v}(t_2)$ *(green), and* $\mathbf{v}(t_3)$ *(blue) represent the particle velocities at time* t_1*,* t_2*, and* t_3 *with* $0 < t_1 < t_2 < t_3$*, respectively. The local particle velocity rotates clockwise in time. The propagation direction is solely determined by the spin direction, resulting in spin dependent propagation. (b) Experimental setup for demonstrating the spin dependent propagation. Four mini-speakers (inset) are mounted near the acoustic waveguide. A rigid wall on each side confines the acoustic wave propagating in-plane. The four speakers emit at 2 kHz with a 90-degree phase difference between the neighboring speakers, mimicking a rotating acoustic dipole, which excites spin up or spin down acoustic wave determined by the relative phase difference among four speakers. (c), (e), (g) Normalized amplitudes of simulated and measured pressure fields. The acoustic metamaterial waveguide is at the bottom of each figure (not shown). The spin down and spin up acoustic waves are excited in (c), (e) and (g), respectively. The measured area of (e) and (g) is 60 cm* $\times$ *40 cm. The spin down acoustic wave propagates only towards left, while the spin up wave propagates towards right, demonstrating the phenomenon of spin dependent propagation. The thermal color scale is used for the pressure amplitude. (d), (f), (h) Normalized spin density for spin down and spin up acoustic waves in (c), (e) and (g), respectively, confirming the acoustic spin dependent propagation. The jet color scale is used for the spin density.* 92

8.6 *Acoustic wave propagating along the metamaterial waveguide. (a) The pressure field (jet color scale) and particle velocity field (red arrows) of the acoustic wave propagating along the metamaterial waveguide. The wave is propagating along x-direction, while evanescently decaying along y-direction. (b) Geometry of the grooves. The period is* $p = 6.35$ *mm, width* $w = 4.76$ *mm, and depth* $T = 15.9$ *mm. (c) The dispersion relations of the metamaterial waveguide (red) and sound cone (blue).* 93

8.7 *Acoustic rotating dipole mimicked by four speakers. (a), (b) the pressure field (jet color scale) and particle velocity field (red arrows) of the four speakers emitting at 2 kHz with phase increasing by 90 degrees between the neighboring speakers in the clockwise direction at time 0 in (a) and a quarter period in (b), respectively. The acoustic dipole represented by the particle velocity direction is rotating in the clockwise direction.* 94

Acknowledgments

It is my pleasure to acknowledge the roles of several individuals who were critical for the completion of my PhD research. First of all, I would like to thank my PhD advisor, Professor Xiang Zhang, for his patience, immense knowledge, and his great support on my research. His kind and helpful support and encouragement are key factors for my success on finishing my PhD studies. I could not have imagined having a better advisor and mentor for my Ph.D study.

Second, I would like to thank my PhD dissertation committee members, Professors Oliver M. O'Reilly, Chris Dames, and James Analytis, and Professor George C. Johnson for their insightful help throughout this effort.

My sincere thank also goes to Dr. Marc Dubois for his generous help on the study of this research. It was a wonderful experience to work with him as a collaborator and learn a lot of experimental skills from him. Meanwhile, I am grateful to Professors Xuefeng Zhu, Jie Zhu, and Dr. Rongkuo Zhao for fruitful and stimulating discussions on the theoretical analysis, experimental techniques, and fundamental physics of acoustics. My thank also goes to Mr Lei Cheng and Professor Yun Chen, who helped design the digital control circuits which are crucial components of my experimental setup. I would like to thank all of them for co-authoring the papers I published during my PhD study.

I would also like to express my gratitude to the Berkeley Fellowship for Graduate Study, the Chin Leung Shui Chun Fellowship, the Graduate Division Block Grant Award, and the Office of Naval Research (ONR) MURI program under grant number N00014-13-1-0631 for the support of my PhD study and research.

I thank my fellow labmates and friends from Duke University, Rutgers University, University of Texas at Austin, and Massachusetts Institute of Technology for the helpful comments in the reviews within the group and the MURI program, which widen my research from various perspectives, especially Dr. Yuan Wang, who helps a lot on both scientific research and communications. I also thank the Lawrence Berkeley National Laboratory for giving me access to the outstanding research facility.

Last but not the least, I would like to thank my parents, Changxin Shi and Jinyu Dong, and my family for their endless support on both my life and study.

Chapter 1

Introduction

1.1 A Brief Overview of Acoustics

Acoustics is a multidisciplinary science studying the propagation of mechanical vibrations. As a branch of physics and mechanical engineering, acoustics has attracted the interest of researchers for centuries because of its broad impact on almost all aspects of human society from our daily communication to biomedical treatments. According to the different applications, the study of acoustics has been divided into multiple subbranches like physical acoustics, structural acoustics, architectural acoustics, speech acoustics, musical acoustics, psychological acoustics, biomedical acoustics, etc. For all of these subbranches, the acoustic sources, the propagating media, and the acoustic sensors are the three key components in the study. Based on the materials where the wave propagates in, the acoustic waves can be categorized as sound waves propagating in fluids and elastic waves propagating in solids. The physics of elastic waves is described by the displacements of the solid particles in three-dimensional space characterizing the three polarizations categorized into longitudinal, shear vertical, and shear horizontal waves. Compared with the complicated polarizations of elastic waves, most of the physics of sound waves can be described by scalar pressure fields, whose polarization is mostly longitudinal. This dissertation focuses on the control of sound wave propagation in fluids like air and water.

The propagation of sound waves is controlled by the material parameters of the fluids including the refractive index and acoustic impedance. These two material parameters are determined by the density and bulk modulus of the media. When a sound wave hits the boundary between two fluids whose refractive index and acoustic impedance are different, reflection and refraction occur where a portion of the acoustic energy transmits through the boundary and the rest of the acoustic energy reflects backward obeying Snell's law. The reflective index also determines the speed of sound propagating inside the fluid. In most cases where the acoustic attenuation is considered, the refractive index becomes complex-valued whose imaginary part characterize the loss of sound wave propagating through the medium. Besides the material parameters, the geometry of structures also affects acoustic

wave propagation especially for waves propagating in waveguides such as pipes, ducts, and air slabs confined within two solid plates. The wave propagation inside these structures as well as the effective material parameters of the geometries can be derived by applying the continuity boundary conditions between different structures. The analogy between different structural geometries and electrical components like inductance and capacitance is developed, which results in acoustic transmission line method to model the wave propagation in the structures. With these modelling methods, different structures are designed to control the sound wave propagation.

Besides the medium where sound waves propagate through, the acoustic sources and sensors are critical components in wave generation and measurements. In practical applications like communication and detection, acoustic beam forming achieved by controlling the amplitude and phase of each element in the source array is required, where the propagation direction and wave pattern of the generated acoustic beam is controlled by the programmable active source array. The design of both the source and sensor arrays is also critical for applications like imaging and communication where time reversal technique is crucial. The arrangement of the sensor array can also affect the accuracy of the measured acoustic signal. Therefore, the study of acoustic sources and sensors is an important branch of acoustics.

In this dissertation, I focus on realizing different material parameters through various designs of acoustic structures for the control of sound wave propagations. The design of acoustic source and sensor arrays for wave control in the realization of high-speed acoustic communication is also discussed. Such designs provide important guidelines for the control of sound propagations which is critical for practical applications including communication, detection, and imaging.

1.2 The History of Acoustic Metamaterials

The control of sound propagation on demand has been desired for centuries. Many ancient architectures are designed to enhance the sound intensity in the auditoriums. However, many other critical controls like nonreciprocal wave propagation are still difficult to be realized using the properties of nature materials. The study of metamaterials started from the discussion of the properties of negative material parameters for electromagnetic waves [1]. In 2000, Pendry discovered that such negative parameters can be used for the realization of optical imaging beyond diffraction limit [2], where diffraction limit refers to the limitation of the size of focal point which cannot be smaller than half of wavelength. In the same year, Sheng's group from Hong Kong realized the first sonic crystal with negative effective mass density using the dipolar resonance of unit cells formed by iron balls coated with rubber in some frequency bands [3]. Negative effective bulk modulus was realized by Fang and colleagues utilizing the monopolar resonance of Helmholtz resonators at some other frequencies [4]. For both cases, the single negative material parameter (effective mass density or bulk modulus) results in a purely imaginary sound speed at the corresponding frequencies, forming frequency bandgaps where the sound wave cannot propagate through the medium.

The realization of imaging beyond the diffraction limit requires the existence of metamaterials with simultaneous negative mass density and bulk modulus in some frequency bands where the sound speed and refractive index become negative. Such metamaterial was first realized in a one-dimensional waveguide with membranes and side holes forming the unit cells of the metamaterial [5]. A three-dimensional negative refractive index metamaterial was realized using soft materials where the monopolar and dipolar resonances co-exist in the unit cells [6].

Besides applying a slab of metamaterial with negative refractive index to realize acoustic imaging beyond diffraction limit, devices including hyperlens [7] and superlens [8, 9] were designed to achieve deep-subwavelength resolution. Diffraction limit is a result of the lost information of non-propagating evanescent waves with large transverse wave vector. The designed hyperlens and superlens used metal structures to realize anisotropic media in which the evanescent waves in free space with large transverse wave vector become propagating wave, and the information conveyed by these waves can be transmitted through the space [7, 8]. Time reversal technique applied on an array of acoustic resonators is another approach to realize wave control at subwavelength scale [9].

Metamaterials with zero-valued parameters can be realized at frequencies in between the bands where the refractive index transients from negative value to positive value because the material parameters are continuous functions of frequency. At the frequencies where the material parameters of a metamaterial become zero, intriguing phenomena like infinite phase velocity, cloaking, and wave tunneling can be observed for electromagnetic waves [10]. In acoustics, density near zero metamaterials were realized with iron block array and membrane structure [11, 12]. These density near zero metamaterials, however, possess zero acoustic impedance which can never match with the surrounding media. Such strong impedance mismatch results in a strong reflection at the boundary between the metamaterial and background medium. In practical applications where high transmission through material boundaries is desired, zero refractive index metamaterials with simultaneous zero mass density and infinite bulk modulus whose impedance can be designed to match with the background medium are required. These double zero refractive index metamaterials can be realized by designing unit cells with both monopolar and dipolar resonances forming a Dirac-like cone at Brillouin zone center [13, 14].

With the ability to realize material parameters ranging from negative to zero to positive and anisotropic properties using different structural materials, the propagation trajectory of acoustic wave can be manipulated by media designed based on transformation acoustics and achieve acoustic cloaking [15]. The transformation acoustics algorithm maps the coordinates and material parameters of a virtual uniform space onto the physical cloaking region, such that the distribution of refractive index over the cloaking region bends the acoustic rays so the wave propagates without reaching the cloaked object and is never scattered [16–18].

For sound waves whose wavelength is usually large, ultrathin materials are desired to be used for the control of sound propagation. In this case, acoustic metasurfaces with subwavelength thickness were developed. Most of the existing metasurfaces can be categorized into two major types based on their working principles: coiled spaced structures and resonating

elements. The coiled spaced structures modulate the effective phase velocity by coiling up the propagation path such that the actual propagation distance can be controlled by the space coiling without changing the thickness of the structures [19, 20]. Metasurfaces formed by resonating elements including decorated membranes and Helmholtz resonators modulate the wave propagation through the resonances of the unit cells which are used to realize near perfect absorbers [21] and ultrathin carpet cloak [22, 23].

In addition to passive structures, active elements like piezoelectric components are also used in the design of acoustic metamaterials. Applying these active elements, non-reciprocal sound propagation where the wave transmissions from different sides are different can be realized [24, 25]. Such active elements can also be used as acoustic gain material which is a crucial component in acoustic parity-time symmetric (PT) systems where the sound attenuation and amplification balance with each other [26]. Under certain conditions, the PT symmetric system reaches exceptional point where the metamaterial exhibits unidirectional reflection properties [27, 28]. Meanwhile, these active elements are used to form an acoustic phase array for the generation of different acoustic beams for the realization of high-speed acoustic communication [29].

1.3 Overview of the Dissertation

This dissertation is organized in the following structure. Chapter 2 discusses some fundamentals of acoustic wave propagation including the derivation of acoustic wave equation, waveguides, Snell's law, diffraction limit, and resonators. Chapter 3 explores the realization of double zero refractive index acoustic metamaterials induced by Dirac-like cone at Brillouin zone center and the properties of these metamaterials. Chapter 4 introduces acoustic metamaterials with PT symmetry where the loss and gain media inside the system balance each other. Chapter 5 studies the properties of exceptional points in PT symmetric acoustics and the method to control these exceptional points. Chapter 6 discusses the realization of an ultrathin acoustic metasurface using resonators for acoustic illusion with rapidly changing profiles. Chapter 7 investigates the properties of acoustic orbital angular momentum (OAM) generated by an active phase array and its application in high-speed acoustic communication. Chapter 8 explores the existence of acoustic spin and its properties. Chapter 9 summarizes the dissertation and lists potential future directions for further studies of acoustic metamaterials and angular momentum.

Chapter 3 of this dissertation is based on [14]. Chapter 4 is based on [26]. Chapter 5 is based on [28]. Chapter 6 is based on [23]. Chapter 7 is based on [29].

Chapter 2

Fundamentals of Acoustic Wave Propagation

2.1 Derivation of Acoustic Wave Equation

The acoustic waves discussed in this dissertation refers to sound waves propagating in fluids like air and water. The fluids are assumed to be isotropic and compressible. According to the balance of mass of the fluid, when we take a finite volume of fluid, the continuity equation can be derived as

$$\frac{\partial \rho_f}{\partial t} + \nabla \cdot (\rho_f \mathbf{u}) = 0, \tag{2.1}$$

where $\rho_f = \rho_0 + \rho$ is the density of the fluid, ρ_0 is the constant density of the fluid when no acoustic wave propagates inside the medium, ρ is the oscillation of the fluid density as a result of propagating wave, and $\mathbf{u}$ characterize the particle velocity field of the acoustic wave. Linearization of the continuity equation yields

$$\frac{\partial \rho}{\partial t} + \rho_0 \nabla \cdot \mathbf{u} = 0. \tag{2.2}$$

The finite volume of fluid also satisfies the balance of linear momentum, which yields

$$\rho_f \frac{\partial \mathbf{u}}{\partial t} = -\nabla P, \tag{2.3}$$

where $P = p + P_0$ is the pressure applied on the finite volume of fluid, p is the oscillating pressure field as a result of the acoustic wave, and P_0 is the hydrostatic pressure. Linearization of the balance of linear momentum yields

$$\rho_0 \frac{\partial \mathbf{u}}{\partial t} = -\nabla p. \tag{2.4}$$

The oscillating density ρ, pressure field p, and particle velocity field $\mathbf{u}$ are three unknown variables, indicating that an additional equation is required to solve for acoustic wave

equation. This additional equation comes from the definition of bulk modulus as another material parameter of the finite volume of fluid. When being compressed, both the volume and density of the finite volume of fluid change, but the product of these two quantities remains constant as a result of the balance of mass, which yields

$$\delta(\rho_f V) = \rho V + \rho_0 \delta V = 0. \tag{2.5}$$

This equation renders the relation between the variation of density and volume as

$$\frac{\delta V}{V} = -\frac{\rho}{\rho_0}. \tag{2.6}$$

According to the definition of bulk modulus κ_0, which characterize the change of volume of fluid under pressure

$$p = -\kappa_0 \frac{\delta V}{V} = \frac{\kappa_0}{\rho_0}\rho. \tag{2.7}$$

This is the phase equation of the finite volume of fluid. Substitution of the phase equation into the continuity equation yields

$$\frac{\partial p}{\partial t} + \kappa_0 \nabla \cdot \mathbf{u} = 0. \tag{2.8}$$

Without loss of generality, ρ and κ are used to replace ρ_0 and κ_0, representing the constant fluid density and bulk modulus when no wave is propagating inside the medium for this dissertation.

The acoustic wave equation of motion is derived by taking the divergence of the balance of linear momentum equation in Eq. (2.4) and substituting into Eq. (2.8), which yields

$$\frac{\partial^2 p}{\partial t^2} - c^2 \nabla^2 p = 0, \tag{2.9}$$

where $c = \kappa/\rho$ is the sound speed in the fluid.

Without loss of generality, we first consider an acoustic plane propagating along x axis. The wave solution of the acoustic wave equation in Eq. (2.9) satisfies

$$p = p_+(x - ct) + p_-(x + ct), \tag{2.10}$$

where $p_+(x - ct)$ and $p_-(x + ct)$ characterize the wave propagating towards $+x$ and $-x$ directions, respectively. It should be noticed that $p_+(x - ct)$ and $p_-(x + ct)$ are independent from each other. Substitution of the solution of the wave propagating towards $+x$ direction into the balance of linear momentum equation in Eq. (2.4) yields

$$\rho \frac{\partial u_x}{\partial t} = p'_+(x - ct), \tag{2.11}$$

where p'_+ represents the derivative of p_+ and u_x is the x component of $\mathbf{u}$. Integrating Eq. (2.11) yields

$$u_x = \frac{p_+}{Z}, \tag{2.12}$$

where $Z = \rho c$ is the acoustic impedance of the fluid, which is an intrinsic property of the material. The acoustic intensity which quantifies the energy is given by the product of pressure and particle velocity.

For a harmonic acoustic wave, the solution of the wave equation becomes

$$p = p_0 \cos(\omega t - kx + \phi), \tag{2.13}$$

where p_0 is the amplitude, ω is the angular frequency, $k = \omega/c$ is the wave number, and ϕ is the phase of the wave. One should also notice that the sign of k determines the propagation direction of the wave. The wavelength of the acoustic wave is $\lambda = c/f$, where $f = \omega/(2\pi)$ is the frequency of the wave. Therefore, the relation between the wave number and wavelength is given by $k = 2\pi/\lambda$. In the literature, the complex-valued form is also used to describe the acoustic wave as

$$p = p_0 e^{j(\omega t - kx + \phi)}, \tag{2.14}$$

where $j = \sqrt{-1}$ is the imaginary unit. The real-time pressure field of the acoustic wave is given by the real part of Eq. (2.14). For convenience, the complex-valued form is used in this dissertation.

In three dimensional space, the wave solution becomes

$$p = p_0 e^{j(\omega t - \mathbf{k}\cdot\mathbf{r} + \phi)}, \tag{2.15}$$

where $\mathbf{k}$ is the wave vector that defines the propagation direction of the wave and $\mathbf{r}$ defines the location in the space.

2.2 Snell's Law

When an acoustic wave propagates normally onto the boundary of two materials whose impedance are Z_1 and Z_2 as shown in Figure 2.1, the wave frequency remains constant and the continuities of pressure and particle velocity are satisfied at the interface. For pressure field, we have

$$p_i + p_r = p_t, \tag{2.16}$$

where p_i, p_r, and p_t are the pressure field of the incident, reflected, and transmitted waves, respectively. Applying the continuity of particle velocity field and Eq. (2.12) yields

$$\frac{p_i - p_r}{Z_1} = \frac{p_t}{Z_2}. \tag{2.17}$$

The solutions of Eqs. (2.16) and (2.17) are given by

$$R = \frac{Z_2 - Z_1}{Z_2 + Z_1}, \tag{2.18a}$$

$$T = \frac{2Z_2}{Z_2 + Z_1}, \tag{2.18b}$$

where $R = p_r/p_i$ and $T = p_t/p_i$ are the reflection and transmission coefficients, respectively. When the impedances $Z_1 = Z_2$, indicating the media on the two side of the boundary are the same, Eq. (2.18) yields $R = 0$ and $T = 1$. Thus, the acoustic wave has total transmission and no reflection in this case. If the ratio between Z_1 and Z_2 approaches zero, the acoustic wave hits a hard wall. In this case, $R = 1$ and $T = 2$, while the particle velocity field of the transmitted wave is zero, indicating that no acoustic energy transmits through the hard wall and the acoustic wave has total reflection. For the case when the ratio between Z_1 and Z_2 approaches infinity, the acoustic wave hits a soft wall. In this case, $R = -1$ and $T = 0$. Thus, no acoustic energy can transmit through soft wall, and the acoustic wave has total reflection.

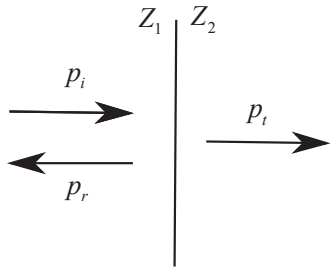


Figure 2.1: *An acoustic wave p_i incident normally onto an interface between two materials with impedance Z_1 and Z_2, resulting in reflection p_r and transmission p_t at the boundary.*

For oblique incident acoustic waves propagating onto the boundary between two materials with impedance Z_1 and Z_2 as shown in Figure 2.2, continuities of pressure and particle velocity fields along the direction perpendicular to the boundary still hold. For convenience, only harmonic waves are considered and the boundary is set as $x = 0$. It should be noticed that the acoustic frequency remains constant when propagates across the boundary. In this case, applying the continuity of pressure at $x = 0$ yields

$$P_i e^{j(\omega t - k_1 \sin\theta_i y)} + P_r e^{j(\omega t - k_1 \sin\theta_r y)} = P_t e^{j(\omega t - k_2 \sin\theta_t y)}, \tag{2.19}$$

where P_i, P_r, and P_t are the amplitudes of the pressure fields of incident, reflected, and transmitted waves, respectively. θ_i, θ_r, and θ_t mark the incident, reflected, and transmitted angles. $k_1 = \omega/c_1$ and $k_2 = \omega/c_2$ are the wave numbers of acoustic waves propagating in Z_1 and Z_2 media. Simplification of Eq. (2.19) yields

$$k_1 \sin\theta_i = k_1 \sin\theta_r = k_2 \sin\theta_t. \tag{2.20}$$

Equation (2.20) indicates that the reflected angle θ_r and the incident angle θ_i are equal. The transmitted angle (also called refractive angle) and the incident angle satisfy the refractive

relation governed by Snell's Law

$$\sin\theta_t = \frac{c_2}{c_1}\sin\theta_i = \frac{n_1}{n_2}\sin\theta_i, \tag{2.21}$$

where $n_1 = c_0/c_1$ and $n_2 = c_0/c_2$ are the refractive index of the media, and c_0 is the sound speed of the background medium which can be air ($c_0 = 343$ m/s) or water ($c_0 = 1500$ m/s) for most cases. When $n_1 > n_2$ ($c_1 < c_2$), the quantity on the right hand side of Eq. (2.21) can be larger than one. In this case, the refractive angle does not exist, indicating that the acoustic wave has zero transmission and total reflection. For a special case where the incident angle satisfies

$$\theta_i = \arcsin\frac{n_2}{n_1}, \qquad n_1 > n_2, \tag{2.22}$$

the refractive angle θ_t is 90 degrees. Thus, the incident acoustic wave excites a surface acoustic wave traveling along the interface between the two media. This incident angle is defined as the critical angle of the interface between the two materials.

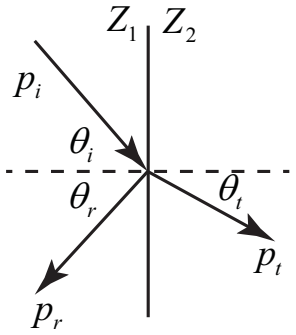


Figure 2.2: *An acoustic wave p_i incident with an oblique angle θ_i onto an interface between two materials with impedance Z_1 and Z_2, resulting in reflection p_r with reflected angle θ_r and transmission p_t with refractive angle θ_t at the boundary.*

For the case when $n_1 < n_2$ or when the incident angle is smaller than the critical angle for $n_1 > n_2$, the pressure fields of the reflected and transmitted waves are determined by the continuity of pressure given by Eq. (2.16) and the continuity of particle velocity field along x axis given by

$$\frac{\cos\theta_i}{Z_1}(1-R) = \frac{\cos\theta_t}{Z_2}T. \tag{2.23}$$

Therefore, the reflection and transmission coefficients of this obliquely incident wave are

$$R = \frac{Z_2\cos\theta_i - Z_1\cos\theta_t}{Z_2\cos\theta_i + Z_1\cos\theta_t}, \tag{2.24a}$$

$$T = \frac{2Z_2\cos\theta_i}{Z_2\cos\theta_i + Z_1\cos\theta_t}. \tag{2.24b}$$

One can observe that the effective impedance for the obliquely traveling waves are $Z_1^{\text{eff}} = Z_1/\cos\theta_i$ and $Z_2^{\text{eff}} = Z_2/\cos\theta_t$.

2.3 Waveguide

Acoustic waveguides are fluids like air or water where sound waves propagate inside which are enclosed by solid boundaries whose cross-section can be rectangular, circular, and any other shapes. For convenience, we focus on the discussion of waveguides with rectangular cross-section and solid boundaries which can be treated as hard wall boundaries at $y = 0$ and $y = h$, where h is the height of the waveguide, and the boundary condition can be expressed as

$$\frac{\partial p}{\partial y} = 0, \qquad y = 0 \text{ or } h. \tag{2.25}$$

Without loss of generality, we also assume the waveguide is infinitely long along z axis, and the sound waves propagate along x direction. Substitution of Eq. (2.25) into the acoustic wave solution in Eq. (2.15) yields

$$k_y = \frac{m\pi}{h}, \tag{2.26a}$$

$$k_x = \sqrt{(\frac{\omega}{c})^2 - k_y^2}, \tag{2.26b}$$

where m is an integer, which defines the order of the waveguide mode. For example, if $m = 0$ the pressure field in a waveguide cross-section of a propagating sound wave is uniform, which is defined as acoustic plane wave (also called the fundamental waveguide mode). If $m = 1$, the pressure field of the sound wave in the cross-section is anti-symmetric, which is named odd mode or the first order waveguide mode. Equation (2.26b) indicates that the acoustic frequency ω must be larger than $m\pi c/h$ such that the propagation wave number k_x becomes real and the sound wave can propagate inside the waveguide. This frequency defines the cut-off frequency of the corresponding waveguide mode below which the sound wave cannot propagate.

2.4 Diffraction Limit

Diffraction limit characterizes the type of information carried by acoustic waves that can propagate through space and be received in the far-field. The information carried by the acoustic waves are determined by the wave vector in the plane perpendicular to the propagation direction. Without loss of generality, let us assume the wave propagates along x direction. Thus, we have the propagation wave number

$$k_x = \sqrt{(\frac{\omega}{c})^2 - k_{yz}^2}, \tag{2.27}$$

where k_{yz} is the in-plane wave vector that carries the information. Because the propagating acoustic wave in free-space has a constant frequency ω, the in-plane wave vector k_{yz} must be smaller than $\omega/c = 2\pi/\lambda$. Information carried by higher wave vectors becomes evanescent that cannot be transmitted. Because the acoustic wave propagation is reciprocal, one can also use the same argument to derive that the acoustic wave cannot be focused to a spot smaller half-wavelength $\lambda/2$.

2.5 Helmholtz Resonators

Helmholtz resonator is a type of acoustic resonator that is commonly used for acoustic wave manipulations which consists of a cavity of fluid enclosed by hard wall boundaries with a small hole named as neck to connect with the ambient as shown in Figure 2.3. The fluid trapped in the neck has a small volume which is assumed to be incompressible and behaves like a solid mass particle with its mass given by

$$m = \rho SL, \tag{2.28}$$

where S is the effective cross-section area of the neck and L is the effective length of the neck. The volume of the fluid in the cavity is compressible and behaves like a spring. When the mass in the neck moves by a small displacement ξ under pressure p, the change of volume in the cavity is given by

$$\Delta V = \xi S. \tag{2.29}$$

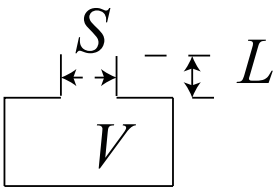


Figure 2.3: *A Helmholtz resonator consisting of a cavity of fluid with volume V and a neck with effective cross-section area S and effective length L.*

Substitution of Eq. (2.29) into the definition of bulk modulus yields

$$p = -\kappa \frac{\Delta V}{V} = -\rho c^2 \frac{\xi S}{V}, \tag{2.30}$$

where V is the hydrostatic volume of the fluid in the cavity. Therefore, the effective spring constant of the cavity is

$$K = \frac{\rho c^2 S^2}{V}. \tag{2.31}$$

Substitution of Eqs. (2.28) and (2.31) into the resonant frequency equation of mass-spring harmonic oscillators yields the resonant frequency of Helmholtz resonator as

$$\omega_0 = \sqrt{\frac{K}{m}} = \sqrt{\frac{Sc^2}{VL}}. \tag{2.32}$$

2.6 Spherical Waves and Huygens Principle

When written in spherical coordinates, the acoustic wave equation in Eq. (2.9) becomes

$$\frac{\partial^2 p}{\partial r^2} + \frac{2}{r}\frac{\partial p}{\partial r} = \frac{1}{c^2}\frac{\partial^2 p}{\partial t^2}, \tag{2.33}$$

where r is the radial coordinate in the spherical coordinates. Multiplication of Eq. (2.33) by r yields

$$\frac{\partial}{\partial r}(\frac{\partial}{\partial r}(rp)) = \frac{1}{c^2}\frac{\partial^2 (rp)}{\partial t^2}. \tag{2.34}$$

The solution of Eq. (2.34) is given by

$$p(r,t) = \frac{A}{r}e^{j(\omega t - kr + \phi)}, \tag{2.35}$$

characterizing the spherical waves emitted by a point source located at the origin of the spherical coordinates. In more general cases, the acoustic wave solution emitted by a point source is given by

$$p(\mathbf{r},t) = \frac{A}{|\mathbf{r}|}e^{j(\omega t - \mathbf{k}\cdot\mathbf{r} + \phi)}, \tag{2.36}$$

where $\mathbf{r}$ is the position vector pointing towards the sensing point from the point source and $|\cdot|$ is the norm of the vector.

When considering acoustic waves generated by an array of point sources, line sources, or plane sources, one can discretize the continuous sources into finite elements that can be considered as point sources and applying Huygens principle to calculate the generated acoustic field at the sensing point as

$$p = \sum_i \frac{A_i}{|\mathbf{r_i}|}e^{j(\omega t - \mathbf{k}\cdot\mathbf{r_i} + \phi_i)}, \tag{2.37}$$

where the integration covers all point sources in the array or discretized point sources of the continuous sources.

Chapter 3

Acoustic Double Zero Refractive Index

3.1 Introduction

Acoustic wave behavior is affected by material parameters such as mass density and bulk modulus of the media where the wave propagates. Metamaterials provide a new strategy to design unprecedented material properties that do not exist in nature [3–8, 16–18, 21, 30–35]. Metamaterials with negative effective mass density and bulk modulus were experimentally developed using locally resonant sonic crystal [3] and Helmholtz resonators [4], respectively. These materials are called single negative materials as only one of their parameters is negative. The refractive index of such materials is dominantly imaginary, due to a bandgap. With proper design of the multiple scattering in bi-periodic crystal, single negative materials can be used to realize a superlens that breaks the diffraction limit [30]. Double negative materials with negative refractive index whose mass density and bulk modulus are simultaneously negative were demonstrated using a one-dimensional waveguide with membranes and side holes [5, 36] and coiled space structures [37–39]. Anisotropic materials were realized for the design of an acoustic hyperlens [7], super-resolution imaging [8], and cloaking [17, 18]. While single zero materials have been explored both in electromagnetic (epsilon near-zero) [10, 40, 41] and acoustic metamaterials (density near-zero) [11, 42, 43], these media suffer from low transmission due to an impedance mismatch. In acoustics, the impedance of a material is given by $Z = \sqrt{\rho\kappa}$, where ρ is the mass density and κ is the bulk modulus. An acoustic double zero refractive index metamaterial with simultaneously zero density and infinite bulk modulus achieving finite impedance overcomes such an obstacle (see Sections 3.5 and 3.6). Recently developed electromagnetic metamaterials with Dirac-like cone at the Brillouin zone centre exhibit double zero index properties [13, 44–46]. These electromagnetic metamaterials consist of periodic scatterers with phase velocity lower than the surrounding materials [13, 44]. But this requirement is extremely challenging for airborne sound applications because the sound speed in air is slow compared with other materials.

Zero index materials where sound propagates without phase variation, holds a great potential for wavefront and dispersion engineering. Recently explored electromagnetic double zero index metamaterials consist of periodic scatterers whose refractive index is significantly larger than that of the surrounding medium. This requirement is fundamentally challenging for airborne acoustics because the sound speed (inversely proportional to the refractive index) in air is among the slowest. Here, we report the first experimental realization of an impedance matched acoustic double zero refractive index metamaterial induced by a Dirac-like cone at the Brillouin zone centre. This is achieved in a two-dimensional waveguide with periodically varying air channel that modulates the effective phase velocity of a high-order waveguide mode. Using such a zero index medium, we demonstrated acoustic wave collimation emitted from a point source. For the first time, we experimentally confirm the existence of the Dirac-like cone at the Brillouin zone centre.

Here, we apply cylindrical scatterers with height larger than background air channel in a two-dimensional waveguide where the acoustic phase velocity is smaller than air sound speed for a high-order waveguide mode to realize an acoustic double zero refractive index metamaterial. The acoustic double zero refractive index metamaterial is used to collimate cylindrical waves emitted from a point source at the center of the medium. Our analysis of the collimated acoustic beam exhibits a high directivity performance. The holey structure of the double zero index metamaterial allows us to measure the acoustic field inside the medium and map the reciprocal space to confirm the existence of Dirac-like cone at the Brillouin zone centre experimentally for the first time. Acoustic zero refractive index metamaterials open a new door for effective acoustic wave engineering in applications such as ultrasound medical imaging and underwater communication.

3.2 Design of an Acoustic Double Zero Refractive Index Metamaterial

In this letter, we experimentally realize an acoustic metamaterial with simultaneous zero mass density and infinite bulk modulus induced by a Dirac-like cone at the Brillouin zone centre by periodically varying the thickness of an air channel in a two-dimensional waveguide (Figure 1), resulting in the change of the effective sound speed of the first order waveguide mode (see Section 3.7)

$$c(\omega, h) = (\sqrt{\frac{1}{c_0^2} - \frac{\pi^2}{\omega^2 h^2}})^{-1}, \tag{3.1}$$

where $c_0 = 343$ m/s is the sound speed in air, ω is the angular frequency, and h is the thickness of the air channel. The periodic cylindrical air columns with larger air thickness in Figure 3.1 have slower phase velocity than in the surrounding waveguide. With proper scatterer dimensions and lattice constant, this material exhibits a Dirac-like cone at the Brillouin zone centre for the first order waveguide mode (Figure 3.2). This Dirac-like cone is formed by the degeneracy of a monopolar mode and two dipolar modes (Figure 3.2). The monopolar mode

modulates the effective bulk modulus and the dipolar mode affects the effective mass density [47]. The pressure field of the other dipolar mode is orthogonal to the one shown and is not excited. The lowest band of the Dirac-like cone contains a negative group velocity as the wave vector decreases with increasing frequency (Figure 3.2). Consequently, the material behaves as a double negative medium; similarly for double positive behavior for the upper cone. At the Dirac point where these two bands are degenerate, the effective mass density and inverse of bulk modulus are simultaneously zero. This gapless band structure allows high transmission because acoustic impedance remains finite. A first order waveguide mode plane wave is generated and propagates through a slab of eight unit cells in order to test the transmission at normal incidence (Figure 3.2). The measured transmitted amplitude is nearly constant across the Dirac-like cone (Figure 3.2). This result indicates the absence of bandgap in the fabricated metamaterial. Furthermore, the measured 86% amplitude transmission confirms impedance matching between our designed metamaterial and surrounding medium. One-dimensional conical dispersion was observed in coiled space structures [11, 43]. However, the narrow channels in the complex structure increase the viscosity loss [48]. Thus, it is difficult to achieve double zero index under such a high loss and perfect transmission can hardly be observed.

3.3 Acoustic Collimation Achieved by the Double Zero Index Metamaterial

Acoustic wavefront engineering and plane wave generation is crucial for the applications such as imaging and sensing [49]. Traditional acoustic plane wave generation requires implementation of large arrays of sources together with complex controlling circuits. Indeed, single acoustic sources are small compared with wavelength, emitting cylindrical waves in two dimensional space whose intensity decays along traveling distance. As the phase velocity is infinite in a zero index material, the phase of the acoustic field is uniform throughout the material. Therefore, one can design the wavefront of the outgoing field by shaping the interface between the zero index material and the surrounding medium [50, 51]. In our experiment, an acoustic point source exclusively exciting the first order waveguide mode is placed at the centre of a square metamaterial sample consisting of ten by ten unit cells (Figure 3.1). The pressure field radiated by the point source at the Dirac point frequency (18.7 kHz) is scanned and shown in Figure 3.3 with and without the metamaterial, respectively. We observe that the phase along the edge of the metamaterial is uniform. Therefore, the cylindrical wavefront emitted by the point source is collimated into a plane wave. This experimental result confirms that the metamaterial acts as a double zero index medium at this frequency. The amplitude of the collimated plane wave is confined within 11 ± 1 degrees (Figure 3.3). This directivity performance is near the theoretical limit (10.6 degrees) obtained from a line source with the same dimensions (see Section 3.8). The measured amplitude of the collimated plane wave contains about 30% of the point source emission. The reduced transmission has already

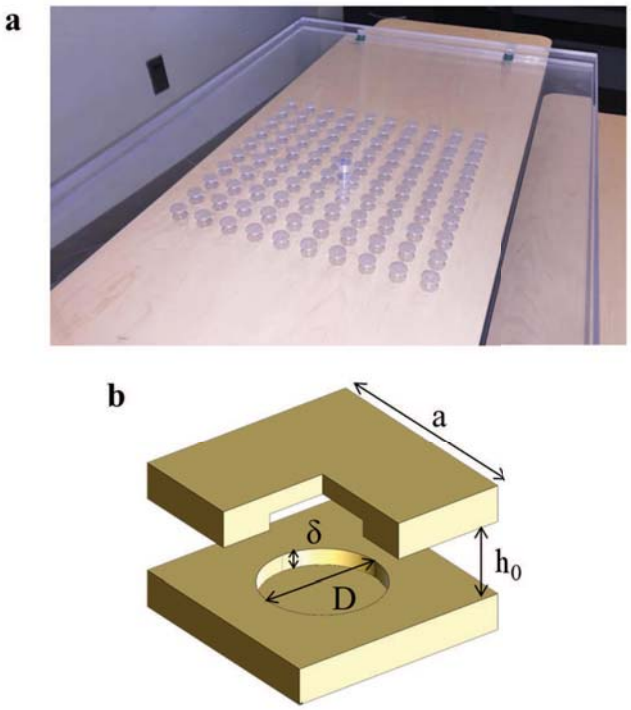


Figure 3.1: *Acoustic metamaterial with simultaneous zero effective mass density and infinite effective bulk modulus. (a) Photography of the fabricated sample with square lattice of 10 × 10 symmetric blind holes constituting an array of cylindrical scatterers. A through hole provides access to the centre of zero index metamaterial for a point source to excite the first order waveguide mode. Four spacers located at the corners of the sample ensure the height of the air channel in the waveguide and the alignments of the top and bottom plates. (b), (c) Top and side views of a unit cell of the zero refractive index metamaterial, respectively. Grey areas mark the solid structures of the waveguide. The light grey circle in the top view denotes the blind holes on the top and bottom plates inside the waveguide. The top and bottom plates are symmetric about the central plane.* $D = 16$ *mm,* $h_0 = 10$ *mm,* $h_1 = 14.5$ *mm, and* $a = 30$ *mm.*

been reported and explained in optics due to the low available density of states [45].

3.4 Observation of the Dirac-Like Cone at the Brillouin Zone Center

The existence of a Dirac-like cone at the Brillouin zone centre provides a key evidence of double zero index property [13, 44–46]. As the metamaterial structure is hollow, one can directly access the field within and characterize the equifrequency contour in the reciprocal

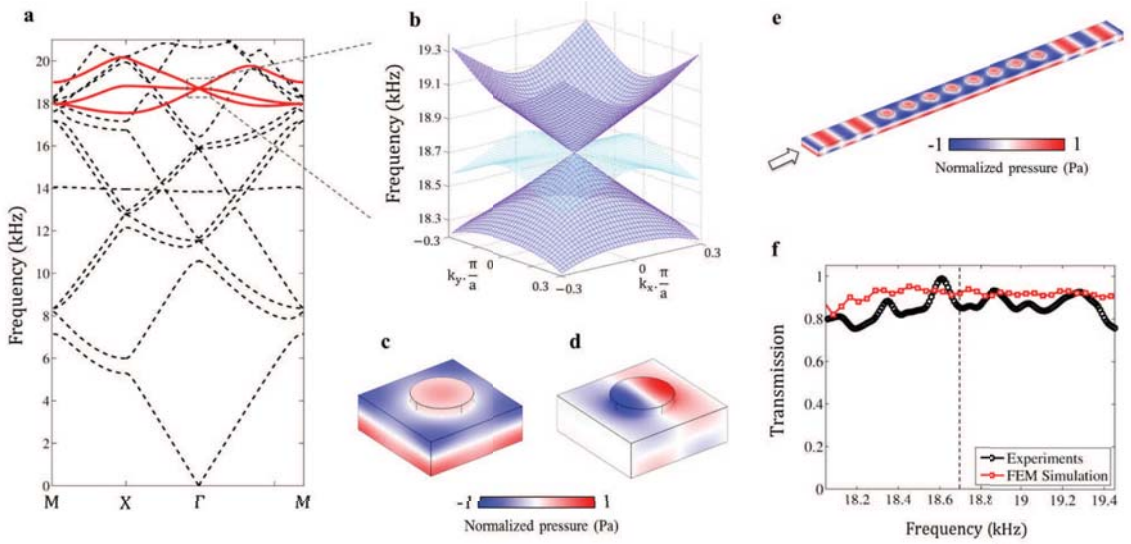


Figure 3.2: *Dirac-like cone dispersion of designed double zero index metamaterial. (a) Calculated band structure of the zero index metamaterial. A Dirac-like cone is located at Brillouin zone centre for the first order waveguide mode at 18.7 kHz. It is formed by the three bands highlighted with red curves. These three bands are degenerate at the Dirac point. (b) Zoom in of three-dimensional dispersion surfaces near the Dirac-like cone. The dispersion surfaces below and above the Dirac point (blue) have negative and positive group velocity, respectively. The metamaterial has zero refractive index at the Dirac point. The flat band (cyan) is not excited in our experiment due to symmetry. (c), (d) calculated pressure fields of the first order waveguide mode showing degenerate monopolar and dipolar behaviors at the Dirac point, respectively. The fields are anti-symmetric along the out-of-plane direction, as expected for the first order waveguide mode. Monopolar and dipolar behaviors modulate the bulk modulus and density of the material, respectively. These modulations enable simultaneous zero effective density and infinite effective bulk modulus at the Dirac point. (e) Full-wave simulation of a plane wave propagating through eight unit cells at 18.7 kHz. The solid side walls are equivalent to periodic boundary conditions forming a two dimensional square lattice. (f) Corresponding simulated (red) and measured (black) normalized transmissions between 18 kHz and 19.4 kHz. The simulated transmission including standard viscous loss over this frequency band is* 91%*, and the measured transmission is* 86%*. The absence of a bandgap and near total transmission demonstrates impedance matching between the double zero index metamaterial and surrounding waveguide.*

space. The pressure field inside the metamaterial is scanned for different frequencies and mapped onto reciprocal space with two-dimensional Fourier transform (Figure 3.4). A Dirac-like cone is observed at the Brillouin zone centre between 18.1 kHz and 19.3 kHz with its Dirac point at 18.7 kHz. This measured Dirac-like cone matches with the theoretical dispersion

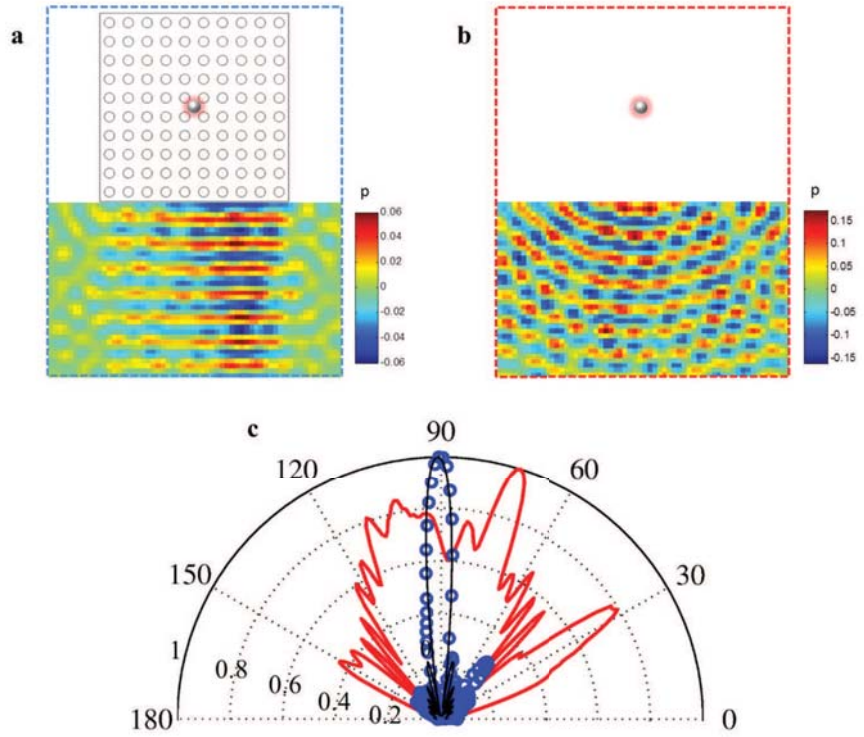


Figure 3.3: *Acoustic plane wave generation from a point source in the zero refractive index metamaterial. (a) Measured pressure field radiated by acoustic point source embedded in zero refractive index metamaterial. The zero refractive index metamaterial collimates the emission from a point source to a plane wave. (b) Measured pressure field radiated by an acoustic point source in the empty waveguide. Without zero refractive index material, a cylindrical wave pattern is obtained in the waveguide. (c) Directivity of a collimated plane wave. The blue circles and red curve are directivities corresponding to the pressure field radiations shown in (a) and (b), respectively. The black curve is the calculated directivity of an ideal line source with the same size (10 unit cells, i.e. 6.5 wavelengths). The zero index metamaterial collimates the acoustic pressure field within* 11 ± 1 *degrees, close to 10.6 degrees given by the theoretical limit of the line source. The noise observed on both experimental results is due to the spurious reflection from the waveguide edges.*

shown in Figure 3.2. At the Dirac point, the medium exhibits double zero index property. Subsequently, we measure a collimated plane wave at 18.7 kHz (Figure 3.4). The upper band of the Dirac-like cone gives a positive group velocity to acoustic wave propagating in the metamaterial. Therefore, a classic refraction effect occurs at the interface resulting in the expansion of the acoustic beam observed at 19.1 kHz (Figure 3.4). For frequencies below the Dirac point, the metamaterial acts as a double negative medium while the outer waveguide is a double positive medium. They form a negative-positive interface and focus

the acoustic beam (Figure 3.4). The measured amplitude of the focusing beam compared with the point source emission at the same frequency is 60%. This continuous evolution of refractive index from double negative to double positive is also confirmed by the measured acoustic field inside the metamaterial. At 18.3 kHz, the acoustic field envelope merges into the point source due to the double negative refractive index. The acoustic field envelope propagates away from the point source at 19.1 kHz where the refractive index is double positive. At 18.7 kHz, the excited acoustic field envelope is breathing with a uniform phase distribution because of the double zero refractive index.

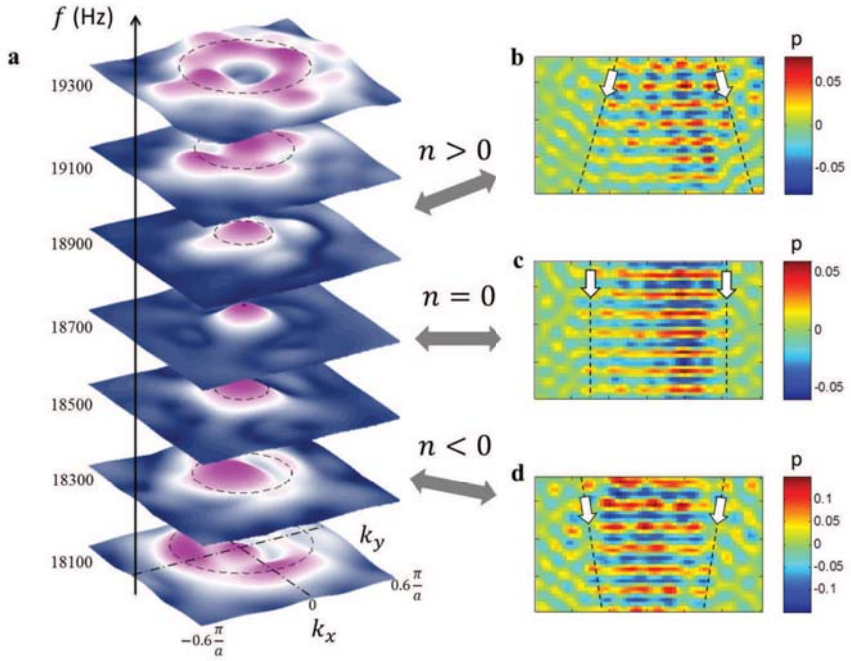


Figure 3.4: *Measurement of the Dirac-like cone and the associated interface acoustic refraction. (a) Experimentally resolved reciprocal space of the zero index metamaterial near the Brillouin zone centre at different frequencies. A ring is observed at low frequencies and shrinks to a point at 18.7 kHz. The ring opens again as frequency increases. The black dashed circles represent the calculated equifrequency contours of the Dirac-like cone shown in Figure 3.2 and agree well with the measurement. (b), (c), (d) Measured pressure fields outside the metamaterial at 19.1 kHz, 18.7 kHz, and 17.9 kHz, respectively. The black dashed lines and white arrows indicate the acoustic beam profiles and propagation directions. A focusing pattern is observed at 17.9 kHz due to the double negative index property. An acoustic plane wave is obtained at 18.7 kHz as a result of the double zero index metamaterial. The acoustic beam expands when propagating at 19.1 kHz because the material parameters are both positive.*

3.5 Single Zero Index Metamaterial

To investigate the difference between double and single zero index metamaterials, we detune the lattice constant of our designed structure to 2.7 cm that opens up the Dirac cone at the Brillouin zone centre (Figure 3.5), resulting in a single zero index metamaterial. The full wave simulations of one-dimensional waveguides with eight unit cells of single and double zero index metamaterials for normal incident first order waveguide mode plane wave at the zero index frequency f_0 are shown in Figure 3.5, respectively. The solid side walls act as periodic boundaries as discussed in the main text. The transmission through the single zero index metamaterial is much lower than the double zero index metamaterial. Figure 3.5 shows the simulated (red) and measured (black) transmission through the double zero index metamaterial and the simulated (blue) transmission through the single zero index metamaterial. The transmission through the double zero index metamaterial has the same value discussed in the main text. At the zero index frequency f_0, a bandgap can be observed due to impedance mismatch, resulting in 30% transmission through the single zero index metamaterial.

3.6 Effective Medium Model

To further confirm that our designed metamaterial is a double zero index metamaterial, we retrieve the effective material parameters of a slab containing five unit cells by measuring the transmission and reflection in our full wave simulation with normal incidence [52]. The normalized effective density and bulk modulus are simultaneously zero at the Dirac point frequency, indicating that the metamaterial presents double zero index properties at this frequency (Figure 3.6). This characterization is equivalent to the model with refractive index and impedance. The normalized index is zero at 18.7 kHz, and the impedance matched with the surrounding waveguide ($Z = 1.1Z_0$ for simulation and $Z = 1.3Z_0$ for experiment shown in the main text, with Z_0 to be the impedance of the plain waveguide). The measured imaginary part of the refractive index is about 2.5×10^{-3} through the measured frequency range (blue dashed line in Figure 3.6), confirming that the metamaterial has zero real and imaginary part of the refractive index at 18.7 kHz.

3.7 The First Order Waveguide Mode and its Sound Speed

The first order waveguide mode is acoustic wave propagating in a waveguide whose maximum pressure amplitudes occur at the two boundaries of the waveguide and are phase opposite. Thus, the pressure distribution along the z-axis is anti-symmetric about the centre line of the waveguide. Such first order waveguide mode is used in all of our experiments because the designed zero refractive index material works for this acoustic propagating mode. The

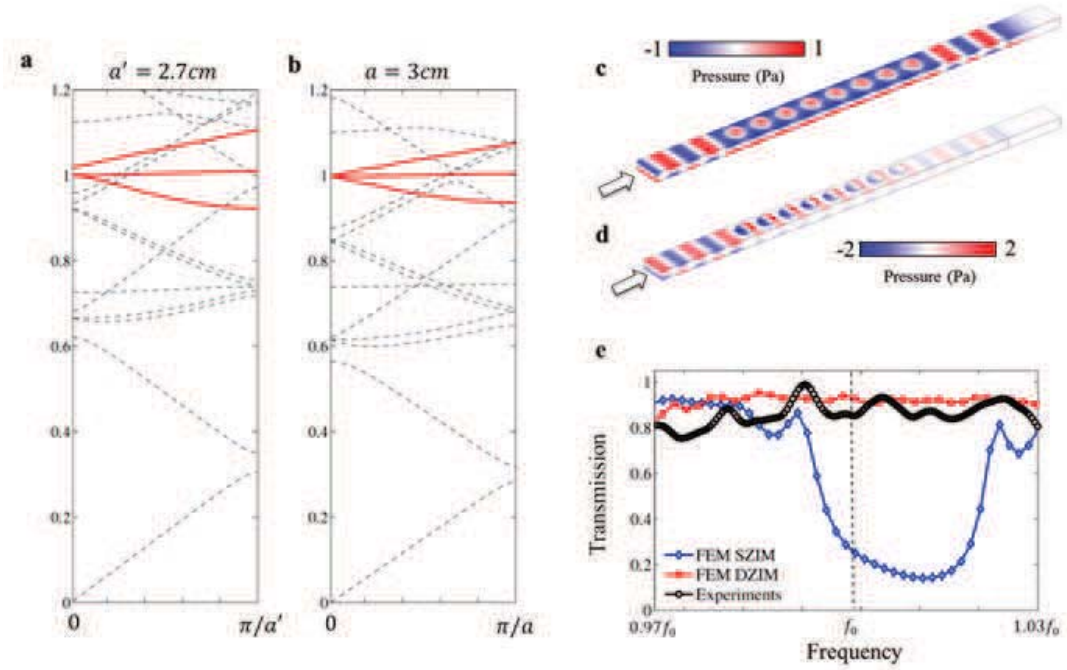


Figure 3.5: *Comparison of single and double zero index metamaterials. (a), (b) Dispersion relations of one-dimensional arrays of cylindrical scatterers with lattice constant 2.7 cm and 3 cm, respectively. The frequencies are normalized with the zero index frequency f_0 of the associated structure. For lattice constant 3 cm, the same as the structure in the main text, a Dirac cone is observed, giving double zero index properties. The three bands forming this Dirac cone are highlighted with red curves. Once the lattice constant is detuned to 2.7 cm, the Dirac cone opens up to a bandgap, resulting in single zero index properties. (c), (d) Full wave simulation of transmissions of one-dimensional double and single zero index metamaterials with eight unit cells for normal incidence, respectively. High transmission can be observe for double zero index metamaterial. A large portion of acoustic energy is reflected by the single zero index metamaterial, resulting in a low transmission through the medium. (e) Simulated (red) and measured (black) transmission through the double zero index metamaterial and simulated transmission through the single zero index metamaterial (blue) between 0.97 f_0 and 1.03 f_0 for normal incidence. The simulated and measured transmissions of the double zero index metamaterial are* 91% *and* 86%*, respectively. This high transmission is a result of impedance matching between our designed double zero index metamaterial and the surrounding waveguide. Due to impedance mismatch, only* 30% *transmission can be observed for the single zero index metamaterial.*

wave number along the z-axis is

$$k_z = \frac{\pi}{h}, \tag{3.2}$$

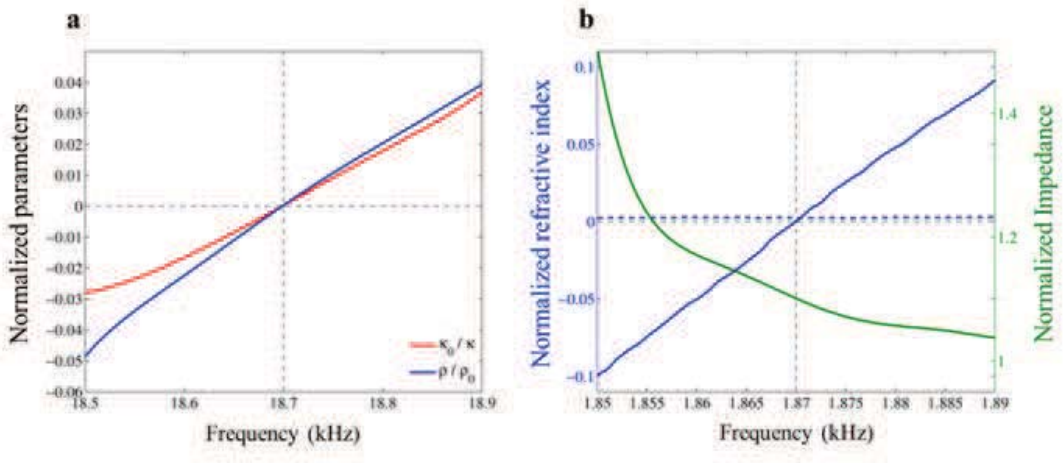


Figure 3.6: *Effective medium model of the double zero index metamaterial for the first order waveguide mode. (a) Normalized effective density and inverse bulk modulus. At 18.7 kHz, the effective density and inverse bulk modulus are simultaneously zero. (b) Normalized refractive index and impedance. The imaginary part of the refractive index is about* 2.5×10^{-3} *represented by the blue dashed line. At 18.7 kHz, the refractive index is zero and the impedance matches the background waveguide. Both (a) and (b) are sufficient to demonstrate double zero index properties.*

where h is the height of the waveguide. Based on the balance of linear momentum, the propagating wave number along x-axis is

$$k_x = \sqrt{k^2 - k_z^2} = \sqrt{\frac{\omega^2}{c_0^2} - \frac{\pi^2}{h^2}}, \tag{3.3}$$

where k is the total wave number, ω the angular frequency, and $c_0 = 343$ m/s) is the sound speed in air. Thus, the sound speed of the first order waveguide mode is

$$c = \frac{\omega}{k_x} = (\sqrt{\frac{1}{c_0^2} - \frac{\pi^2}{\omega^2 h^2}})^{-1}, \tag{3.4}$$

Equation (3.4) indicates that a waveguide with larger air channel thickness exhibits lower phase velocity. This result is confirmed by the dispersions of waveguides with different air channel thickness shown in Figure 3.7. The red (blue) dispersion curve for the first order waveguide mode corresponds to the waveguide with thinner (thicker) air channel. At the same frequency, the red dispersion curve associated with thinner air channel has smaller wave vector, resulting in larger phase velocity. For waveguides with 10 mm and 14.5 mm, the ratio of refractive indices inversely proportional to phase velocity is $n_1/n_0 = 1.94$ at the Dirac point frequency (18.7 kHz).

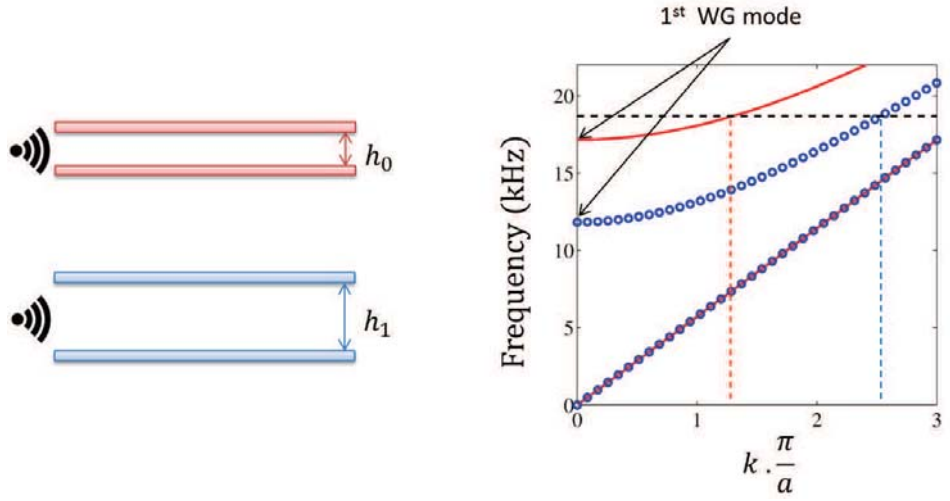


Figure 3.7: *Dispersion relation of the first order waveguide mode. The red and blue curves correspond to the thinner and thicker waveguides with air channel thickness* $h_0 = 10$ *mm and* $h_1 = 14.5$ *mm, respectively. At 18.7 kHz, the thinner waveguide has smaller wave vector, resulting in larger phase velocity. The ratio between the refractive indices, inversely proportional to the associated phase velocities, is* $n_1/n_0 = 1.94$.

3.8 Directivity

The directivity of a plane wave can be expressed as the angle over which the amplitude of the plane wave is confined. As discussed in the main text, the amplitude generated by our zero index metamaterial sample excited by a point source is confined within 11 ± 1 degrees (Figure 3.8). A line source with the same dimension (30 cm, i.e. 6.5 wavelengths) generating a plane wave at 18.7 kHz is simulated by COMSOL 3.5b and shown in Figure 3.8. The comparison between the experimental and simulated fields indicates that the directivity performance of the zero index metamaterial is close to the theoretical limit. The theoretical limits of directivity with different line source dimensions are calculated (Figure 3.8). The directivity performance improves as the length of the line source becomes larger because line source with small dimensions compared with the wavelength behaves like a point source. For a line source with length 30 cm, the theoretical limit of directivity is 10.6 degrees as shown by the star in Figure 3.8. This result confirms that the directivity performance of our sample is neat the theoretical limit.

3.9 Discussions

In conclusion, we have experimentally demonstrated the first acoustic double zero index metamaterial. The measurement of the reciprocal space inside the metamaterial reveals the

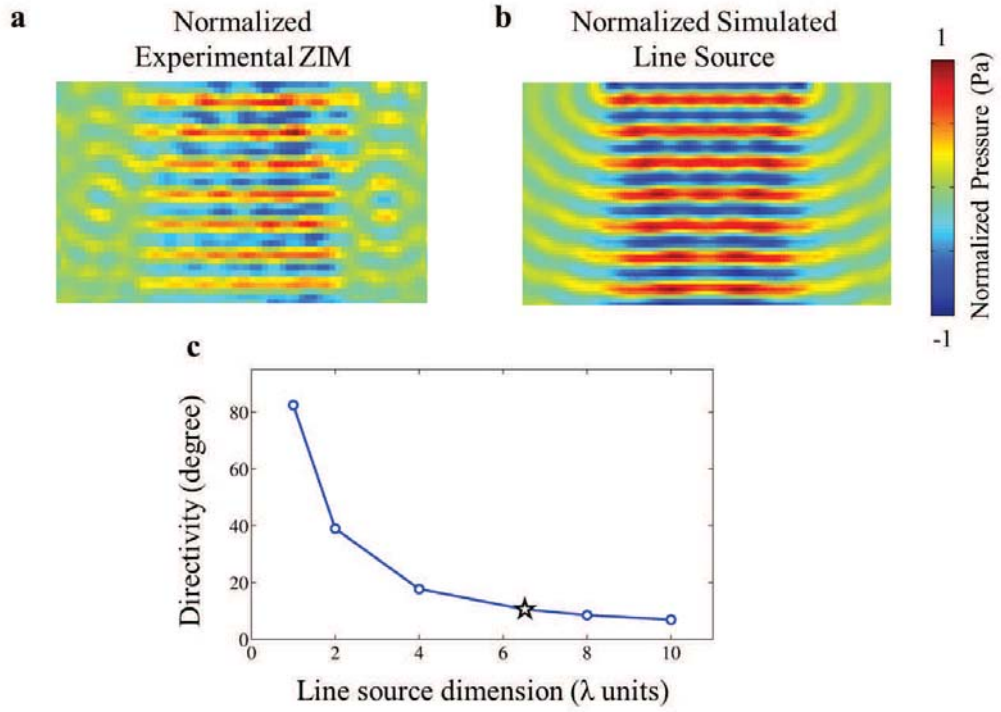


Figure 3.8: *Theoretical limits of directivity. (a), (b) Normalized fields of plane waves generated by the zero index metamaterial in our experiment and a line source with the same size in simulation, respectively. The directivity of our experimental result shown in (a) is* 11 ± 1 *degrees, close to the simulation of the line source shown in (b). (c) Theoretical limits of directivity with varying line source dimension. Line source with larger dimension generates plane waves with better directivity. The line source with length 6.5 wavelengths shown as the star in (c) corresponding to (b) has a limit 10.6 degrees.*

presence of a Dirac-like cone at the Brilloun zone centre. As a consequence, this metamaterial possesses simultaneous zero effective mass density and infinite bulk modulus at the Dirac point. This allows impedance matching with background medium and is confirmed with the transmission measurement. Acoustic beam collimation from a point source is also demonstrated using the zero index property in this passive structure. Acoustic zero index materials offers unique wavefront engineering, providing a novel platform for the exploration of new fundamental physics such as transformation acoustics, sound dispersion, and phase matching.

3.10 Methods

The band structure of our designed material is calculated using a commercial finite element solver (COMSOL). This designed material contains cylindrical air scatterers with radius 8 mm and height 14.5 mm forming a square lattice with lattice constant 30 mm in a two dimensional 10 mm thick air waveguide (Figure 3.1). This waveguide is formed by two acrylic plates over a 930 mm by 540 mm area. The blind holes forming the 10 by 10 cylindrical scatterers are drilled by a CNC machine. Spacers are placed at the four corners of the waveguide to form the 10 mm thick air channel between the two acrylic plates. The waveguide with 8 unit cells used to measure transmission shown in Figure 3.2 is also fabricated by the CNC machine. Two PUI AST-1532MR-R speakers generating airborne sound with opposite phase are assembled face to face at the top and bottom plates. They form an acoustic point source exclusively exciting the first order waveguide mode at the centre of our 10 by 10 unit cell sample. The acoustic signal is measured by a CUI CME-1538-100LB microphone and amplified by Reson VP2000 voltage preamplifier EC6081. A Stanford Research Systems SR830 lock-in amplifier is used to read the amplitude and phase of the acoustic signal. Two VELMEX MN10-0150-E01 motors controlled by VXM stepping motor controller are used to move the microphone and scan the acoustic field in the waveguide with a scan of 75 by 60 points and step size 7.6 mm.

Chapter 4

Parity-Time Symmetry in Acoustics

4.1 Introduction

Over the past two decades, phononic crystals have continuously attracted considerable attention both theoretically and experimentally. Based on real modulation of mass density and elastic modulus, many interesting phenomenon can be observed such as phononic band-gap [3, 53–55], double negative refraction [56], acoustic tunneling [57], and Anderson localization [58], etc. However, rare studies are focused on complex crystals with imaginary modulation of acoustic parameters. The imaginary modulation can be realized with some loss and gain mechanisms. In acoustics, the loss and gain can be provided by the inherent acoustic damping and delicate real-time acoustic feedback systems, respectively. An intriguing case is that the acoustic system respects parity-time (PT) symmetry.

Recently the notion of PT symmetry, where introduced first in quantum filed theory, adapted into the optics [59–62] and electronics [63, 64] by means of synthetic matters. This successful mapping elevated the notion of PT symmetry from a mathematical curiosity to a functional mechanism in which one can realize several intriguing physical features. These include, among others, power oscillations and nonreciprocity of light propagation [59], nonreciprocal Bloch oscillations [65], unidirectional invisibility [60, 62, 66, 67], reconfigurable Talbot effect [68] and a new class of conical diffraction [69]. In the nonlinear domain, such nonreciprocal effects can be used to realize a new generation of optical on-chip isolators and circulators [61, 69, 70]. Other results include the realization of coherent perfect laser-absorber [71, 72]. In photonics and electronics, exhibition of PT symmetric synthetic matter is feasible by implementing balanced amplification and absorption mechanisms into the optical and electronic system. A natural question that one can ask is how one can carry out the concept of PT symmetry into the acoustic structures and explore new features in this area?

In this Chapter, we introduce the concept of PT symmetry into the acoustic domain by judiciously interleaving balanced loss and gain regions. In terms of the exact analytical expression for scattering matrix, we first show that our set-up satisfies all the properties of

a PT symmetric system, namely it maintains all the conservation relations associated with a 1D PT symmetric scattering set-up. Later we exploit the non-reciprocal behavior in the reflections of the acoustic PT symmetric scatterer. We identify an interesting feature of our set-up where for a specific frequency the system becomes unidirectionally transparent. The phenomenon was first predicted in [66]. Its generalization was discussed in [73], and later experimentally verified in [62, 74]. This study makes sure that our set-up is a true realization of a PT symmetric acoustic system and displays all the novel phenomena encountered in the systems with generalized PT symmetries.

4.2 Design of PT Symmetry in Acoustics

In acoustics, a PT symmetric medium can be realized using a complex bulk modulus obeying the condition $\kappa(r) = \kappa^*(-r)$ and the mass density $\rho(r) = \rho^*(-r)$, which will be discussed in details later. The well-designed 1D PT symmetric medium is schematically shown in Figure 4.1. In the system, the acoustic waves are propagating in the z direction, which can be described by the Helmholtz Equation,

$$\frac{\partial^2 p}{\partial z^2} + \omega^2 \frac{\rho}{\kappa} p = 0, \tag{4.1}$$

with p the pressure, ω the round frequency, ρ the mass density, and κ the complex bulk modulus. Since the system respects PT symmetry, the mass density and the real part of bulk modulus are an even function of position $z = 0$, while the imaginary part of bulk modulus is an odd one. In our case, the material parameters are $\rho_p = 1.2$ kg/m^3 and $\kappa_p = 1.42 \times 10^5$ Pa for passive regions, $\rho_l = 1.49$ kg/m^3 and $\kappa_l = 1.75 \times 10^5 - 1.72 \times 10^4 j$ Pa for loss regions, $\rho_g = 1.49$ kg/m^3 and $\kappa_l = 1.75 \times 10^5 + 1.72 \times 10^4 j$ Pa for gain regions, respectively. In Figure 4.1, the scattering region ($z < |L| = 0.4815$ m) is composed of three loss/gain sections (green/red) and five passive sections in between. The length of loss or gain sections is 0.148 m, while the length of passive parts is 0.015 m.

4.3 Scattering from PT Symmetric Structures

The underlying symmetries of the scattering system, viz. PT symmetry, impose a generalized conservation relation on the scattering characteristics of the structure which has been discussed in optical framework in [73]. Following these references outside the scattering region ($z > |L|$), we can decompose the pressure field into the right and left traveling waves

$$p(z \geq |L|) = p_f^{-(+)} e^{jkz} + p_b^{+(-)} e^{-jkz}, \tag{4.2}$$

where $-(+)$ is for the left $z < -L$ (the right $z > L$) and k is the wave number. Furthermore, the scattering matrix describes the relation between the incoming and out-going incident

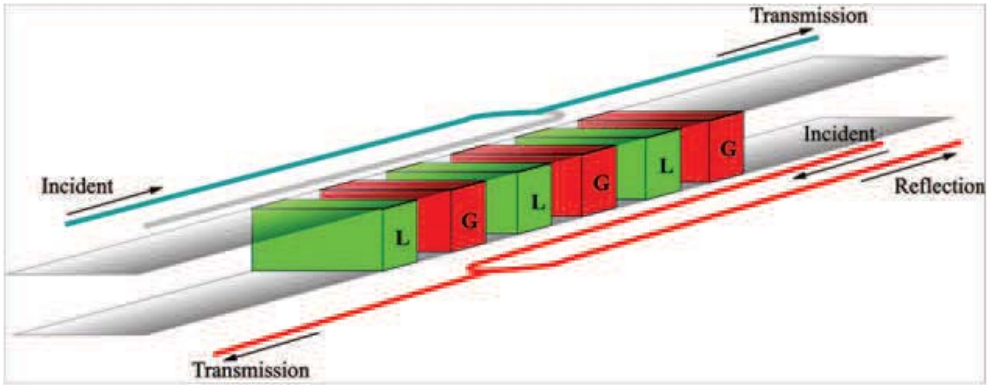


Figure 4.1: *Schematic of the acoustic PT symmetric medium. The scattering domain composed of eleven sections, three gain regions (red), three loss regions (green) and five passive regions in between. The length of the active parts is 0.148 m while the length of the passive sections is 0.015 m. The transmission and reflection of acoustic waves incident from left (blue) and right (red) are shown. This PT symmetric medium is designed to be reflectionless for acoustic waves incident from the left.*

acoustic waves in a 1D system can be expressed as

$$\begin{pmatrix} p_f^+ \\ p_b^- \end{pmatrix} = \mathbf{S}(k) \begin{pmatrix} p_f^- \\ p_b^+ \end{pmatrix} = \begin{pmatrix} t & r_R \\ r_L & t \end{pmatrix} \begin{pmatrix} p_f^- \\ p_b^+ \end{pmatrix}, \tag{4.3}$$

where r_L, r_R, and t are left and right reflection coefficients and transmission coefficients, respectively. The PT symmetric nature of the acoustic system leads to

$$\begin{pmatrix} p_f^{-*} \\ p_b^{+*} \end{pmatrix} = \mathbf{S}(k) \begin{pmatrix} p_f^{+*} \\ p_b^{-*} \end{pmatrix}, \tag{4.4}$$

A comparison between Eqs. (4.3) and (4.4) shows that $\mathbf{S}^*(k) = \mathbf{S}^{-1}(k)$. From this relation we can conclude that [73]

$$r_L r_R^* = 1 - |t|^2, \tag{4.5a}$$

$$r_L t^* + r_L^* t = 0, \tag{4.5b}$$

$$r_R t^* + r_R^* t = 0. \tag{4.5c}$$

Equation (4.5a) or its other form $\sqrt{R_L R_R} = |T - 1|$ is a generalization of the more familiar conservation relation $R + T = 1$ associated with the passive systems where the geometric mean of the two reflections $\sqrt{R_L R_R}$ replaces the single reflection R of the unitary process [73]. Existence of the left and right reflections in this general conservation relation means that in 1D acoustic PT systems the left reflection R_L can in principle be different from the right reflection R_R. An interesting result occurs when we have perfect transmission, that is $T = |t|^2 = 1$. Although, in this case, each reflection is no longer required to vanish, their product

must indeed vanish according to Eq. (4.5a). Typically, this constraint can be satisfied by one of the reflections getting to zero while the other remains non-zero or both reflections get to zero simultaneously. The later one is an accidental degeneracy and we call it bidirectional transparency. The former phenomenon is of our interest and recalls for the unidirectional transparency, since we have reflectionless perfect transparency in one direction but not the other. Based on transfer matrix method in acoustics, we have respectively calculated the phase and intensity (Figure 4.2) of left and right reflected waves and transmitted waves propagating through the well-designed PT symmetric multilayer system. According to [73], for the case $T < 1$, the phase of the left reflection and right reflection should be equivalent, while for $T > 1$, there is a π phase difference between the two reflections. Moreover for both cases there is a $\pm\pi/2$ phase difference between the transmission and reflection parts. Figure 4.2 shows our results are in agreement with these theoretical predictions. Moreover, our results in Figure 4.2 show that at the frequency $f \approx 6$ kHz, the left reflection is exactly zero and the right reflection is around 0.39, as marked by darken dots. At that frequency, the phase of left reflected waves experiences an abrupt change of π due to the changes in the transmission. This abrupt phase changes is related to the zero reflection. Due to the step function behavior of the phase, the delay time $\tau_r = d\phi_r/d\omega$ for the left reflection behaves as a delta function. As a result the reflected field will remain for a long time in the waveguide and get annihilated completely by the loss. At that frequency, the transmission is exactly unitary but the phase of transmitted waves ($\approx -0.3\pi$) is differed from the phase ($\approx -0.33\pi$) of the acoustic waves after traversing a passive region with the same length of the scattering system. Therefore, the system cannot be regarded as invisible in any case, even though the system exhibits reflectionless for the waves propagating from the left.

The transmission transition from $T < 1$ to $T > 1$ and vice versa can be related to the exact and broken phases in our acoustic PT set-up. In this respect, we shall demonstrate the frequency at which the transmission is exactly unitary is related to an exceptional point by investigating the spectral properties of scattering matrix. Following [73], when the system is in PT symmetric phase, the eigenvalues of Hamiltonian are non-degenerate and unimodular. In other words, unimodular eigenvalues correspond to the PT symmetric phase whereas non-unimodular eigenvalues, whenever they appear, signify the PT broken phase. In the acoustic system, we can derive explicit criteria for the spontaneous PT symmetry breaking transition in terms of the transmission and reflection coefficients in scattering matrix. From Eq. (4.3), the eigenvalues of scattering matrix are expressed as $\lambda_{1,2} = t \pm \sqrt{r_L r_R}$, and the eigenvectors with the first component normalized are given by $(1 \quad \pm\sqrt{r_R/r_L})^T$. Using Eqs. (4.5a) and (4.5b), we have $\lambda_{1,2} = t(1 \pm j\sqrt{(1-T)/T}$. From this relation, we can conclude that when $T < 1$, eigenvalues are unimodular and non-degenerate and we are in the so-called exact phase. However, when $T > 1$, the eigenvalues are non-unimodular and system is in the broken phase. At the exceptional point, transition between these two regions happens and we have $T = 1$.

In Figure 4.2, we plotted the absolute values of the eigenvalues of scattering matrix, from which the exceptional point can be observed at $f \approx 6$ kHz, as marked by a darken dot.

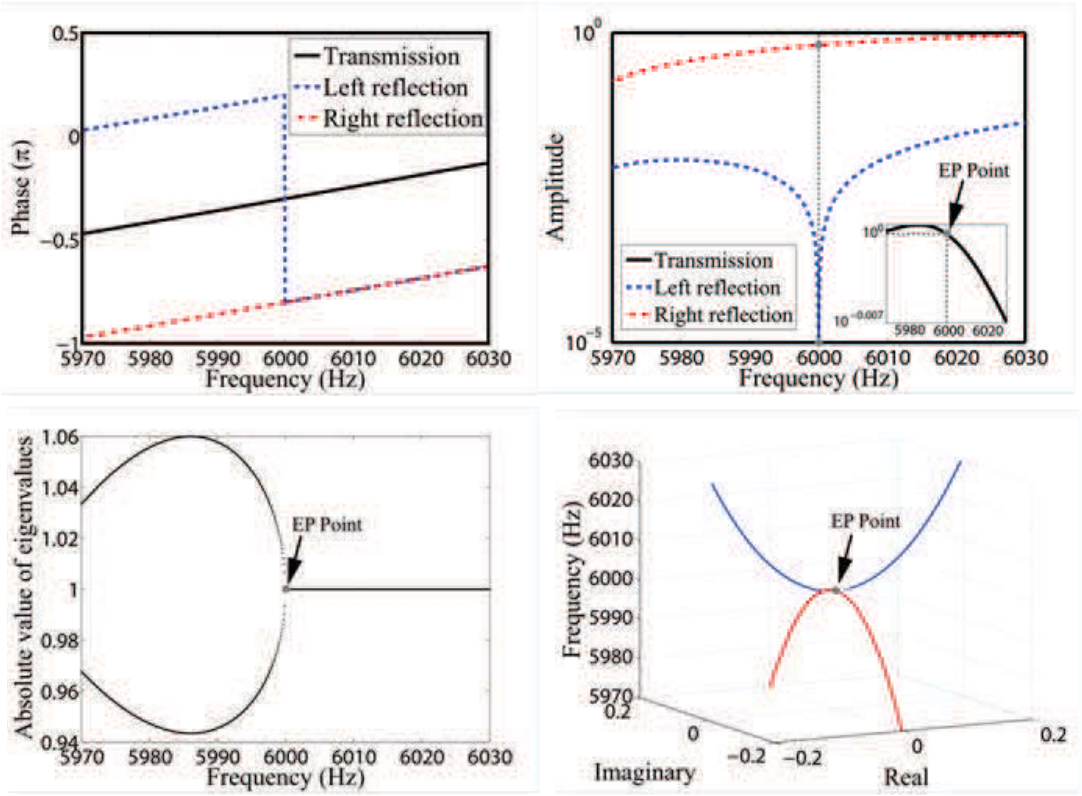


Figure 4.2: *Phases and intensities of left reflected, right reflected, and transmitted waves of the PT acoustic symmetric medium are shown in (a) and (b), respectively. The absolute value of the eigenvalues and the second component of the eigenvectors of the corresponding scattering matrix of this PT acoustic symmetric medium are shown in (c) and (d). We normalized the eigenvectors such that the first component is always unitary.*

Below the exceptional point, the eigenvalues are non-unimodular, the transmission $T > 1$ (Figure 4.2), and the system is in the broken phase. While above the exceptional point, the eigenvalues are unimodular, the transmission $T < 1$ (Figure 4.2), and the system is in the PT symmetric phase. At the exceptional point, the transmission $T = 1$ (Figure 4.2), and the system is unidirectionally reflectionless. Moreover, in Figure 4.2, we plot the second component of the eigenvectors of scattering matrix. The blue curve corresponds to the PT symmetric phase, where the eigenvectors are real and clearly they are invariant under conjugation [73]. In the broken phase (red curve), the second components of the eigenvectors are purely imaginary and under conjugation one of the components transforms into the other.

We also carry out full-wave simulations using a finite element solver (COMSOL Multiphysics) to verify the unidirectional reflectionless effect of the well-designed 1D PT symmetric medium, as shown in Figure 4.3. In the numerical simulations, the plane wave is incoming from the left and right directions, respectively, with the frequency located at the exceptional

point. The interference pattern due to strong Bragg reflection is visualized for the right incidence, whereas the scattered acoustic waves are barely observed for the left incidence. It is interesting to point out that the pressure field for the left incidence is equally distributed in the loss and gain parts with the field distribution symmetric to the position $z = 0$, indicating the energy produced by the acoustic gain is completely absorbed by the loss in the mirrored position. However, when the waves are incoming from the right, the pressure field is more localized in the gain parts and the extra energy from the gain after balanced out by the loss provides the strong Bragg reflection.

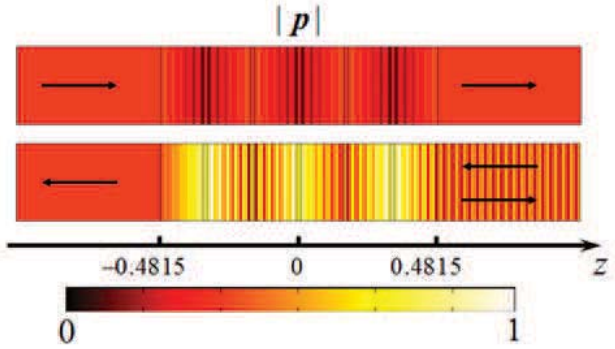


Figure 4.3: *The normalized amplitude of pressure field for the left and right incidences at the exceptional point, respectively.*

4.4 Directional Cloaking with PT Symmetry

Since the acoustic wave equation is invariant under coordinate transformation [32, 75–77], it is possible to combine PT symmetric medium with transformation acoustics to design myriad transformation acoustics devices of unidirectional responses. As an example, we will show how to design a 2D PT symmetric acoustic cloak that is one-way invisible. First, we need to construct a PT symmetric periodic structure with unidirectional invisibility in the virtual space (r, θ), for which the complex modulation of material parameters should take the unique form of $\delta \exp(j\beta \cdot \mathbf{r})$ rather than the generalized one exemplified in Figure 4.1, where δ and $2\pi/|\beta|$ are the amplitude and periodicity of modulation, respectively. In our case, the density and complex bulk modulus of the unidirectionally invisible PT symmetric periodic structure are $\rho_0 = 1.2$ kg/m^3 and $\kappa_0 = 1.42 \times 10^5[1 + 0.1\exp(j219.7r\cos\theta)]$ Pa, respectively, in the virtual space (r, θ). In cylindrical coordinates, a mapping between virtual space (r, θ) and real space (r', θ') to produce a 2D acoustic cloak of cylindrical geometry can be expressed as $r = f(r')$ and $\theta = \theta'$, with $f(r') = b(r' - a)/(b - a)$ for $a \leq r' < b$. Here, a and b are the inner and outer radii of the acoustic cloaking shell, which are 0.05 m and 0.1 m in our numerical simulations. With the transformation acoustic equations in orthogonal

coordinates, we have the material parameters [15]

$$\rho'_r = \rho_0 \frac{r'}{r'-a}, \tag{4.6a}$$

$$\rho'_\theta = \rho_0 \frac{r'-a}{r'}, \tag{4.6b}$$

$$\kappa' = (\frac{b-a}{b})^2 \frac{r'}{r'-a} \kappa_0(f(r'), \theta'), \tag{4.6c}$$

for the PT symmetric acoustic cloak in real space (r', θ'). As a matter of fact, the specific modulation in the form of $\delta \exp(j\beta \cdot \mathbf{r})$ can be regarded as a complex grating that can provide a one-way wave vector β. The interaction between incident plane waves of wave vector $\mathbf{k}_1$ and the complex grating will produce a diffraction mode with the spatial frequency being $\mathbf{k}_1 + \beta$. The mode transition between incident plane waves and the diffraction mode can take place only when the phase matching condition is approximately satisfied, viz. $\delta = |\mathbf{k}_1 + \beta - \mathbf{k_2}| \approx 0$, where $\mathbf{k}_2$ is the spatial frequency of the excited diffraction mode propagating in the surrounding medium and therefore $|\mathbf{k}_1| = |\mathbf{k}_2|$. On the other hand, if $\delta \neq 0$, the energy transferred to the diffraction mode is negligible due to the momentum mismatch. The proposed one-way invisibility of PT symmetric cloak is validated in Figure 4.4. For left incidence in virtual space, strong Bragg reflection is observed in terms of the satisfied phase-matching condition $\mathbf{k}_2 \approx \mathbf{k}_1 + \beta$, as shown by the inset vector diagram in Figure 4.4. However, for right incidence in Figure 4.4, scattered waves can hardly be visualized due to phase mismatch and the waves are propagating through the PT symmetric medium as if there is a bulk of surrounding medium. From the vector diagram in Figure 4.4, a diffraction mode with the spatial frequency $\mathbf{k}_1 + \beta$ will be much larger than $\mathbf{k}_2$ and thus can hardly be excited since it falls into the evanescent regime. Figure 4.4 show the corresponding simulations of PT symmetric acoustic cloak in real space after coordinate transformation, where the pressure field distribution in both incidences agree well with the results in virtual space. It is clearly shown that an arbitrary object positioned in a rigid cylinder is perfectly concealed and one-way cloaked by the transformed PT symmetric medium. It is worth mentioning that for left incidence in Figure 4.4, the concealed rigid cylinder still remains invisible to the observer on the right, which is due to the reason that the designed phase matching is only satisfied for the backward reflection. It is also possible to make the phase matching condition satisfied for the forward reflection, which requires engineering of the direction and periodicity of the complex modulation of material parameters. However, the reflection parts can never be in the same direction of incident waves under the constraint of Lorentz reciprocity in this linear and static system. The complex modulation of material parameters can also be designed along the radial direction, viz. $\delta \exp(j\beta \cdot \mathbf{r})$, where the anisotropic transformed PT symmetric medium can be realized by alternatively stacking concentric loss and gain layers with isotropic material parameters, as indicated by the reducible cloak designing in [77].

For the generalized PT -symmetric structure exemplified in Figure 4.1, it is shown that the unidirectionality is very sensitive to frequency. However, for PT -symmetric potentials taking

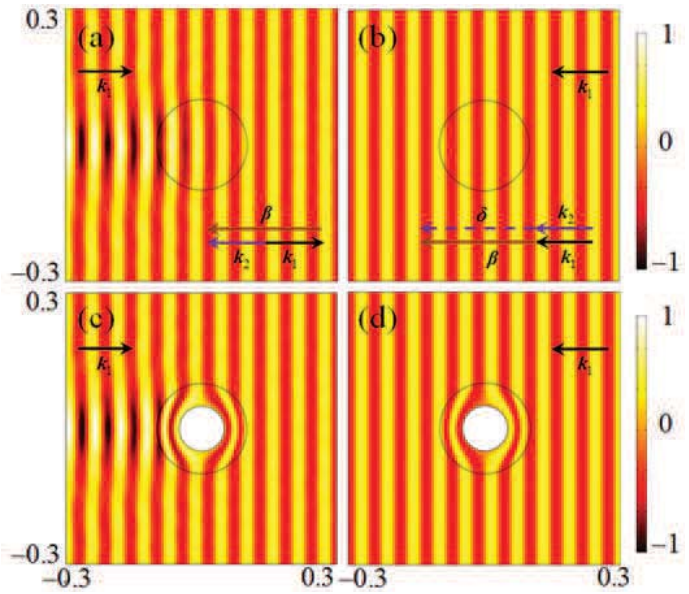


Figure 4.4: *The pressure field maps in the virtual space (a), (b) and the physical space (c), (d) one-way invisible PT symmetric cloak. In (a) and (c) where the plane wave is incoming from left, strong backscattered reflection can be observed due to the satisfied phase matching and therefore the observers on the left can sense the existence of the cloak. However in (b) and (d) where the plane wave is incident from right, the waves propagate without any scattering due to phase mismatching and thus an arbitrary object is perfectly concealed in the white region.*

the unique form of $\delta \exp(j\beta \cdot \mathbf{r})$, it has a broadband unidirectional response from 5 to 8 kHz, as demonstrated in Figure 4.5, since the scattering cross section is close to zero due to the phase mismatch for right-side-incoming waves of different frequencies, whereas the scattered waves will be visualized for the nonignorable scattering cross section in a relatively broad frequency band when the phase-matching condition is approximately satisfied for left-side incidence [78]. It also should be mentioned that for the PT-cloaking device, the singularity at the inner boundary of the cloak may limit the operating bandwidth and narrows this band of functionality in practice. Moreover, Figure 4.5 depicts the scattering cross section versus the angle of incidence at the frequency of 6 kHz, where the unidirectional invisibility also holds for an oblique angle of $|\theta| < \pi/6$.

A one-way invisible 2D PT symmetric acoustic ground cloak [17] is also designed using our PT symmetric medium. We perform the full-wave simulation using the $\rho_0 = 1.2$ kg/m^3 and $\kappa_0 = 1.42 \times 10^5[1 + 0.03\exp(j2\pi z/(0.4\sqrt{2}))]$ Pa ($1.4 < x < 11.4$ and $|z| < 10$). This acoustic ground cloak can be observed from the left because of the strong back reflection caused by Bragg scattering (Figure 4.6), whereas the cloaked region is invisible from the right due to phase mismatching (Figure 4.6).

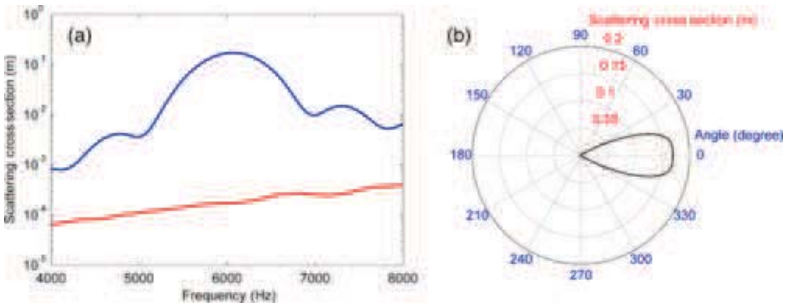


Figure 4.5: *(a) Scattering cross section versus frequency, where the blue (upper) and red (lower) curves describe the scattering cross section of the PT-symmetric cloak when the light is incoming from the left and right, respectively. (b) Scattering cross section versus the incident angle at the frequency 6 kHz, where* $\theta = 0$ *corresponds to the parallel propagation along the z direction from left to right.*

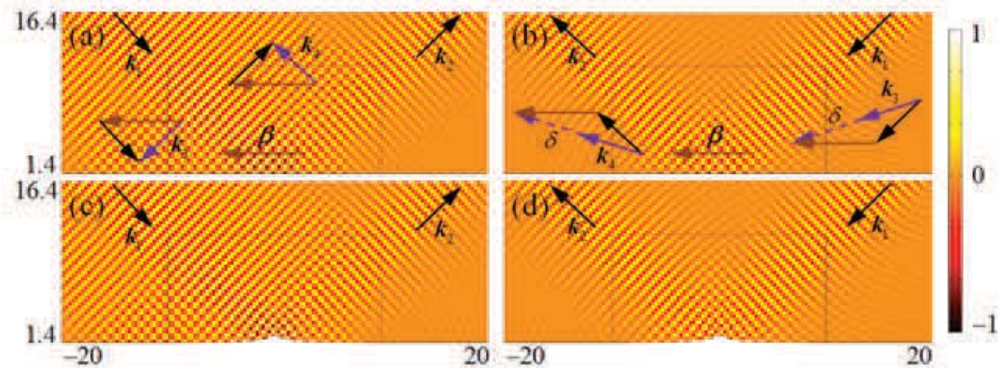


Figure 4.6: *The pressure field maps in the virtual space (a), (b) and the physical space (c), (d) for one-way invisible PT symmetric acoustic ground cloak. In (a) and (c) where the plane wave is incoming from left, strong back reflection can be observed due to the satisfied phase matching and therefore the observers on the left can sense the existence of the ground cloak. However in (b) and (d) where the plane wave is incident from right, the waves propagate without any scattering due to phase mismatching and thus an arbitrary object can be concealed in the bump region.*

4.5 Discussions

In conclusion, we have introduced the concept of PT symmetry into acoustics and demonstrate the phenomenon of unidirectional transparency at the exceptional points in the non-Hermitian acoustic system. With a unique form of complex modulation of material parameters, the PT symmetric medium can further exhibit unidirectional invisibility, which can be employed to design a one-way invisible PT symmetric cloak under transformation acoustics.

Our results will offer great material design flexibility and additional freedoms for developing novel acoustic devices.

Chapter 5

Exceptional Points of PT-Symmetric Acoustics

5.1 Introduction

Non-reciprocal wave transport is important for key applications such as isolators [79–81], diodes [25, 82], and rectifiers [83, 84], etc. However, these schemes rely on high-order harmonic generation, mode conversion or angular dependent bandgap in order to realize asymmetric transmission. Recent progress on parity-time (PT) symmetric systems provides a new paradigm to realize asymmetric transport without frequency or mode conversion [26, 59–62, 66, 85–91]. Only at specific frequencies called exceptional points, complex interference in PT symmetric systems results in unidirectional reflection that is crucial for applications [60, 66, 73]. However, PT symmetric systems require an exact balance of loss and gain in the medium, and the dispersive behavior of most loss and gain materials prevents this condition to be fulfilled over a broad frequency range. Hence, it is challenging to access the exceptional points in practice. Here, we present a general method to approach the exceptional points within a large frequency range by tuning an acoustic gain medium that satisfies the PT symmetric condition and simultaneously controls the scattering process. For the first time, we experimentally demonstrate the ability to reverse the direction of the acoustic transparency at any given frequency. Such control of directional transparency opens new routes for wave physics including acoustics and electromagnetics, and important applications in sensing, communication and imaging.

PT symmetric systems are invariant under parity and time reversal operations. Therefore, they obey the following energy conservation relation

$$r_l r_g* = 1 - |t|^2, \tag{5.1}$$

where t is the transmission coefficient, r_l is the reflection coefficient from the loss side, and r_g is the reflection coefficient from the gain side of the system [26, 66]. In PT symmetric systems, phase transition where the system Hamiltonian switches between real and complex

spectrum [92, 93] provides a novel approach to realize asymmetric transport. This phase transition has been intensely studied in electronics [63, 64], optics [59–62, 66, 85, 86, 90, 91, 94–96], acoustics [26, 88], etc. The right-hand side sign of Eq. (5.1) determines the PT phase of the system: positive for PT "exact phase", and negative for PT "broken phase" [26, 66]. When the system undergoes phase transition, transmission is unity, $|t| = 1$, corresponding to the existence of exceptional points. Therefore, one of the reflections must vanish at these exceptional points, typically resulting in unidirectional transparency.

The PT symmetric condition requires the distribution of complex refractive index to be a Hermitian function in the transverse direction such that $n(x) = n^*(-x)$ [59, 60]. This distribution is achieved by precisely balancing loss and gain materials. However, as the complex refractive indices of most natural materials are dispersive, the PT symmetric condition often occurs at a single frequency or in a very narrow band of frequencies, making the observation of exceptional points difficult. Here, we introduce a method to systematically tame these exceptional points and control PT phases. Our experimental demonstration hinges on an active acoustic element that realizes a complex-valued potential and simultaneously controls the multiple interference in the structure. The manipulation of exceptional points offers new routes to broaden applications for PT symmetric physics in acoustics, optics, microwaves, electronics, which are essential for sensing, communication, and imaging.

5.2 Tailoring the Exceptional Points of PT Symmetric Structure

Figure 5.1 illustrates the control of exceptional points for typical dispersive loss and gain materials, the imaginary parts of their indices are balanced at a single frequency f_b. When there is no spacing between the loss and gain materials (Figure 5.1)), one can observe reflections from both sides, and not be able to access exceptional points. Exceptional points and unidirectional transparency are the results of complex interference inside the PT symmetric structure. This scattering process can be controlled by introducing a gap corresponding to a phase delay between the gain and loss cells (Figure 5.1). Analytic calculations based on transfer-matrix formalism are used to scan the response of the structure as a function of spacing and frequency. The reflection from the loss side (Figure 5.1) presents a sharp dip for a specific spacing L_0 at frequency f_b, where the multi-reflection interfere destructively. In this case, one can access an exceptional point where the reflection from the loss side vanishes while achieving total transmission and nonzero reflection from the gain side, making the system to be unidirectional transparent (Figure 5.1).

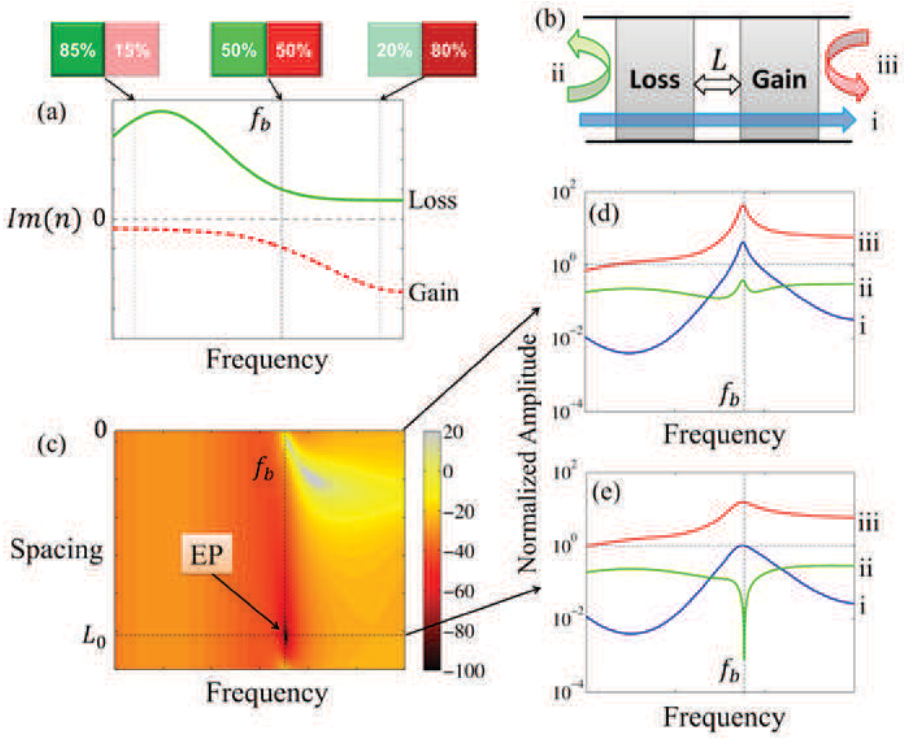


Figure 5.1: *Accessing the exceptional point of acoustic PT system by tuning the spacing between loss and gain materials. (a) Imaginary parts of the refractive indices of loss and gain materials are typically dispersive, so the PT symmetric condition could only be satisfied at single frequency f_b where the loss and gain materials are exactly balanced. (b) Loss and gain materials assembled with spacing. (c) Amplitude of the reflection from the loss side as a function of frequency and the spacing between the loss and gain materials. Exceptional point (EP) occurs at frequency f_b and a specific spacing L_0 when the reflection vanishes. (d) The normalized transmissions (blue, i), reflections from the loss (green, ii) and from the gain (red, iii) in logarithmic scale without spacing, no exceptional point observed. (e) Similar representation to (d) with spacing L_0, an exceptional point observed at f_b.*

5.3 Experimental Demonstration of Unidirectional Transparency

Recent development in PT symmetric acoustics promises new applications such as asymmetric cloaking and sensing [26, 88]. The control of exceptional points is crucial for the design of such devices. The realization of PT symmetric acoustics relies on the combination of acoustic loss and gain materials. It has been shown that active elements can be tuned to obtain artificial materials with desired effective acoustic parameters. This was demonstrated in the modulation of the real part of the acoustic parameters [97]. In this work, we explore

the acoustic parameters in the complex domain to exploit non-Hermitian physics and the control of exception points.

In our experiments, coherent acoustic sources are used to generate a gain response that balances a passive loss material and satisfies the PT symmetric condition. Our acoustic prototype consists of one loss cell where multiple slits are carved in a waveguide to form a leaky region, and one gain unit formed by two acoustic source arrays paired with upstream and downstream highly directive sensors (Figure 5.2). We first obtain the scattering matrix of the loss part at 5.3 kHz by measuring the amplitude and phase of transmission and reflection without the gain unit. This frequency corresponds to a local maximum of the loss parameters, resulting in high contrast between the reflections of the PT symmetric system (Figure 5.3). A parameter extraction algorithm is used to retrieve the effective parameters of the loss material from the measured scattering matrix at 5.3 kHz [52]. The calculated mass density is $\rho = 1.13\exp(-j0.68)$ kg/m^3 and bulk modulus is $\kappa = 0.16\exp(-j0.87)$ MPa(refractive index is $n = c_0\sqrt{\rho/\kappa} = 0.9 + 0.09j$ with $c_0 = 343$ m/s). Effective parameters of the gain medium are obtained by complex conjugation, and the same algorithm can be reversed to calculate the gain scattering matrix. By tuning the two acoustic source arrays to match this scattering matrix, the PT symmetric condition can be satisfied at 5.3 kHz. As discussed previously, exceptional point occurrences are dictated by the multiple interferences within the structure. In our experiment, these interferences are controlled by the spacing between the loss and gain materials. Analytical calculation at 5.3 kHz reveals that 1.24 cm spacing results in unidirectional transparency from the loss side. The loss region and the balanced gain unit are assembled in a waveguide with the correct spacing. The scattering matrix of the entire system is measured by two calibrated microphone pairs

$$|\mathbf{S}| = \begin{pmatrix} |t_l| & |r_g| \\ |r_l| & |t_g| \end{pmatrix} = \begin{pmatrix} 0.99 & 3.34 \\ 0.02 & 1.02 \end{pmatrix}. \tag{5.2}$$

The experimental results confirm the unidirectional transparency from the loss side, which agree well with the analytical predictions (Figure 5.2).

5.4 Accessing Exceptional Points at Multiple Frequencies

One major benefit of using active gain material is that the PT symmetric condition can be satisfied over a large frequency band, regardless of the loss material dispersion. We demonstrate that unidirectional transparency is achieved by controlling exceptional points for different frequencies within the range of 5 6 kHz. The scattering matrices of the leaky waveguide are measured at four frequencies and the retrieved refractive indices confirm the dispersive behavior of our loss part (Figure 5.3). The complex conjugates of these indices are used to calculate the scattering matrices of the gain material at each frequency. In order to observe unidirectional transparency at these frequencies, different spacings are required

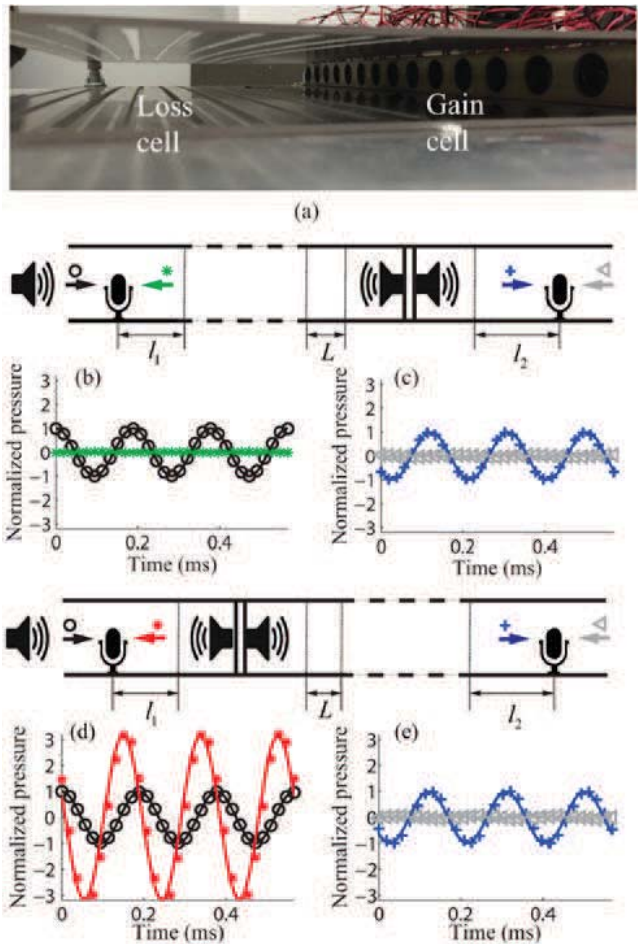


Figure 5.2: *Experiment demonstration of unidirectional transparency of the PT symmetric system at 5.3 kHz. (a) The photo of an experimental sample including loss and gain units. (b), (c) The calculated (solid curves) and measured (marked dots) transmissions and reflections when the incident wave is coming from the loss side. (d), (e) Similar representation to (b), (c) when the incident wave is from the gain side. Black, green, red, blue, and gray colors denote the incidence, reflection from the loss side, the reflection from the gain side, the transmission, and the reflection from the end of the waveguide, respectively. All results have been normalized with the amplitude of incidence. The two calibrated unidirectional microphones are mounted at* $l_1 = 15.5$ *cm and* $l_2 = 13$ *cm away from the boundaries of our PT symmetric materials. The spacing between the loss and gain materials is* $L = 1.24$ *cm. No reflection is observed from the loss side (green curve and dots in (b)), about* 330% *reflection is observed from the gain side (red curve and dots in (d)), and total transmissions* ($|t| = 1$) *have been observed on both sides, resulting in unidirectional transparency from the loss side.*

in the system. The calculated spacing distances and the measured scattering matrices are listed in Figure 5.3. By applying opposite phase shifts to the two acoustic source arrays, we introduce an effective spatial offset between the gain medium and these emitting arrays. The phase shifts allow us to set the effective spacing between the loss and gain materials in a fixed structure for each frequency (see Section 5.6). For all measurements, total transmissions through the PT symmetric system can be observed within 2% error, the reflections from the loss side vanish ($< 3\%$), and the reflections from the gain side are nonzero. It is important to point out that both the loss and gain units are working in linear conditions. Thus, the system will preserve the unidirectional reflection when input signals are linear combinations of the demonstrated frequencies, promising time-dependent signal applications.

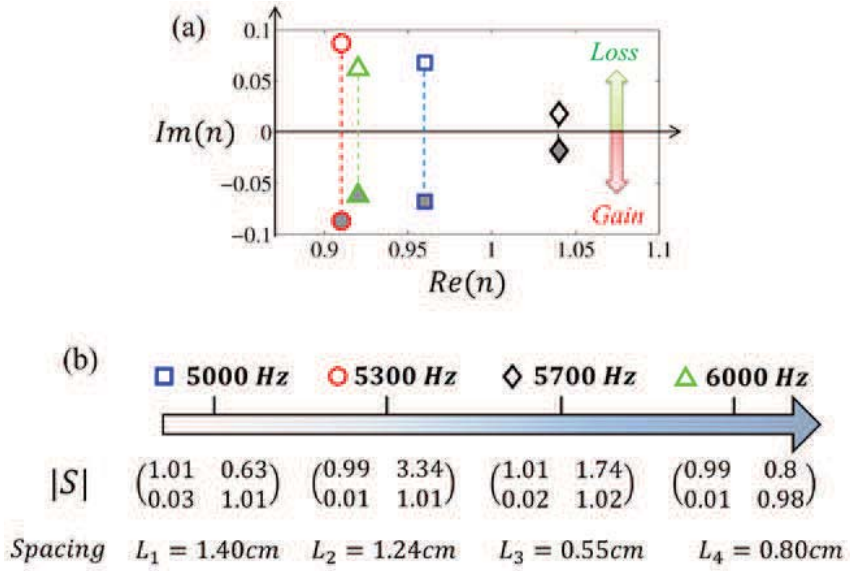


Figure 5.3: *Taming exceptional points at different frequencies. (a) The measured complex-valued refractive indices of the loss material formed by the leaky waveguide at 5 kHz, 5.3 kHz, 5.7 kHz, and 6 kHz (open marks). The active gain material is tuned to have the refractive indices that are complex conjugate of those of the loss material at the corresponding frequencies (filled marks). (b) The measured amplitudes of the scattering matrices for the controlled exceptional points at these four frequencies with the appropriately tuned spacing between the loss and gain materials. The reflections from the loss side almost vanish and total transmissions are observed for all of the frequencies. The reflections from the gain side are nonzero.*

5.5 Reversing the Orientation of Unidirectional Transparency

Previous studies in optics and acoustics only demonstrate unidirectional transparency from the loss side [59, 88], whereas Eq. (5.1) reveals that two types of exceptional points exist depending on the side where reflection is cancelled. Here we demonstrate that our method can control the orientation of unidirectional transparency at the same working frequency, which is useful for applications such as logical acoustics. Figure 5.4 presents the transmission and reflection coefficients of the PT symmetric system as functions of spacing. These coefficients are periodic functions with period $\lambda/2$. Within this scope, two exceptional points are observed. The same as shown in Figure 5.2, reflection from the loss side vanishes with 1.24 cm spacing. The other exceptional point occurs at 1.71 cm spacing, where the reflection from the gain side is cancelled. Figure 5.4 show the transmissions and reflections normalized with their inputs for these two different gaps. In both cases, we can observe total transmissions of waves. Once we tune the spacing to be 1.71 cm, 70% reflection from the loss side is observed while the reflection from the gain side is less than 8%. The experimental results agree well with the analytical predictions, and prove that the orientation of the unidirectional transparency can be controlled by tuning the spacing between the loss and gain materials within half wavelength.

5.6 Measured Scattering Matrix at 5.3 kHz

The measured scattering matrix of the loss unit form by the leaky waveguide is

$$\mathbf{S}_{\text{loss}} = \begin{pmatrix} t_l & r_l \\ r_l & t_l \end{pmatrix} = \begin{pmatrix} 0.33\exp(-27^o j) & 0.39\exp(95^o j) \\ 0.39\exp(95^o j) & 0.33\exp(-27^o j) \end{pmatrix}, \tag{5.3}$$

with transmission coefficient t_l and reflection coefficient r_l of the loss part. The effective loss parameters are retrieved from this scattering matrix. The gain scattering matrix is calculated using the complex conjugate of the loss parameters

$$\mathbf{S}_{\text{gain}} = \begin{pmatrix} t_g & r_g \\ r_g & t_g \end{pmatrix} = \begin{pmatrix} 1.49\exp(11^o j) & 1.75\exp(69^o j) \\ 1.75\exp(69^o j) & 1.49\exp(11^o j) \end{pmatrix}, \tag{5.4}$$

After tuning the active gain unit to present this scattering matrix and tuning the spacing between the loss and gain units to 1.24 cm, the scattering matrix of the entire PT symmetric system is measured

$$\mathbf{S} = \begin{pmatrix} t_l & r_g \\ r_l & t_g \end{pmatrix} = \begin{pmatrix} 0.99\exp(130^o j) & 3.34\exp(63^o j) \\ 0.02\exp(167^o j) & 1.02\exp(118^o j) \end{pmatrix}, \tag{5.5}$$

Considering the wave propagation between the boundaries of the PT symmetric system and the two microphone pairs, the calculated transmission and reflection coefficients are $t = \exp(128^o j)$ and $r_g = 3.17\exp(75^o j)$. The measured amplitudes are within 5% relative error, and the measured phases are within 3% relative error.

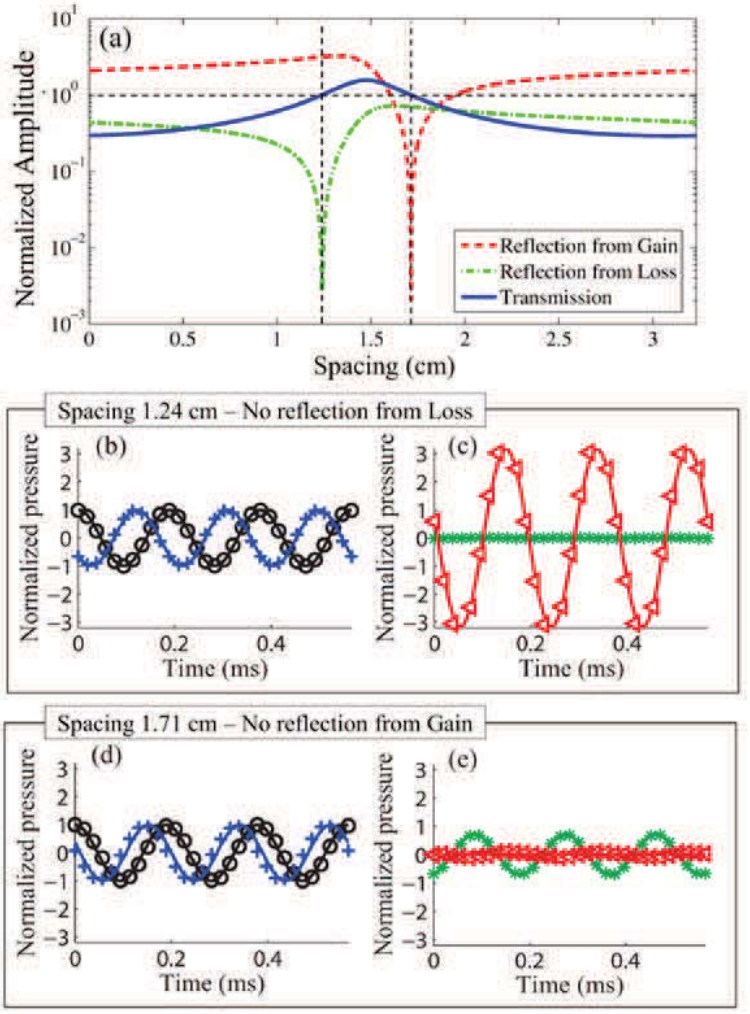


Figure 5.4: *Reversing the unidirectional transparency at 5.3 kHz. (a) Calculated transmission (blue) and reflections from the gain side (orange) and the loss side (red) with varying spacing between the loss and gain materials from zero to half wavelength. Two exceptional points are observed when the spacing is 1.24 cm and 1.71 cm, respectively. (b), (c) Transmission and reflections from the gain and loss sides associated with 1.24 cm spacing. Black, blue, red and green colors denote the incidence, transmission, reflection from the gain side, and reflection from the loss side, respectively. Solid curves are calculated values and marked dots are from measurements. The same as Figure 5.2, unidirectional transparency is observed from the loss side. (d), (e) Similar representation to (b), (c), but with 1.71 cm spacing. The direction of unidirectional transparency is reversed. Nearly zero reflection from gain side and* 70% *reflection from the loss side are observed.*

5.7 Method of Control the Artificial Gain Material

Different from the conventional opinion that acoustic gain materials only have the function to amplify acoustic signals, actual acoustic gain media, if exist, create a certain scattering pattern whose transmission and reflection coefficients are specific and determined by the effective parameters. To mimic an actual acoustic gain material, we need to tune our active gain unit to generate the same scattering matrix. This section discusses the method to control the scattering matrix and virtual position of our active gain unit to mimic the behavior of an actual acoustic gain material that is precisely balance with the loss part at an arbitrary frequency and tuning the spacing between these loss and gain units to control and explore the exceptional points.

As presented in Figure 5.5, our experiment starts with measuring the scattering matrix of the loss part form by the slits shown in Figure 5.2. The loss unit is assembled in an acoustic waveguide with reflectionless ends. Two calibrated unidirectional microphone pairs (discussed in Section 5.8) are placed on two sides of the loss unit to measure the incidence, transmission, and reflection in the system at a chosen frequency below 6 kHz. An acoustic source formed by fifteen speakers that can generate acoustic plane waves lower than 6 kHz in the waveguide is used to generate the incident wave for the measurement. The measured transmission and reflection coefficients, i.e. scattering matrix, are used to extract the effective parameters at this frequency using the method discussed in [52]. To satisfy the PT symmetric condition, the effective parameters of the actual gain material we need to use are complex conjugates of those of the loss material (Figure 5.5). Thus, the scattering matrix of the gain material is calculated using these effective parameters, and this scattering matrix is the one our artificial gain material needs to generate in our experiment. This artificial gain contains two speaker arrays and two calibrated highly directional microphone pairs. The acoustic waves emitted by the speaker arrays are tuned according to the measured signal from the microphone pairs so that the scattering matrix of the gain unit remains the same for any incident waves. The virtual position of our artificial gain material, which tunes the spacing between the loss and gain materials, is controlled by modifying the phases of the two speaker arrays used in the gain unit. The appropriate value of the spacing that allows us to observe the exceptional point and realizes unidirectional transparency is calculated by sweeping the spacing size between zero and half wavelength using a transfer matrix method. With the appropriate spacing and the measured parameters of the loss and gain materials, the total scattering matrix of the system is calculated and used to tune the artificial gain unit in our experiment.

A linear control method is used to tune the active gain unit formed by two speaker arrays (identical to the one that generates the incident wave) that generates acoustic plane waves between 5 kHz and 6 kHz in the waveguide. The loss and gain units are assembled in a wavelength with reflectionless ends, where two pre-calibrated unidirectional microphone pairs are placed on the two sides of the unit cell formed by these loss and gain units to measure the transmission and reflection coefficients of the entire system. Because the system is linear, the detected signals of the unidirectional microphone pairs are linear combinations

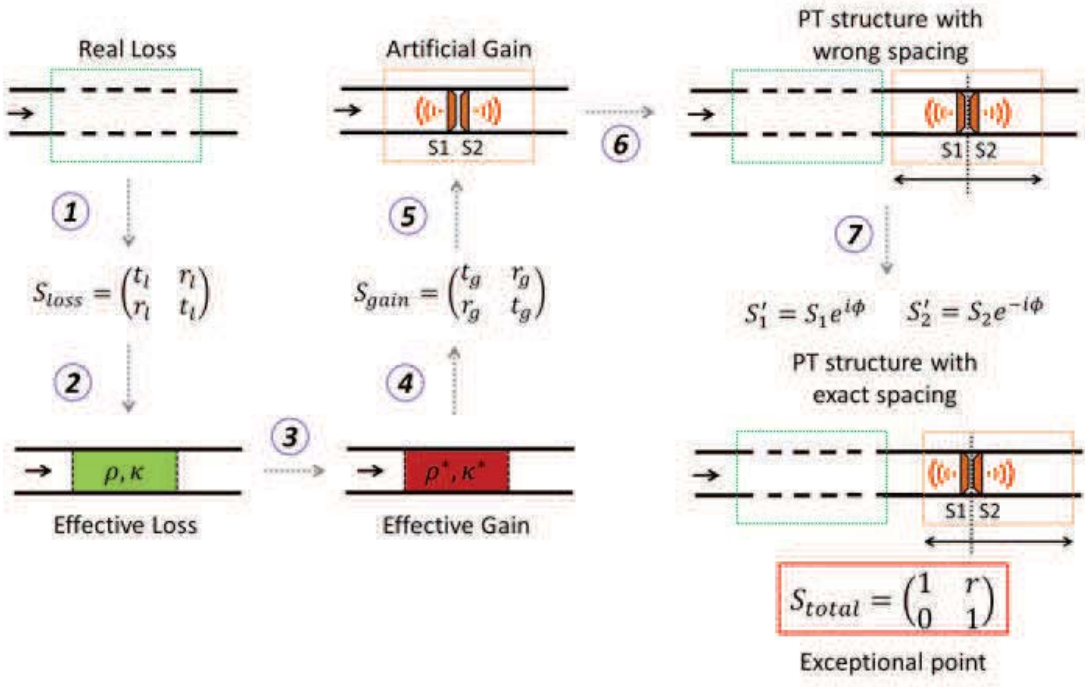


Figure 5.5: *Seven experimental steps of realizing unidirectional transparency and observing exceptional points in PT symmetric systems. (1) Measuring the scattering matrix of the loss material. (2) Retrieving the effective parameters of the loss material. (3) Calculating the effective parameters of the gain material. (4) Deriving the scattering matrix of the gain material using the calculated effective parameters. (5) Tuning the active gain unit to mimic the actual gain material needed in the system when the entire structure is assembled. (6) Satisfying the PT symmetric condition where the loss and gain materials are precisely balanced. (7) Tuning the spacing between the loss and gain materials by apply opposite electrical phase shifts to the two active emitters to control the exceptional point and realize unidirectional transparency.*

of the system responses to the three speaker arrays installed in the setup. Therefore, we turn only one of the speaker arrays on each time and record the incidence, transmission, and reflection in the system. After we finish these measurements for the three speaker arrays, a matrix relating the emissions of the speaker arrays and the system response is generated. By inverting this measured matrix and applying the desired system response at the exceptional point, we calculate the expected emissions of these three speaker arrays. With these calculated expected speaker emissions, we tune our active gain unit to observe the unidirectional transparency of the system. All the above calibration and tuning procedures are performed for the cases when acoustic wave incidents from the loss and gain sides separately. The two microphone pairs have two functions: 1. measuring the scattering matrix of the entire

system; 2. providing the feedback signal so that the two gain speaker arrays can be tuned accordingly. Because our system is linear, the scattering matrix of the gain material is the one we calculated previously when the scattering matrix of the entire system is tuned to the desired values.

5.8 Calibration of Unidirectional Microphone Pairs

Unidirectional microphones that only measure acoustic waves travel in one direction are crucial for our measurement of the incidence, transmission, and reflection in the system. To realize such unidirectional microphones, we use two PUI Audio PUM-5250L-R microphones to form a microphone pair. Even though these microphones are labeled as unidirectional microphones, they still detect some of the signals incident from the back side. For the same incident wave, the amplitudes of the signals measured by the microphone when it is facing towards the incident wave (A_f) and the opposite direction are different (A_b). We define the ratio of these two amplitudes $R = A_b/A_f$ to be the back-front-ratio of the microphone. This ratio varies with frequency and is different for each microphone. A waveguide with reflectionless ends is used for the calibration of the unidirectional microphone pairs (Figure 5.6). The two microphones are fixed on a thin metal strip that can be assembled in the waveguide facing opposite directions. A speaker array discussed in Section I is used to generate the incident wave for this calibration. After the microphone pair is assembled in the waveguide, we record the measured signals of the two microphones m_{11} and m_{21}. Then we rotate the microphone pair 180^o and assemble it at the same position and record the two measured signals m_{12} and m_{22}. Because the waveguide has reflectionless ends, only the acoustic wave generated by the speaker array travelling in one direction exists in the waveguide. Thus, the back-front-ratios of the two microphones are $R_1 = |m_{12}/m_{11}|$ and $R_2 = |m_{21}/m_{22}|$. The phases of the measured signals m_{11} and m_{21} are calibrated to be the same because the two microphones are mount at the same location where they should detect the same phase information.

When acoustic waves propagating in opposite directions exist in the waveguide (Figure 5.6), we can use the measured back-front-ratios of the two microphones to form a unidirectional operation and extract the signals of the left and right propagating waves I_l and I_r. The detected signals of the two microphones are

$$m_1 = I_l + R_1 I_r, \tag{5.6a}$$

$$m_2 = R_2 I_l + I_r. \tag{5.6b}$$

Solving Eq. (5.6) for the two propagating waves, one can obtain the unidirectional operation to calibrate this microphone pair

$$I_l = \frac{m_1 - R_1 m_2}{1 - R_1 R_2}, \tag{5.7a}$$

$$I_2 = \frac{m_2 - R_2 m_1}{1 - R_1 R_2}. \tag{5.7b}$$

Because the back-front-ratio varies with frequency for each microphone, we need to calibrate the microphone pairs for every experimental frequency.

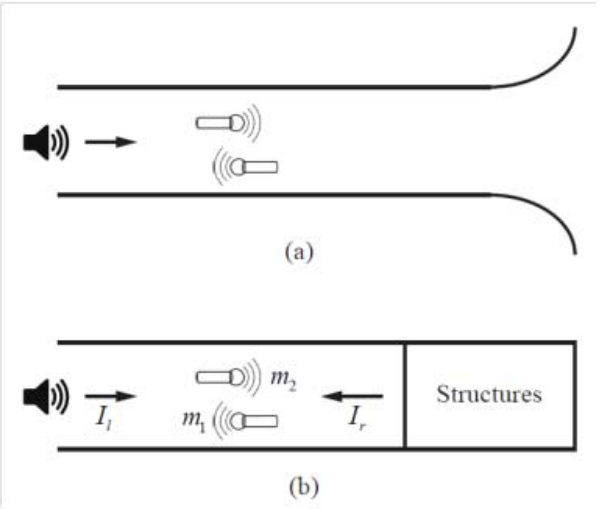


Figure 5.6: *Calibration of unidirectional microphone pair. (a) Microphone pair mounted in a waveguide with reflectionless ends to measure the back-front-ratio of each microphone. (b) Microphone pair assembled in a waveguide where the structures cause reflection of the incident wave, and hence left and right propagating waves exist in the waveguide.*

5.9 Experimental Result without Spacing Control

To demonstrate that the tuning of spacing is crucial for controlling exceptional points and realizing unidirectional transparency, we perform a control experiment at 5.3 kHz in a system where the loss and gain units are assembled side by side without spacing. The calculated and measured transmissions and reflections from the loss and gain sides are shown in Figure 5.7. Only 29% transmission is observed on both sides of the system. The reflection from the loss side is 44%, and the one from the gain side is 210%. Although the two reflections are still different, the system is not unidirectional reflectionless. This experimental result reveals that the system is not operating at the exceptional points. Unidirectional transparency cannot be observed without tuning the spacing.

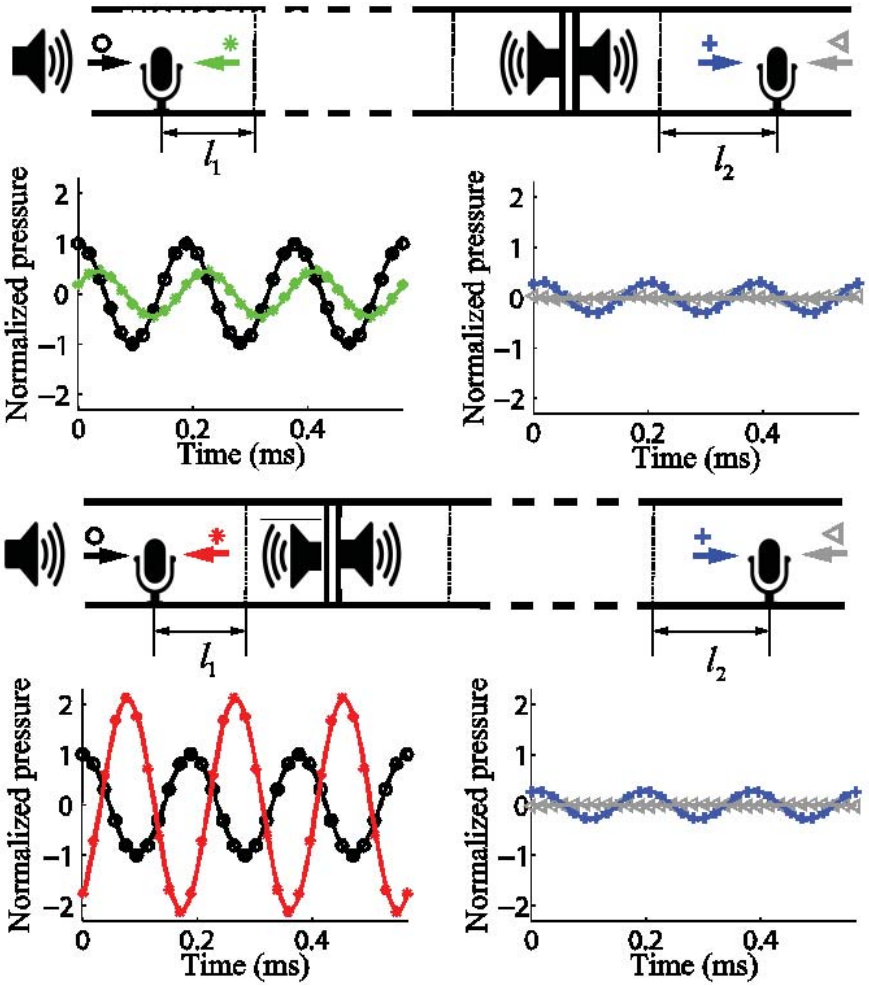


Figure 5.7: *Transmission and reflections from the loss and gain sides of a PT symmetric system consisting of loss and gain units without gap in between. The calculated values are represented by curves and the measured values are represented by marked dots, respectively. Black color shows the incidence, green color shows the reflection from the loss side, red color shows the reflection from the gain side, blue color shows the transmission, and grey color shows the wave reflected from the end of the waveguide, respectively. All waves are normalized by their inputs. The system has small transmission. Reflections can be observed on both sides.*

5.10 Difference between Exceptional Points and Accidental Degenerate Points

Conventionally, two equivalent definitions exist for PT "exact" and "broken" phases. A PT symmetric system is in PT "exact phase" when the eigenvalues of the system scattering

matrix are unimodular as shown in Figure 5.8. Once the norms of these eigenvalues are non-unity, the system is in the PT "broken phase". As depicted by Figure 5.8, this definition of the PT phases is equivalent to the one we gave in the main text.

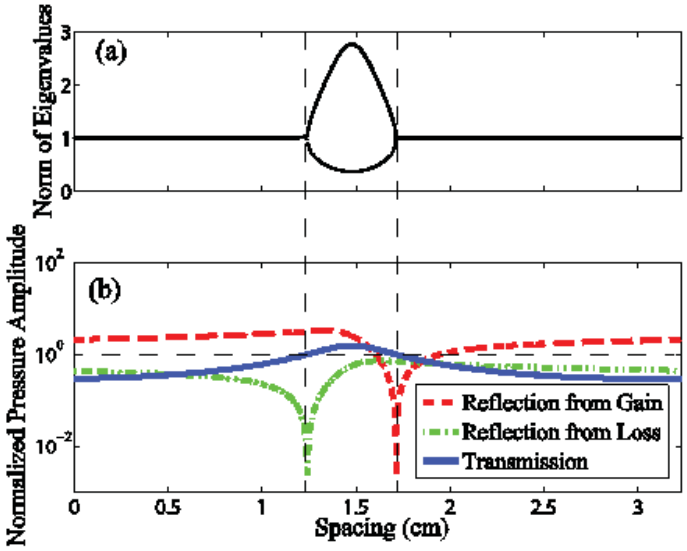


Figure 5.8: *Equivalence of two definitions of PT phases. (a) The norm of the eigenvalues of the system scattering matrix varying with spacing between the loss and gain materials. (b) The transmission (blue) and reflections from the gain side (orange) and the loss side (red) varying with spacing between the loss and gain materials from zero to half wavelength at 5.3 kHz. Two exceptional points are observed when the spacing is 1.24 cm and 1.71 cm.*

As defined previously, exceptional points of PT symmetric systems associate with the phase transition of the system where total transmission is observed. According to Eq. (5.1), one of the reflections must vanish at the exceptional points. Total transmission can also be obtained for accidental degenerate points where the two reflections are simultaneously zero, satisfying Eq. (5.1). The exceptional points and accidental degenerate points look similar, but they are fundamentally different. Figure 5.9 shows the transmissions and reflections for two PT symmetric systems. Two exceptional points associated with the phase transitions from the PT "exact phase" to PT "broken phase", and back to PT "exact phase" are observed in Figure 5.9. By tuning the system parameters, one can shift these two exceptional points and make them to be accidentally degenerate at a frequency, resulting in an accidental degenerate point shown in Figure 5.9. However, the PT "broken phase" does not exist when this accidental degenerate point appears. Thus, the phase transition does not occur at accident degenerate points, making them different from the exceptional points.

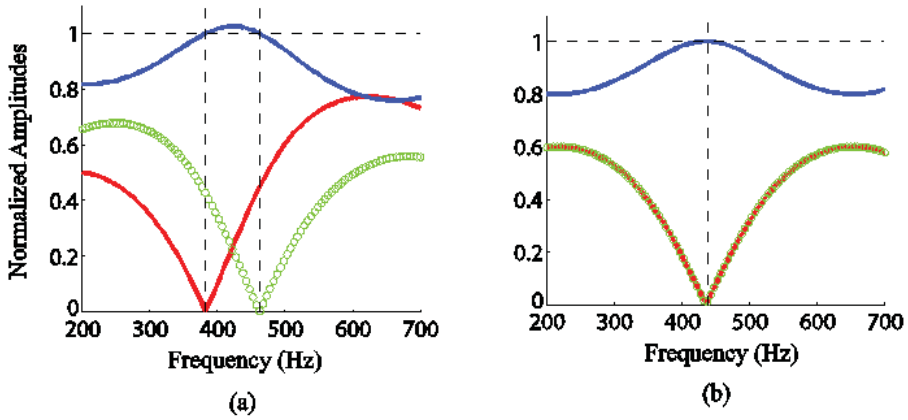


Figure 5.9: *Difference between exceptional points and accidental degenerate points. Transmissions (blue curves) and reflections from the gain side (red curves) and from the loss side (green circles) of systems where (a) two exceptional points are observed and (b) one accidental degenerate point is observed. All amplitudes are normalized by their inputs.*

5.11 Response of Broadband Pulse Signal

A pulse signal with central frequency at 5.5 kHz and bandwidth 1 kHz is used to study the response of broadband signal in the PT symmetric structure under our control of the exceptional points. The calculated transmission, reflections from the loss and gain sides are shown in Figure 5.10. The reflection from the loss side is zero, while the reflection from the gain side is observed. Because the phases of transmission at different frequencies are different, the transmission is slightly distorted, but the transmitted energy remains 100%. This analytical result reveals that our control of the exceptional points is working for broadband signals.

5.12 Exceptional Points of PT Symmetric Periodic Structures

Even though only one PT symmetric unit is used in our demonstration, the method we used to control exceptional points can be used for PT symmetric periodic structures described in [66]. Figure 5.11 shows the comparison of transmission and reflection loci of PT symmetric systems consisting of one unit and a thousand units. Effective loss and gain media with mass density 1.4 kg/m3 and refractive indices $1.4 \pm 0.1j$ are used in the simulations. Each of the loss or gain unit is 10 cm with no spacing between them. Two exceptional points are observed at 482 Hz and 716 Hz in both cases, indicating that the exceptional points of systems with single and periodic PT symmetric units are identical. This numerical result indicates that our control method valid for one PT symmetric unit can also be used to

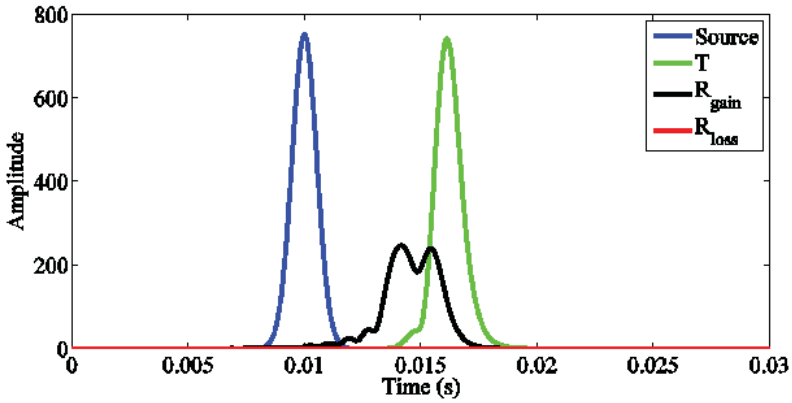


Figure 5.10: *Transmission and reflections from the gain and loss sides of a pulse incidence with central frequency at 5.5 kHz and bandwidth 2 kHz. The pulse incidence, transmission, and reflections from the gain and loss sides are shown by blue, green, black, and red curves, respectively. The reflection from the loss side vanishes while the reflection from the gain side is obtained. Because the transmission phases at different frequencies are different, the transmitted pulse is slightly distorted, but the transmitted energy remains* 100%.

control the exceptional points of systems with periodic PT symmetric units regardless of the number of unit cells.

5.13 Control of Exceptional Points in Systems Formed by Multiple Non-Hermitian Materials without PT Symmetry

Our control method of exceptional points can also handle systems containing multiple non-Hermitian materials without PT symmetry discussed in [62] for the observation of unidirectional reflection. Figure 5.12 shows the contrast of reflections from the two sides of the system containing two 10 cm effective loss materials with mass densities 1.4 kg/m^3 and 1 kg/m^3 and refractive indices $1.4 - 0.1j$ and $1.2 - 0.05j$, where the contrast is defined as

$$\text{Contrast} = \frac{||r_l| - |r_r||}{|r_l| + |r_r|}. \tag{5.8}$$

This contrast is a function of frequency and the spacing between the two loss materials. Several curves with high contrast are observed in Figure 5.12. One can tune the spacing according to the incident frequency following these curves to control the exceptional points and realize unidirectional reflection with high contrast.

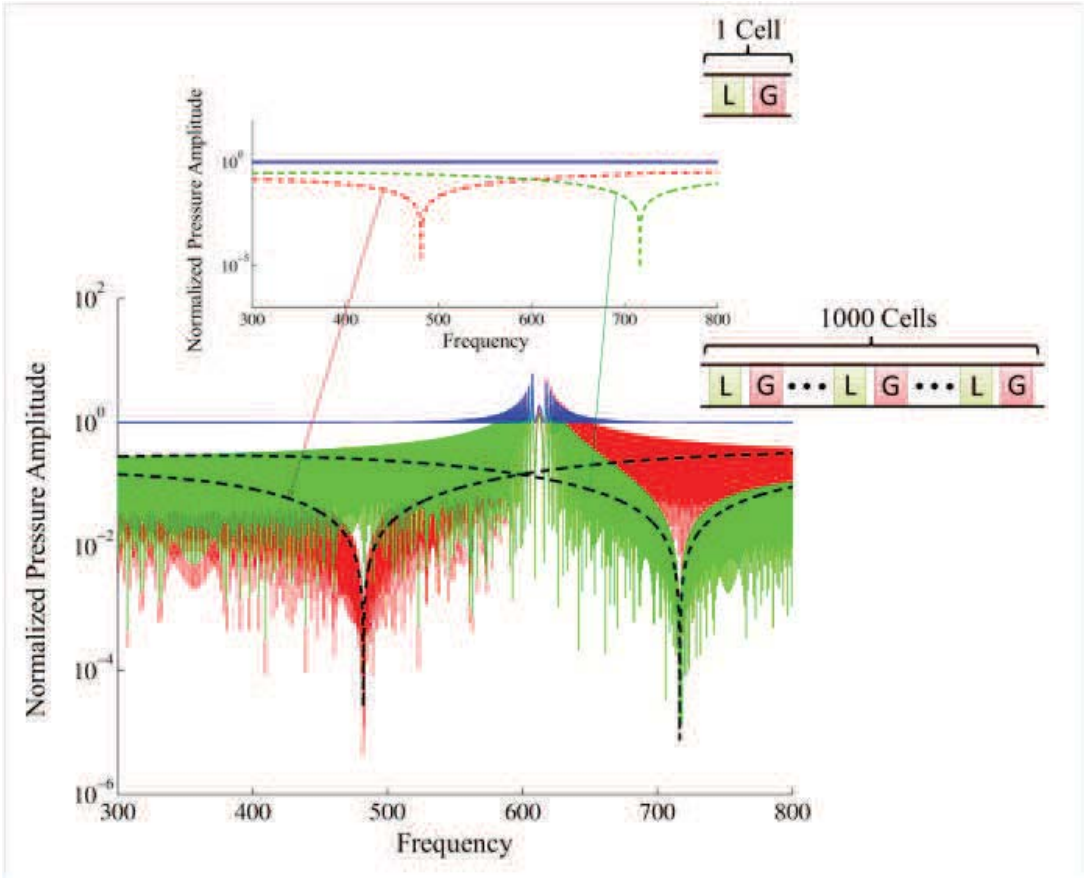


Figure 5.11: *Transmissions (blue) and reflections from loss side (green) and gain side (red) of systems with one and a thousand PT symmetric units. Effective loss and gain materials with mass density 1.4 kg/m^3 and refractive indices* $1.4 \pm 0.1j$ *are used. In both cases, two exceptional points are observed. The exceptional points of these two systems appear at the same frequencies.*

5.14 Discussion on Previous Demonstration of PT Symmetric Acoustics

A recent report discussed the possibility of using electronic circuits with specific impedances to realize a PT symmetric acoustic unit [88]. However, only one exceptional point was observed, and no method for the control of this exceptional point was proposed. This realization of PT symmetric system relies on electronic signals that has been demonstrated previously [63], rather than acoustic waves. Even with an active gain unit, the validation of the PT symmetric condition in our system depends on the acoustic waves propagating through the loss and gain units. Both loss and gain units need to be judiciously designed

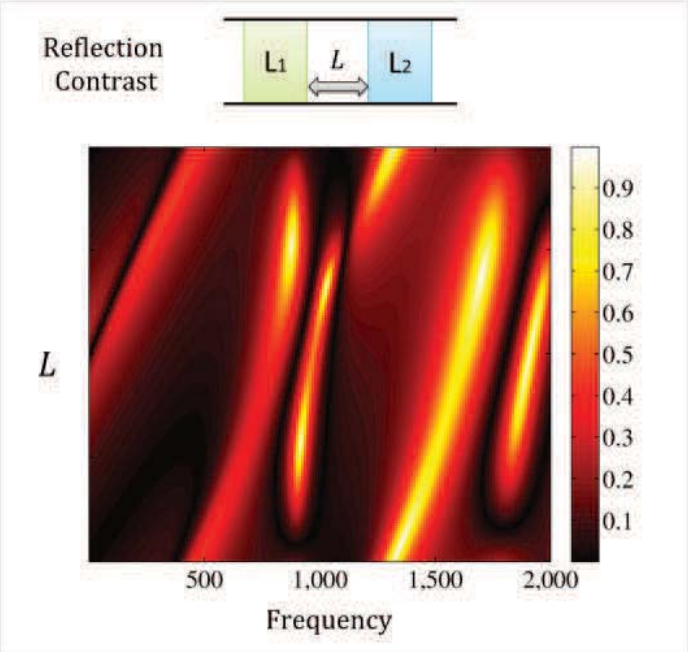


Figure 5.12: *Contrast between the two reflections as a function of frequency and spacing in a system with two loss materials. Each of the loss materials is 10 cm with mass densities 1.4 kg/m^3 and 1 kg/m^3 and refractive indices* $1.4 - 0.1j$ *and* $1.2 - 0.05j$*, respectively. High contrast can be observed along several curves.*

in their proposal, preventing a wide application because most natural materials contain loss that is difficult to be controlled. Our design of PT symmetric acoustic systems overcomes this limitation because only the active gain unit is tuned to match with arbitrary loss materials.

5.15 Discussions

In conclusion, we propose and demonstrate a new method to control the exceptional points of PT symmetric systems by tuning the spacing between the loss and gain materials. This enables us to shift the exceptional points to desired frequencies and control the orientation of unidirectional transparency. Our control method can be applied to different fields such like electronics, optics, microwaves, etc. Numerically, this control method can also handle PT symmetric periodic structures [66] or non-Hermitian systems without PT symmetry [62] (see Sections 5.12 and 5.13). Thanks to the active acoustic gain medium, this control can be realized over a large frequency band. Unidirectional transparency for pulsed signals can be perceived if the transmitted phases and the non-vanishing reflections are adjusted to be identical at different frequencies using additional degrees of freedom such as number of unit cells, lengths of loss and gain units, etc. This control ability over the exceptional points in

PT symmetric system opens a new avenue for developing asymmetric wave transport devices, important for directional imaging and sensing, logic acoustics, and other applications.

5.16 Methods

In this article, the acoustic refractive index is defined as $n = 343/c$, where c is the complex-valued sound speed in the medium. We use a 0.148 m long leaky waveguide consists of nine slits with filling ratio 0.19 on the wall of the waveguide to form our loss part as shown in Figure 2a. These slits leak the acoustic energy out of the waveguide. The height of the waveguide we use is 0.024 m. Both simulations and experiments confirm this loss material is dispersive. An active unit containing two arrays of Kobnite 254-PS600-RO speakers facing opposite directions is used to reproduce an artificial acoustic gain material because there is no passive acoustic gain material exists in nature. Each speaker array possesses fifteen speakers with spacing 0.03 m in between the centers of each speaker. The 0.03 m spacing is chosen because it is about the half of the wavelength of acoustic wave at 6 kHz, the highest frequency we used in our experiment, and hence generate plane wave in the waveguide. The two speaker arrays are used to control the transmission and reflection of the artificial gain material to generate the scattering matrix an acoustic gain material using a linear operation described in Section 5.7. A third speaker array is used to generate the incident plane wave in our experiment. These three speaker arrays are controlled by a LabVIEW program through NI-USB 6259 DAQ system. Two pairs of PUI Audio PUM-5250L-R microphones are assembled on each side of the media to measure the scattering matrix (i.e. transmission and reflection coefficients). Each pair of microphones contains two microphones facing opposite directions. The measured signals are amplified and filtered using home-made amplification and filtering circuits. A calibration operation (see Section 5.8) is applied to the two microphone pairs so that they can detect the left and right going waves simultaneously.

Chapter 6

Acoustic Metasurfaces

6.1 Introduction

Absorbers and diffusers are essential elements to control echoes in architectural acoustics. In several applications, acoustic diffusers are preferred because absorbers remove sound energy from the environment, whereas they redistribute the acoustic energy in order to avoid strong dispersion and reverberating paths [98, 99]. Traditional diffusers are heavy, bulky wavelength scale structures with complex geometries, therefore difficult to integrate in existing environments. Recently developed metasurfaces provide the ability to control waves with a single layer of deep-subwavelength elements. Owing to their ultra-thin dimension, metasurface elements can be conformally attached to an arbitrary shape to virtually reproduce the acoustic response of another geometry. In optics, metasurfaces give the freedom of modulating the phase of light to realize beam steering [100–102], ultrathin optical skin cloak [103], smaller optical devices for advanced digital products [104, 105], and holograms [106–108]. Subwavelength metasurface concept is especially important for acoustic wave manipulations as the wavelength is much larger than optics and the size constraint is critical. Coiled space elements were developed as building blocks of acoustic metasurface to modulate sound phase by increasing the effective path length and have been used for beam steering [19, 20, 37–39, 109–113]. However, the thickness of coiled space based metasurfaces is difficult to shrink down less than quarter wavelength because a large intrinsic loss will result from viscosity in the extreme narrow channels [48]. Another type of acoustic metasurfaces is formed by membranes decorated with masses, which were used to realize simultaneous negative density and bulk modulus [114] and an acoustic perfect absorber [21]. Thin acoustic cloak was also proposed theoretically using membrane type metasurfaces [115, 116], and was demonstrated by Helmholtz resonators with varying cavity volumes [22]. Up to date, the design of metasurfaces is typically assuming a continuous phase profile.

Here, we introduce an acoustic metasurface with 1/12 wavelength thickness to realize acoustic carpet cloak for a randomly rapid-change surface and a virtual acoustic diffuser from a flat surface using a set of Helmholtz resonators. The limitation of metasurface for

large phase gradient application is explored based on a nonlocal model that considers the contributions from neighboring surface profiles. This study extends the integration of smart acoustic surface and may find applications of surface engineering such as in architectural acoustics.

6.2 Design of Acoustic Metasurfaces

In this paper, we extend the previous design of metasurface carpet cloak to investigate the effect of large in-plane (rapid-changing) phase gradient on the cloaking performance. In first order approximation, the carpet cloaking requires each metasurface element to provide a phase shift $\Delta\phi(x) = -2kh(x)\cos\theta$, where k is the wave number, $h(x)$ is the height profile of the structure to be cloaked (Figure 6.1), and θ is the incident angle [22, 103, 115, 116]. This phase shift compensates the path difference due to the geometry of the object. Consequently, the reflected wavefront from the structure decorated with metasurface is flat, and the object becomes invisible for acoustic wave, as shown in Figure 6.1. On the other hand, metasurface elements can be used to make a flat surface to be a virtual diffuser for acoustic wave. In Figure 6.1, we apply a metasurface with the exact opposite phase modulation $\Delta\phi'(x) = 2kh(x)\cos\theta$ to recreate the scattering pattern of the object observed in Figure 6.1 from a flat surface. As sketched in Figure 6.1, previous studies in optics and acoustics demonstrated the ability to cloak structures with small continuous in-plane phase variation [22, 103, 115, 116]. On the other hand, Figure 6.1 presents a structure where the pillars heights are chosen randomly and vary dramatically from site to site. During this random process, sharp well-like structures are created among the pillars, as detailed in Figure 6.1. These wells have very narrow width leading to impedance mismatch that did not exist in the smooth gradient structure. We are able to analytically derive the reflection coefficient R obtained from the well structure sketched in Figure 6.1

$$\frac{R}{I} = \frac{m - 1 + e^{-j2kL}(m+1)}{m + 1 + e^{-j2kL}(m-1)}, \tag{6.1}$$

with $m = S_1/S_2$, and $T = T'e^{(-2ikL)}$. From this expression we can show that the amplitude of this reflection coefficient R is always unity as no energy is stored in the well. However, Figure 6.1 presents the additional phase term $\Delta\phi = \arg(R/I) - 2kL$ acquired by the reflected field in the presence of the well for a ratio $m = 3$. It is clear that the impedance mismatch provides an additional phase term to the reflected wavefront. The goal of this work is to investigate if this additional scattering can be compensated (or reproduced) by the intuitive phase shift profile formula given earlier.

We use an ultrathin acoustic metasurface formed by Helmholtz resonators for surface scattering designs. These Helmholtz resonators are ultra small compared with the wavelength, forming a metasurface with 1/12 wavelength thickness (Figure 6.2). The phase of the reflected wave from the resonators is controlled by the neck diameter (Figure 6.2). Finite element method simulations, including air viscosity model and thermoviscous boundary layer effects [48] (See Section 6.5), show that the reflection phase can be tuned over the entire

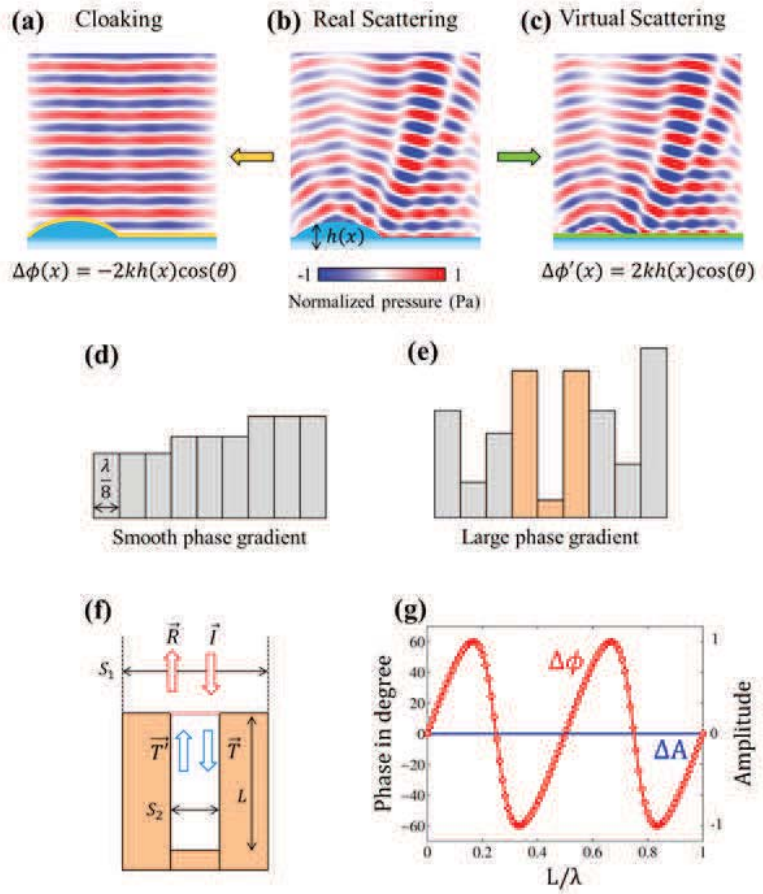


Figure 6.1: *Acoustic surface engineering for reflected waves. (a) The actual reflected field of a simple bump. The scattering pattern allows acoustic wave to detect the existence of the bump. (b) Acoustic cloaking of a bump with metasurface. The metasurface modulates the phase to flatten the reflected wavefront. Thus, the bump is invisible through acoustic wave. (c) Acoustic diffuser formed by metasurface on a flat surface. With the inverse phase mask of the cloak in (b), the scattering pattern in (a) is created. Therefore, the flat surface with decorated metasurface mimics the bump structure, resulting in a virtual acoustic diffuser. (d), (e) Sketch of structure inducing, respectively, small and large in plane phase gradient. (f) Detailed view of the well structure formed in (e) because of the height variation. (g) Calculated additional phase and amplitude in the reflection R from the well structure for a ratio* $m = S_1/S_2 = 3$ *as a function of the well depth L normalized by the incident wavelength.*

phase range, enabling the complete modulation of reflected wavefront. In our experiment, we select six Helmholtz resonators with increasing neck diameters, resulting in six different reflection phases at 2.9 kHz: 60, 120, 180, 240, 300, and 360 degrees. The measured resonances of the 3D printed resonators deviate slightly from the designed frequencies as a

result of fabrication error (Figure 6.2). However, this disagreement only leads to a deviation within 20 degrees from the designed value in reflection phase which is reasonable for our experimental setup. 20% of the incident amplitude is absorbed due to the material loss of the resonator units. Four cylindrical slots are printed on the back of each resonator such that they fit on LEGO bricks. This mechanism enables straightforward reconfigurations of metasurfaces formed by the Helmholtz resonators on structured surfaces built from standard LEGO bricks.

6.3 Carpet Cloaking

The metasurface has been applied to a simple bump structure. Recent study on acoustic metasurface demonstrated a thin carpet cloak by modulating reflection phase with a thicker design of Helmholtz resonators [22]. Our design only changes the neck diameter, allowing the realization of deep subwavelength elements ($\lambda/7.5 \times \lambda/7.5 \times \lambda/12$). Moreover, the possibility of developing an ultrathin carpet cloak for a complex random structure as shown in Figure 6.3 remains as an open question in both acoustics and electromagnetics. As discussed above, the abrupt changes of height in the structure induce not only a large phase gradient but also variations of the acoustic impedance, resulting in additional phase term in the reflected field. In our experiment, we randomly choose the height of each column between zero and one wavelength. The width of these columns is 1/7.5 wavelength, allowing us to create a diffuser with large phase gradient (Figure 6.3). The measured scattering of normal incident plane wave reflected from the complex random structure at 2.9 kHz is shown in Figure 6.3. With metasurface formed by our Helmholtz resonators providing a local phase shift $\Delta\phi(x) = -2kh(x)$ (for small incident angle) canceling the reflection phase variation solely due to the height change of the structure, the scattering is eliminated and a planar wavefront is observed in the reflection (Figure 6.3). This scattering cancellation can be accomplished between 2.8 kHz and 3 kHz with the 3D printed Helmholtz resonators (see Section 6.6). Therefore, this metasurface design has the ability to cancel simultaneously the scattering from the surface roughness and impedance mismatch. As shown in Figure 6.1, the phase shift between T and T comes from the distance $2L$ travel by the acoustic field. In the case of the decorated structure, one Helmholtz resonator is placed at the bottom of the well, this resonator is specifically chosen to add a phase term $\Delta\phi = -2kL$ to the field T. Therefore, we obtain $T = T'e^{(-2jkL - j\Delta\phi)}$ and we can insert this in Eq. (6.1)

$$\frac{R}{I} = \frac{m - 1 + e^{-j2kL - j\Delta\phi}(m + 1)}{m + 1 + e^{-j2kL - j\Delta\phi}(m - 1)}. \tag{6.2}$$

As $\Delta\phi = -2kL$, Eq. (6.2) is simplified as $R = I$ which is what we would expect if the wave was reflected by a flat hard wall. This analysis and the experimental result demonstrate that metasurfaces with phase shift only depending on the local elevation can be used to cloak complex random structures with large in-plane phase gradient. As of the incident angle dependence, numerical simulations show that our metasurface works until ± 20 degrees. This

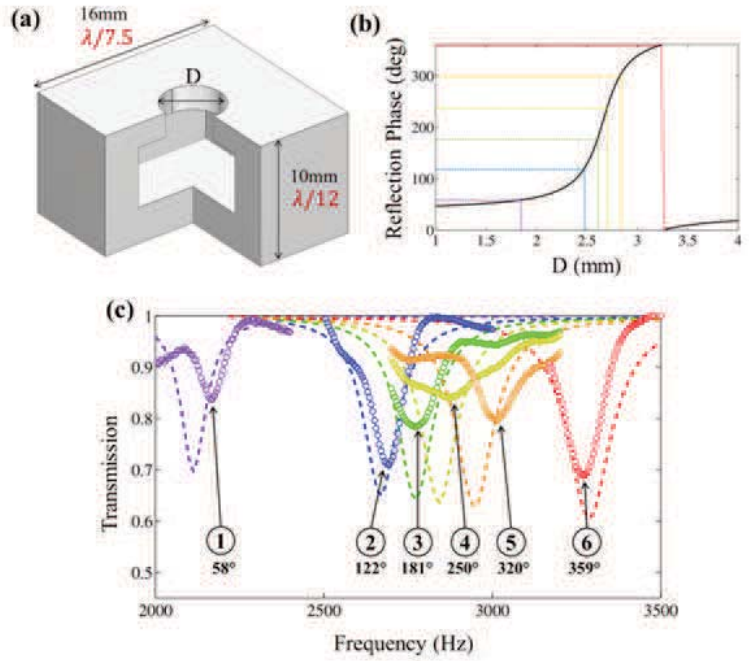


Figure 6.2: *Unit cells of metasurface used for acoustic surface engineering. (a) A unit cell formed by a Helmholtz resonator. The unit cell has dimensions 16 mm × 16 mm × 10 mm with a 10 mm × 10 mm × 5 mm cavity and a cylindrical neck, whose diameter is D and height is 2 mm. (b) Numerically calculated relation between reflection phase and neck diameter at 2.9 kHz with COMSOL. By varying the neck diameter, the resonance of the Helmholtz resonator is shifted. For the same working frequency, this shift of resonance results in a different reflection phase. Six different neck diameters are chosen to realize 60, 120, 180, 240, 300, and 360 degrees reflection phase shifts as marked by the dotted lines. (c) Measured (dotted lines) and numerically calculated (dashed lines) resonances of the six selected Helmholtz resonators. Viscosity loss and thermoviscous boundary layers are considered in the COMSOL simulations (see Section 6.5). The resonances are characterized by the dips of the transmission in an acoustic tube waveguide with a corresponding Helmholtz resonator assembled on the side wall of the waveguide. The resonant frequencies of the six resonators shift from the designed values as a result of fabrication errors. The resulted reflection phase modulations are 4% within the desired values.*

is expected from the local phase shift equation $\Delta\phi(x) = -2kh(x)\cos\theta$ which is a second order function for small θ [22] (See Section 6.7).

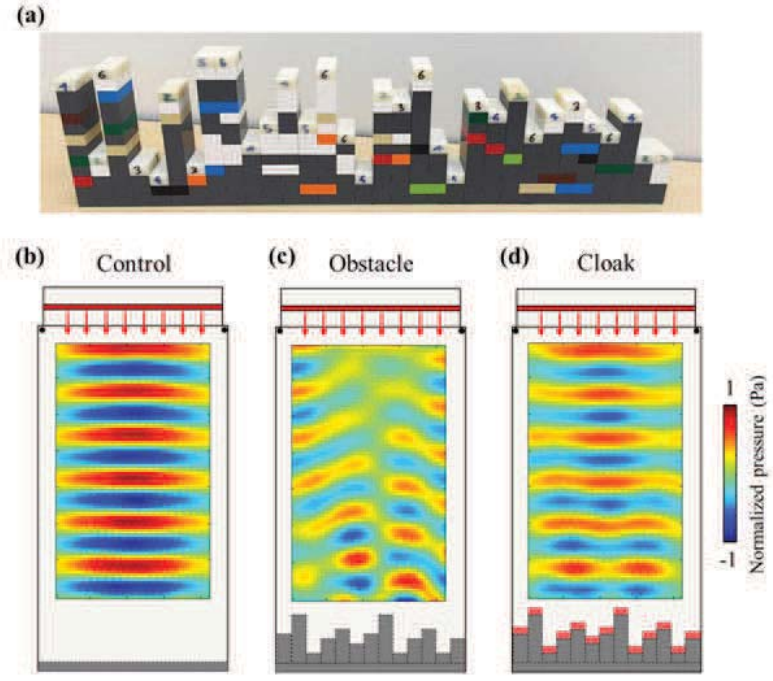


Figure 6.3: *Acoustic cloaking with metasurface. (a) Actual structure used in experiments. The complex random structure is constructed from LEGO bricks. This complex random structure is decorated by 3D printed Helmholtz resonators forming an ultrathin metasurface for acoustic surface engineering. (b) Measured reflection field of normal incidence from a flat reflection surface at 2.9 kHz. A flat wavefront is observed. This scan serves as the control experiment for the comparison with cloaking experiment. (c) Measured reflection field of normal incidence from a complex random structure at 2.9 kHz. The reflection field presents multi-scattering pattern as a result of the height variation of the reflection surface and impedance mismatch due to the variation of cross-section area. (d) Measured reflection field of normal incidence from the complex random structure decorated with cloaking metasurface at 2.9 kHz. The cloaking metasurface modulates the reflective surface by manipulating the reflection phase such that the height of each column is reduced virtually to the based surface (flat surface in (a)). Thus, the acoustic wave detects a flat surface and reflected with flat wavefront. Consequently, the complex random structure is cloaked by the metasurface.*

6.4 Virtual Diffuser

A flat surface can also be transformed into a diffusive surface for acoustic waves using metasurfaces with appropriate combinations of the unit cells. This transformation of mirror surfaces into diffusive surfaces is the inverse problem of cloaking. One can anticipate it should be achieved by metasurfaces (for small incident angle) with the opposite local phase

shift $\Delta\phi'(x) = 2kh'(x)$, where h is the local height of the virtual object. In our experiment, we reproduce the scattering pattern of a circular bump (Figure 6.4) from a flat metasurface at 2.9 kHz. By applying the calculated phase shift, a virtual acoustic object is created and the same cylindrical wavefront is obtained in the reflection (Figure 6.4). Therefore, the flat surface is transformed into a diffusive surface by our metasurface.

It is interesting to ask if we can transform the flat surface into the complex random surface shown in Figure 6.3. By applying the same strategy, a diffusive phase mask is applied on a flat surface. Surprisingly, the measured reflection shown in Figure 6.4d is different from that in Figure 6.4c for the complex random structure. Although the metasurface shifts the reflection phase to mimic the height variation, the abrupt changes of impedance described previously are not captured in this simple relation. We can use the well structure (Figure 6.5) as a model to demonstrate this limitation. In order to reproduce the reflection R observed in Figure 6.5, we need to determine the amplitude (A) and phase (ϕ) that our element has to reflect in Figure 6.5. Assuming that each side of the well reflects perfectly the incident wave, we obtain the following relation

$$Ae^{j\phi} = m(\frac{R}{I} - 1) + 1, \tag{6.3}$$

with $m = S_1/S_2$. The amplitude and phase of this field are represented in Figure 6.5 as a function of the well depth L in the case $m = 3$. First, we can see that the phase is no longer a linear function of the well depth. Second, and more importantly, the amplitude A is larger than unity and needs to be modulated as a function of L. We have numerically checked the validity of Eq. (6.3) in Figure 6.5. Three elements highlighted in green are used to reproduce the field reflected by the triple well structure shown in Figure 6.5. The amplitude and phase of the field emitted by these elements are chosen respectively to the well depth (Figure 6.5). However, the experimental demonstration of this result is hindered by the fact that our metasurface cannot modulate the reflected amplitude. The Helmholtz resonators are used as phase elements, whose amplitude response are constant and cannot exceed unity. This result explained why the linear relation between phase and height of the structure fails when the height varies at a deep subwavelength scale. Recent works have proposed an alternative approach based on holography, to control the acoustic field propagation [117, 118]. However, the phase retrieval technique used to obtain the phase mask is only achieved with conditioned numerical iterations.

6.5 Influence of Air Viscosity and Thermoviscous Boundary Layer

In this section we investigate the influence of viscosity on the performances of our metasurface. Figure 6.6 presents the amplitude and phase of the reflected field from our Helmholtz resonator with varying radius, excited at 2.9 kHz, with and without viscous loss. Standard viscous loss is taken from [119]. First, it is worth noting from Figure 6.6 that the reflected

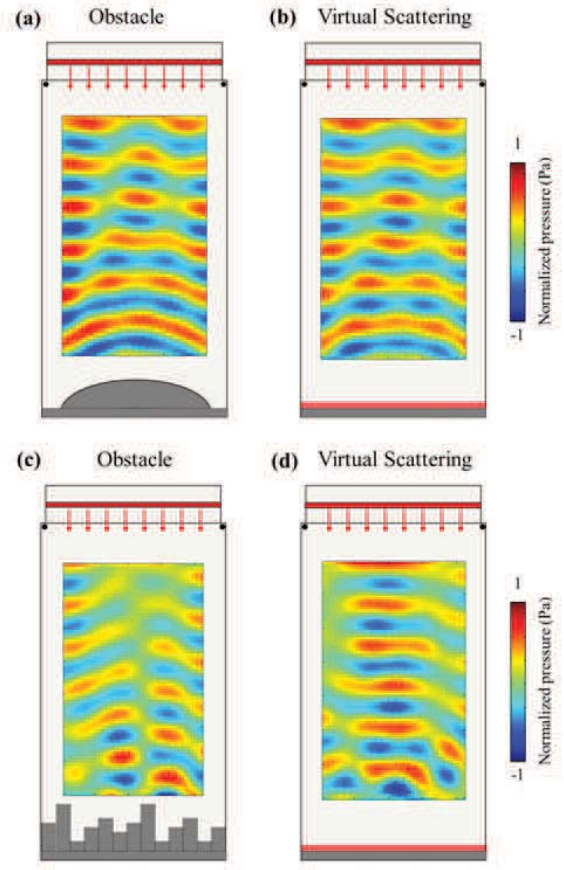


Figure 6.4: *Acoustic diffuser created by metasurface. (a) Measured reflection field of normal incidence from a circular bump at 2.9 kHz. The circular bump results in wave scattering that diffuses the incident acoustic wave in all directions. (b) Measured reflection field of normal incidence from a flat reflection surface decorated with diffusive metasurface. The metasurface modulate the reflection phase such that the local reflection surface presents a virtual height variation identical to the circular bump in (a). This virtual height variation results in the same scattering pattern that diffuses the acoustic wave in all directions. Thus, the metasurface creates an acoustic diffuser from a flat reflection surface. (c) Measured reflection field of normal incidence from a complex random structure as shown in Figure 6.3b. The multi-scattering pattern is a result of the combination of the reflections due to the rough surface and impedance mismatch. (d) Measured reflection field of normal incidence from a flat reflective surface decorated with the inverse phase mask used for cloaking in Figure 6.3c. The scattering pattern is different from the complex random structure. Thus, the inverse phase mask cannot recreate the scattering of the complex random structure.*

phase is identical whether loss is taken into account or not. Second, losses are more pronounced for Helmholtz resonators which are resonant with the excitation frequency. However,

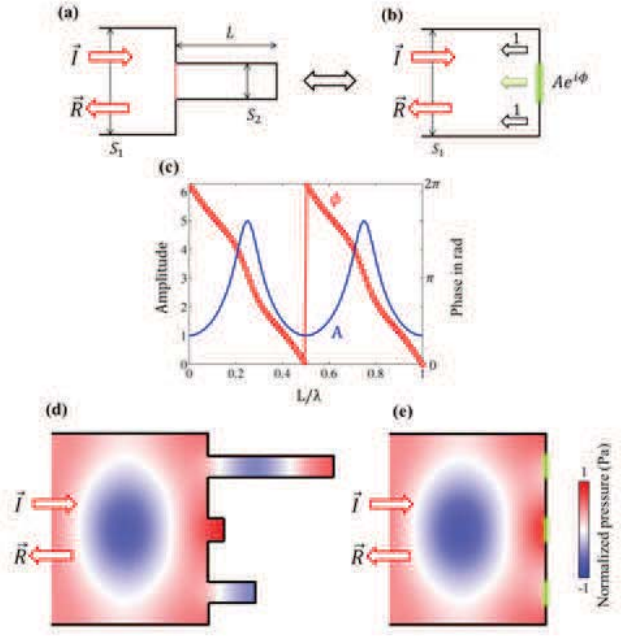


Figure 6.5: *Inverse phase mask for large in plane phase gradient. (a) Sketch of the well like structure emerging from the large in plane phase gradient objects. (b) Sketch of the virtual diffuser configuration. The amplitude and phase of the purple element are chosen such that the new structure presents the same reflection R as in (a). (c) Analytically calculated amplitude A and phase ϕ obtained from (Eq.* (6.3)*) with $m = 3$ as a function of the well depth L normalized by the incident wavelength. (d) Numerical simulation of the field reflected by a triple well structure at 2.9 kHz with the experimental dimensions (width of* 7.5λ*). (e) Reproduction of the reflected field with three active elements highlighted in green. Amplitude and phase are taken from (c) respectively to the well depth.*

the amplitude reduction between the different resonators is less than 6%. We will see in the following that such an amplitude difference has a very small impact on the final metasurface results..We performed simulations to compare the cloaking performances in presence of loss. Figure 6.7 presents simulation results from the rapidly changing profile at 2.9 kHz. As expected from the small loss observed in Figure 6.6, the cloaking performances are almost identical with viscosity taken into account. These numerical results confirm that viscous loss plays a minor role in the performance of our metasurface.

Recent work has drawn attention to detrimental thermoviscous effects in subwavelength acoustic ducts [48]. In this section, we performed simulations that include thermoviscous effects such as the boundary layers. Figure 6.8 shows the resonance frequency of each resonator obtained with the thermoviscous model (dashed lines). As anticipated, the deviation from the atmospheric loss case (solid lines) is maximal for the smallest diameter (black curves) and represents 3% of the central frequency. This is in agreement with the value reported

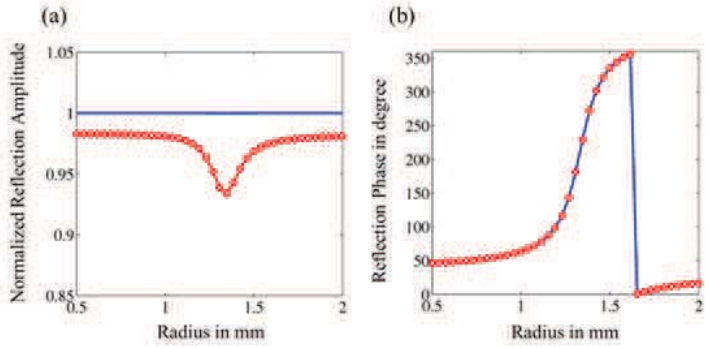


Figure 6.6: *Amplitude (a) and phase (b) of the reflected field from Helmholtz resonator with varying radius excited at 2.9 kHz. Blue solid line shows results from simulations without viscous loss. Red open circle shows corresponding simulations while taking loss into account.*

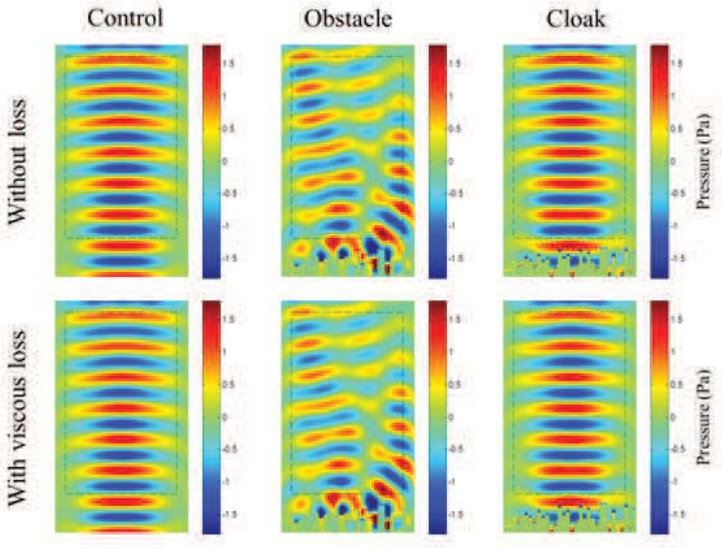


Figure 6.7: *Reflected field with (bottom line) and without (top line) viscous loss. Plane wave excitation at 2.9 kHz and colorbars are identical for each reflected field represented. The dashed rectangle depicts the field of view used in the experimental results presented in the manuscript.*

in [48]. We have shown in a previous reply that the bulk loss do not affect the resonance frequency. Therefore, we will use a lossless model to compare with the thermoviscous one in the following.

Figure 6.9 presents the evolution of the reflected phase in function of the neck diameter when excited at 2900 Hz for both simulation models. As expected the largest deviation is

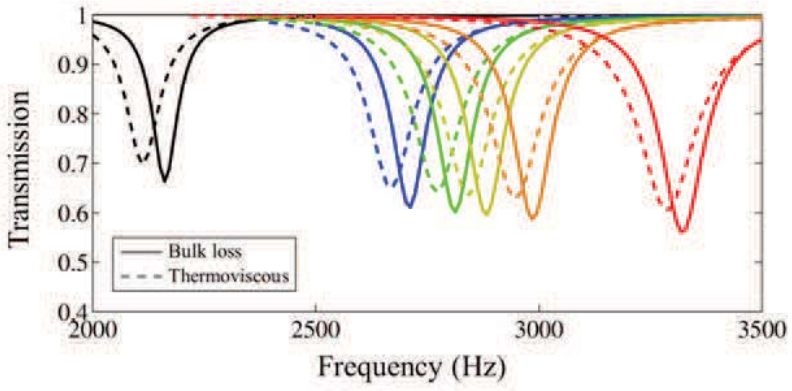


Figure 6.8: *Simulated resonant frequency of each resonator with thermoviscous model (dash) and bulk loss model (solid).*

on the order of 6% (20deg) for the resonator driven close to its resonance. We will see later that this deviation has a limited impact onto the cloaking performance.

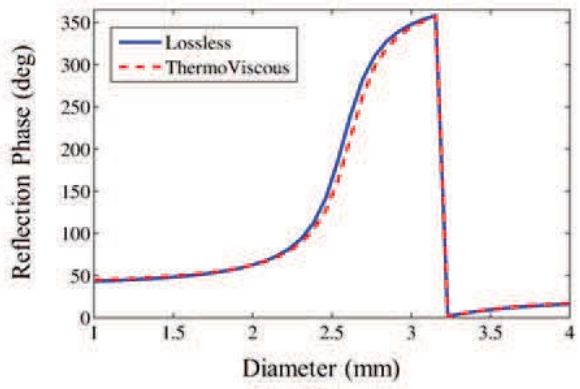


Figure 6.9: *Reflected phase in function of the neck diameter when excited at 2900 Hz with thermoviscous model (dash) and lossless model (solid).*

As mentioned previously, we perform a full size simulation (32 resonators) in order to investigate the impact of thermoviscous effects on the cloaking performance. Figure 6.10 represents the pressure field reflected from a rough surface decorated with the appropriate resonator in both lossless and thermoviscous models at 2900 Hz. If the thermoviscous model helps understanding the origin of losses observed in experiments, it is clear that the reflected wavefront is similar to the one observed in the lossless model and that the thermoviscous effects do not hinder our results.

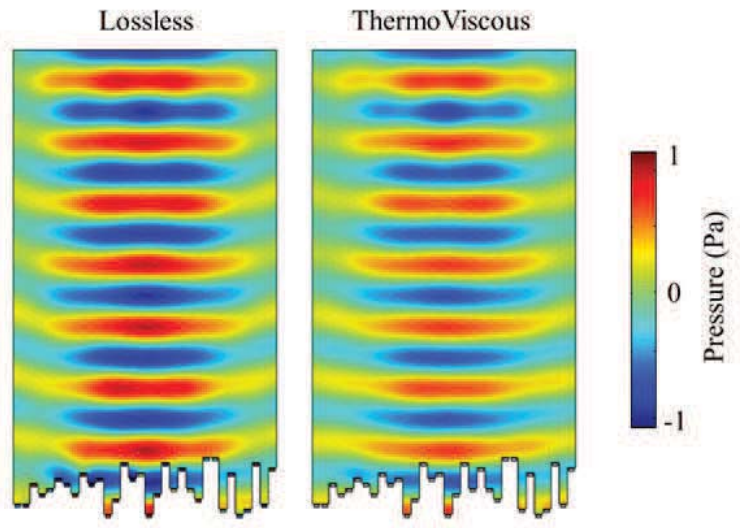


Figure 6.10: *Reflected field from the decorated profile at 2900 Hz with lossless (left) and thermoviscous (right).*

6.6 Experimentally Measured Bandwidth

As our metasurface is based on resonances, the resulting bandwidth is narrow. We performed experimental measurements for different frequencies to investigate the bandwidth of our metasurface when applied to rapidly changing profile. Figure 6.11 shows the reflected field for frequencies ranging from 2.6 kHz to 3.2 kHz. The scattering cancellation is good for the frequencies between 2.84 kHz and 3.04 kHz which gives us a bandwidth of 200 Hz or 7%.

6.7 Influence of Incident Angle

Our experimental setup does not allow us to investigate the incident angle dependence which requires a much larger scanning system. However, we present in the following figures the incident angle dependence for slowly and rapidly changing profile. As expected from the local phase shift equation $\Delta\phi(x) = -2kh(x)\cos\theta$, there is a second order dependence for small θ (see [22]). Therefore, the unit cell arrangement obtained for $\theta = 0^o$ should work for a certain range of angle. Figures 6.12 and 6.13 show numerical results obtained for cloaking of both slowly and rapidly changing profile at 2.9 kHz with varying incident angle. From both Figures 6.12 and 6.13, one can see that the cloaking performances hold very nicely up until 20 degrees of incidence independently from the profile gradient.

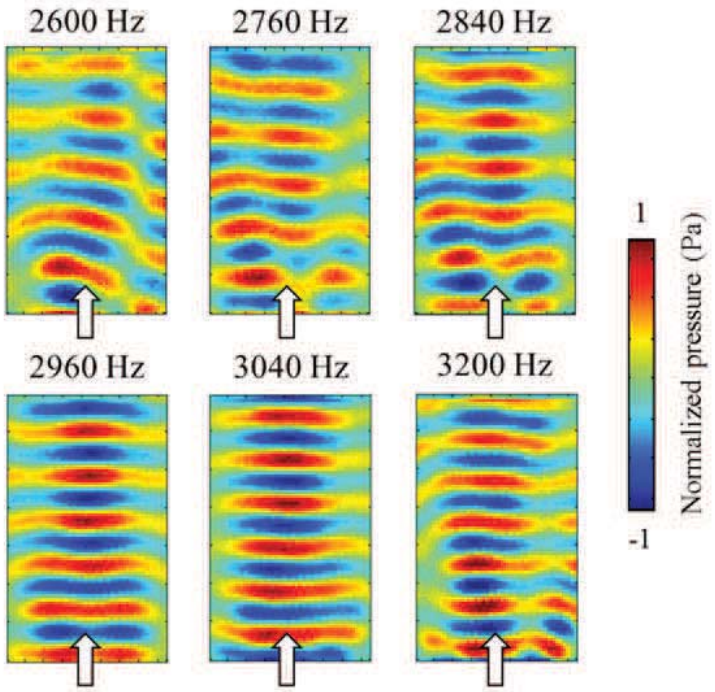


Figure 6.11: *Measured reflected field from the rapidly changing profile for different frequencies. The white arrows indicate the upward propagation direction of the reflected field.*

6.8 Discussions

In conclusion, an ultrathin metasurface formed by Helmholtz resonators with varying neck diameter is realized to modulate reflection phase. An ultrathin acoustic cloak for a complex random structure with abrupt height variation is realized. The inverse modulation of reflection phase with reconfigured metasurface transforms flat surfaces into diffusive structures with smooth phase gradient. The linear relation linking the phase and geometric profiles works for cloaking applications independently from the structure, but fails to recreate virtual diffusers with large in-plane phase gradient. This experimental and analytical study of ultrathin acoustic metasurface for large in plane phase gradient applications provides a deep understanding of reflective surface engineering, which is critical for smart and architectural acoustic designs.

6.9 Methods

The Helmholtz resonators are printed by SST 1200ES 3D printer from ABS plastics. These resonators have dimensions 16 mm $\times$ 16 mm $\times$ 10 mm with a 10 mm $\times$ 10 mm $\times$ 5 mm cavity. The necks of the resonators are drilled by milling machine with diameters 1.89 mm,

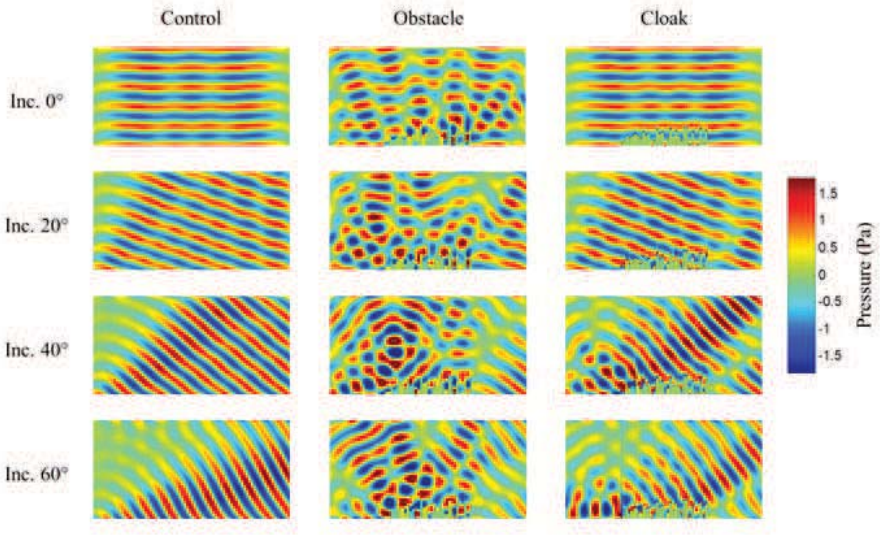


Figure 6.12: *Reflected field from the rapidly changing profile at 2.9 kHz with varying angle of incidence. Structures and colorbars are identical in every set of simulations.*

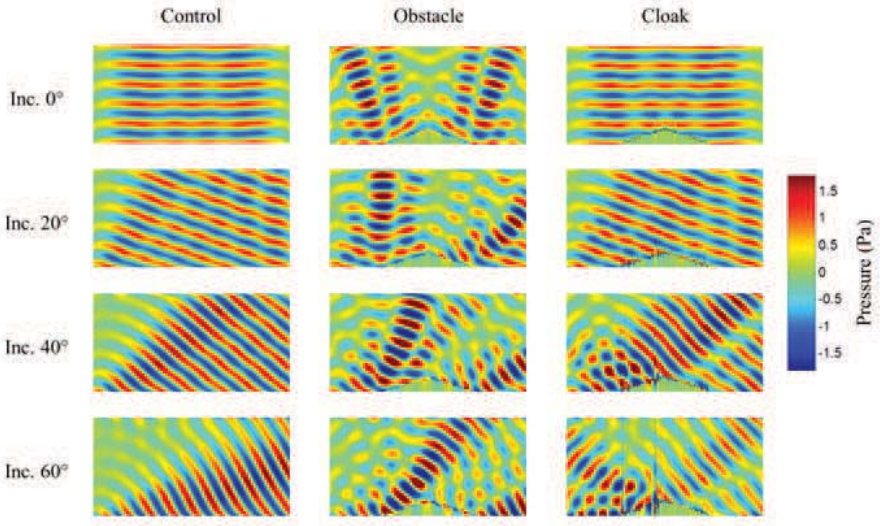


Figure 6.13: *Reflected field from the slowly changing profile at 2.9 kHz with varying angle of incidence. Structures and colorbars are identical in every set of simulations.*

2.47 mm, 2.61 mm, 2.70 mm, 2.83 mm, and 3.27 mm corresponding to the six different reflection phases. All scattering structures and reflective surfaces are constructed from 4 $\times$ 2 LEGO bricks and 2 $\times$ 2 LEGO flat tiles. The measurements are conducted in a two dimensional waveguide formed by two aluminum plates. The normal incident plane wave is

excited by a speaker array containing 15 Kobnite 254-PS600-RO speakers. The pressure field is measured by a CUI CME-1538-100LB microphone. The signal is amplified by a Reson VP2000 voltage preamplifier EC6081 and read by a Stanford Research Systems SR830 lock-in amplifier. Two VELMEX MN10-0150-E01 motors controlled by VXM stepping motor controller are used to move the microphone to scan an area of 70×42 points with step size 10.2 mm. The measurement of resonance frequency is conducted in a square aluminum tube with cross section 30 mm $\times$ 30 mm, and the corresponding resonator is assembled on a side wall of the tube.

Chapter 7

Orbital Angular Momentum Multiplexing

7.1 Introduction

With the increasing amount of human activities underwater including unmanned vehicle exploration, off-shore industrial applications, and remote ocean environment monitoring, the development of underwater communication has become essential. The intrinsic strong absorption of microwave and mid- and far-infrared radiations by water molecules limits the propagation distance of radio frequencies to mere centimeters [120–123], making RF wireless communication approaches impossible. On the other hand, optical waves are scattered by objects in the ocean such as small particles, debris and marine life due to the shorter wavelengths, limiting the range of optical communication underwater to be within just 200 meters [124–126]. Currently, acoustic waves are the only option for long range (over 200 meters) underwater communications. However the applicable bandwidth of acoustic waves is limited within 20 kHz because the higher damping loss of high frequency acoustic waves in water reduces the propagation distance to less than a kilometer range [127]. Such a low carrier frequency limits drastically the spectral bandwidth and data rate accessible for data transmission. Although spectral efficiency has been improved through recent advanced communication technologies such as differential phase shift keying (PSK) and quadrature amplitude modulation (QAM), the number of available data transmission channels remains tied to the low carrier frequency [128–132].

We propose to overcome such a fundamental limitation in acoustic communication by employing additional spatial degrees of freedom for data transmission, such as orbital angular momentum (OAM) of the information carrying wave whose wavefront has helical patterns (i.e. vortex beams). This spatial degree of freedom increases the data transmission capacity, which is given by the product of the available frequency bandwidth and number of modes employed for communication, at the same frequency band. In optics and microwaves, vortex or helical beams with different OAM topological charges are generated by spatial light modu-

lator (SLM), metasurfaces, or parity-time symmetric ring resonator and multiplexed through beam splitters or spin-orbital coupling to demonstrate a significant increase of data transmission capability [133–138]. For acoustics, the underwater propagation of vortex beams with single topological charge was demonstrated with active phase arrays [139, 140]. Passive acoustic phase modulation structures were proposed to generate single charge vortex beams [141–144]. These acoustic vortex beams were used to develop acoustic tweezers, and screwdrivers for particle trapping, levitation and manipulations [145–149]. However, information encoding through multiple OAM channels multiplexing/demultiplexing remains unexplored. Here, we demonstrate that the data transmission rate can be dramatically enhanced at a single frequency modulation by utilizing the spatial degree of freedom OAM of acoustic vortex beams. The proposed high throughput acoustic communications with OAM multiplexing is experimentally demonstrated in air here due to the facility limitations in underwater acoustics, but this technique can be readily extended to underwater applications because the wave physics in air and underwater are the same for low frequency acoustics below 20 kHz. In addition, previous studies have experimentally demonstrated the long distance propagation of phase information of underwater acoustic wave, crucial to underwater communications using OAM multiplexing [130, 139, 140]. It is worth to noting that the spatial multiplexing proposed can be added onto or combined with existing frequency encoding techniques (PSK, QAM, etc.). Thus, this new degree of freedom has the ability to further increase the existing highest acoustic underwater communication rate by N-fold with N the number of OAM channels used.

7.2 Significance

Acoustic communication is critical for underwater application such as deep ocean scientific explorations, off-shore industrial controls, and ocean environment monitoring. This is because other techniques using electromagnetic waves such as RF communications are difficult for underwater applications due to the strong absorption of water in such a frequency. Optical communication, on another hand, suffers from the light scattering from micro-particles or marine life making long range underwater optical communication very challenging. Therefore, using acoustic waves to transmit information is currently the dominate technique for underwater applications including data collection and remote control of off-shore benthic stations. However, the low frequency bandwidth available for acoustic communication limits the data transmission rate and information capacity or content. We propose and experimentally demonstrate here a new approach using the orbital angular momentum (OAM) of acoustic vortex beams which provides a new and independent channel that enhances the data transmission rate by eight fold. The OAM multiplexing method demonstrated here will impact significantly on future underwater communications.

7.3 Acoustic OAM

We use an active transducer array controlled by a digital processor to directly generate multiplexed acoustic vortex beams with eight OAM charges from -4 to +4 (Figure 7.1). Beam splitter or spin-orbital coupling was used for multiplexing different OAM topological charges in optics and microwaves [133–138]. However, acoustic beam splitter is still a challenging research topic [150] and the circular polarization of spin is fundamentally unavailable for sound waves. In our experiment, the multiplexing of different OAM charges is achieved by directly generating the interference pattern of the corresponding vortex beams, which requires independent modulations of amplitude and phase (Section 7.6). For each OAM topological charge l, the array as the sound source generates a relative phase difference varying from 0 to $2l\pi$ along azimuthal direction. The amplitudes and phases measured at a hundred wavelengths away from the emitting plane for vortex beams with OAM charges -4 to +4 at 16 kHz are shown in Figure 7.1. A low pass spatial filter is applied to remove the high frequency noise in the measured fields. The number of twists in the phase pattern indicates the magnitude of the OAM charge. The amplitude pattern of each vortex beam presents a ring shape with increasing radius as the magnitude of the topological charge becomes larger. We calculate the orthogonality relation between vortex beams with different OAM charges (Figure 7.1) by taking the inner product of the two corresponding pressure fields incorporating both amplitudes and phases (Section 7.6). The crosstalk of the measured vortex beams shown in Figure 7.1 is less than -8.54 dB. Therefore, these eight vortex beams provide orthogonal bases to increase the number of the physical channels for data transmission.

7.4 OAM Multiplexing

The multiplexing of the orthogonal OAM charges allows parallel information to be sent through a single acoustic beam. This multiplexing procedure is accomplished in the digital processor by forming linear combinations of the vortex signals used to generate the OAM bases in Figure 7.1. The resulted signals are sent to the active transducer array to emit the information-encoded multiplexed beam. Because the acoustic beam can be encoded with up to eight orthogonal OAM bases in our setup (Figure 7.1), a single acoustic beam conveys a byte (8 bits) of information. In our experiment, we use the multiplexed OAM beams to send the word “Berkly”, which is represented in ASCII binary protocol (Figure 7.2). Each OAM charge represents one bit of information in the one byte binary symbols of the letters. The OAM charges corresponding to “1” in the binary representations are called on-channels, and the other charges are off-channels. Because the multiplexed signals are emitted by the single transducer array, we set the total amplitude of each one-byte letter to be the same, i.e. the total amplitude is equally distributed amongst all of the on-channels for each letter. The inner product method used to characterize the crosstalk between the bases in Figure 7.1 provides an elegant method to decode the information from the superimposed multiplexed beams (Figure 7.2). We use the measured pressure fields (including amplitude and phase)

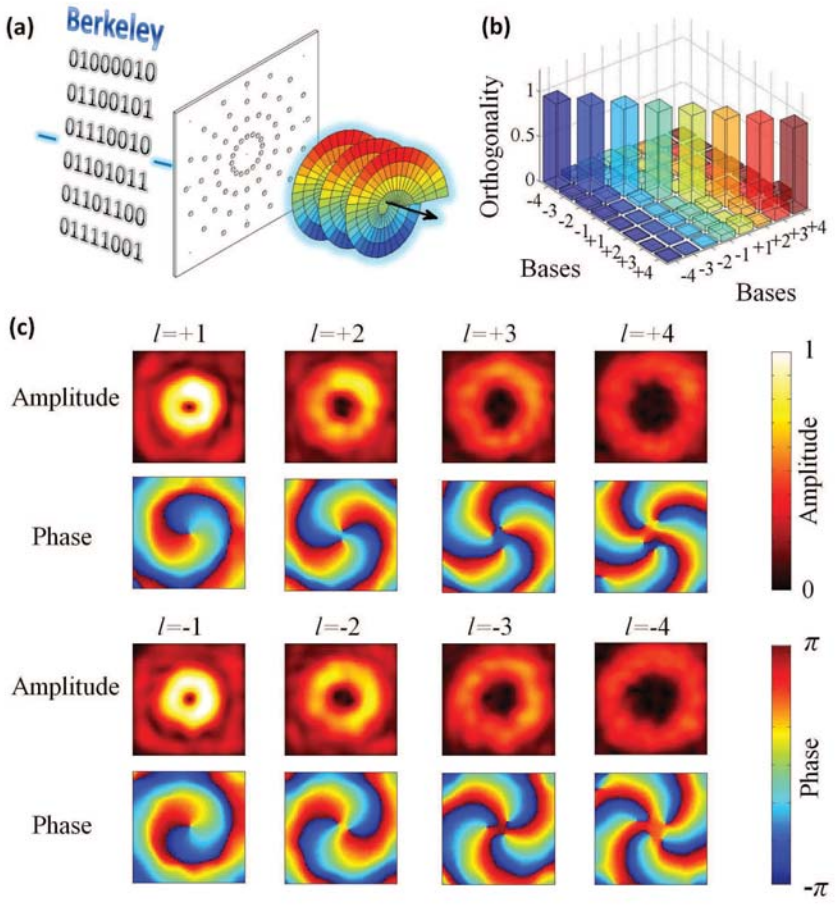


Figure 7.1: *Acoustic communication using vortex beams with OAM charges -4 to +4. (a) Experimental setup of acoustic communication with vortex beams. A computer controlled digital to analog circuit generates signal to control four rings of transducers (with sixteen transducers equally spaced on each ring) and emit information encoded into multiplexed acoustic vortex beams into free space at 16 kHz. The radii of these four rings are 3, 6, 9, and 12 wavelengths. (b) Measured orthogonality relations between the bases formed by acoustic vortex beams with OAM charges -4 to +4. Each of the bars is calculated by forming the inner products between the measured pressure fields of the two corresponding bases. The norm of each basis is normalized to unity. The crosstalk between the bases is less than -8.54 dB. (c) Measured pressure field amplitudes and phases of acoustic vortex beam bases with OAM charges -4 to +4 at 100 wavelengths (2.14 m) away from the emitting plane in air. The scanning area covers 22.4 wavelengths by 22.4 wavelengths (48 cm by 48 cm) with 26 by 26 resolutions. Thermal and rainbow scale colorbars are used for the measured amplitude and phase fields, respectively.*

of the letters in Figure 7.2 to perform inner products with the eight bases set in Figure 7.1. The calculated signals obtained experimentally from the receiver side are shown in Figure 2b, matching well with the binary representations in Figure 7.2. Therefore, the word "Berkly" is sent through multiplexed acoustic vortex beams with OAM charges -4 to +4 at the same frequency. This multiplexing method provides an extra dimension for information encoding in acoustic communications and increases the data transmission rate for all binary information and files.

7.5 Demultiplexing with Inner Product Algorithm

The orthogonality relation between the eight bases in Figure 7.1 and the demultiplexed information in Figure 7.2 are obtained by forming inner product

$$I_{il} = \frac{\int p_i^* p_l da}{\int p_l^* p_l da}, \tag{7.1}$$

where $p_l = \exp(j\beta_l)$ is the pressure field (including amplitude A_l and phase β_l) of vortex beam with OAM charge l, and $p_i = \exp(j\beta_i)$ is the pressure field of other vortex beams or multiplexed waves. The symbol $*$ denotes the complex conjugate of the corresponding variable. This integration is over the scanning area of the receiver array. The information signals are normalized such that $I_{ll} = 1$.

7.6 Generation of Acoustic Vortex and Multiplexed Beams

The acoustic emitting plane in our experiment contains four rings of emitters (Figure 7.3). Each ring consists of sixteen equally spaced speakers. The radii of the rings are 3, 6 9, and 12 wavelengths. The relative phases of the speakers used to emit acoustic vortex beam with orbital angular momentum (OAM) topological charge l are $\psi = l\theta$, where θ is the azimuthal angle between the speaker and reference. All speakers emit with identical amplitude for each OAM. Because the emitting plane is not significantly large compared with the wavelength, the emitted vortex beams expand along propagation direction. To compensate this beam expansion, a phase increment $\delta = \pi/2$ is applied along the radial direction to generate a conical focusing pattern.

The multiplexing of vortex beams with different OAM charges is accomplished by summing the signals required to generate these topological charges in the digital processor, which is then sent to the speakers to emit the multiplexed beam. This summation procedure is equivalent to create an interference pattern between the multiplexed vortex beams. Such a multiplexing procedure requires the modulation of amplitude and phase of each speaker. Here, we take the signal that the speaker at θ emits for a multiplexed beam containing two

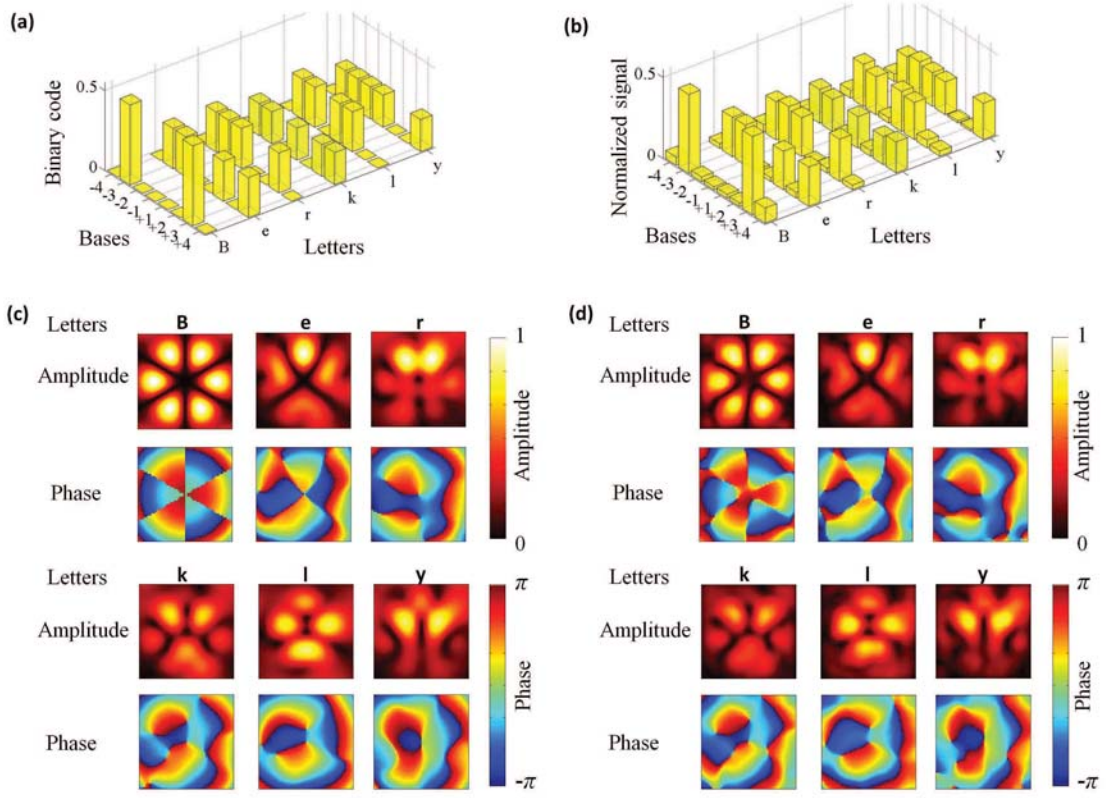


Figure 7.2: *Experimental demonstration of acoustic communication using multiplexed acoustic vortex beams. (a) Binary (ASCII) representations of the letters in the word "Berkly". Each letter contains eight bits (one byte) of information. Each byte contains the same amount of total amplitude, i.e. the signal bars in each letter sum up to unity. This amplitude amount is equally distributed into the vortex beams forming the multiplexed signal. A multiplexed beam formed by the eight orthogonal vortex beams with OAM charges -4 to +4 is capable to convey the information of each letter. (b) Measured signals of the letters in the word "Berkly". The bars are calculated by forming the inner product between the measured pressure fields of the multiplexed signal and the bases. The norms of the bases are normalized to unity. Like (a), each letter contains the same amount of total amplitude, which is equally distributed in the on-channels when sending. (c) Calculated pressure field amplitudes and phases of the multiplexed signal of the letters in the word "Berkly". The field patterns of the letters are superimposed that one cannot judge the information without demultiplexing through inner product. (d) Measured pressure field amplitudes and phases of the multiplexed signal of the letters in the word "Berkly". The experimental results match with the calculated fields in (c). Colored scale bars are used for the amplitude and phase fields, respectively.*

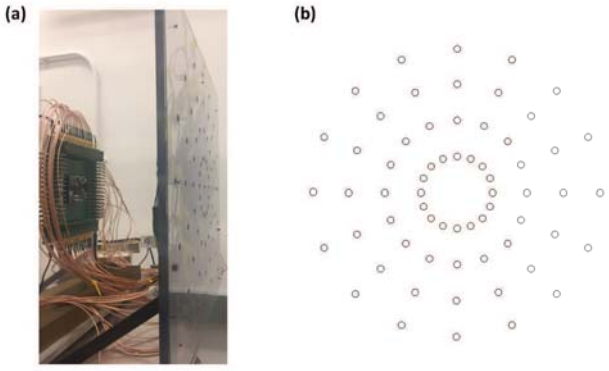


Figure 7.3: *Active phase array used in our experiment. (a) Experimental setup. The digital processor on the left drives the speakers mounted on the plastic frame. (b) Pattern of the emitting array containing 64 speakers. Each circle represents a speaker. These speakers form four rings with radii 3, 6, 9, and 12 wavelengths. Each ring contains 16 equally spaced speakers.*

OAM charges as an example. The multiplexed signal is

$$S = A\cos(\omega t + l_1\theta) + A\cos(\omega t + l_2\theta) = 2A\cos[(l_1 - l_2)\theta]\cos(\omega t\frac{l_1 + l_2}{2}\theta), \qquad (7.2)$$

where ω is the angular frequency of the acoustic wave, A is the wave amplitude, l_1 and l_2 are the topological charges of the two vortex beams. Thus, the amplitude and phase of this speaker are tuned to $2A\cos[(l_1 - l_2)\theta]$ and $(l_1 + l_2)\theta/2$ to emit the multiplexed wave. The amplitude and phase of each speaker required for multiplexed signal containing more than two OAM charges are calculated similarly in the digital processor.

7.7 Bit Error Rate

Bit error rate (BER) is a standard statistical criterion to characterize the performance of a communication system. In our experiment, the BER is calculated statistically from the measured pressure fields of the 256 possible combinations of the eight bases (Section 7.8). For the present communication system, with 26 × 26-resolution receiver array, the BER is $10^{-6.5}$ at a 20 dB signal to noise ratio (SNR) level, indicating that the OAM communication is reliable. To further characterize the performance of our communication system, we vary the SNR of the input signal generated from the digital processor and measure the effect on the BER. The BER increases as the SNR becomes smaller (Figure 7.4). The BER and SNR exhibit the relation $\text{BER} = 1/2\text{erfc}(\sqrt{E_b/N_0}) = 1/2\text{erfc}(\sqrt{\text{SNR}/(8.00.4)})$ (Figure 7.4), where E_b is the signal energy associated with each user data bit and N_0 is the noise spectral density. The energy per bit to noise power spectral density ratio E_b/N_0 is given by the ratio

between SNR and spectral efficiency [137, 151]. Thus, the spectral efficiency of our communication system is 8.0 ± 0.4 (bit/s)/Hz, which can be further increased by using more OAM charges in the data transmission process, and is already higher than all other demonstrated acoustic communication systems to our knowledge [128–132]. Such high spectral efficiency is achieved without applying other modulation techniques. Indeed, this new spatial OAM degree of freedom is compatible with other acoustic communication technology. Therefore, the use of our OAM multiplexing method will increase the data transmission rate of the cutting-edge acoustic communication systems by eight times.

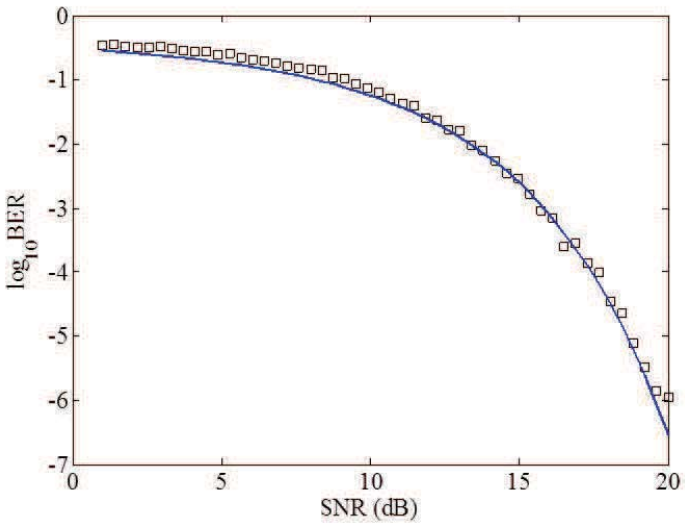


Figure 7.4: *Measured bit error rate (BER) versus signal to noise ratio (SNR) of acoustic OAM communication with 26 × 26 sensor array used in the receiver. The squares are measured data with all bytes have the same total amplitude, which is equally distributed in the on-channels of the byte. The BER decreases with increasing SNR. At 20 dB SNR level, the BER is* $10^{-6.5}$*, which is smaller than the forward error correction (FEC) limit and can still be corrected by standard FEC approaches [152], confirming that our communication system with acoustic OAM is reliable. The blue curve is a regression curve of the experimental data. The measured results fit with this regression curve* $BER = 1/2erfc(\sqrt{SNR/(8.0 \pm 0.4)})$*, indicating the spectral efficiency to be* 8.0 ± 0.4 *(bit/s)/Hz. The theoretical limit of the spectral efficiency is given by the number of orthogonal channels used for data transmission, in this case is 8 bit/s/Hz. Therefore, our acoustic communication device with eight OAM charges employed for information encoding is already working at the theoretical limit.*

7.8 Experimental Measurement of Bit Error Rate and Signal to Noise Ratio

To obtain the bit error rate (BER) and characterize the performance of our communication system with acoustic OAM, we measured the pressure fields of the $2^8 = 256$ possible combinations of the eight bases. The signal of the pressure field is measured within 300 ms, corresponding to a 3 Hz bandwidth. The inner products are calculated for all the on and off channels. With the statistical parameters (average μ_1 and μ_0 and standard deviation σ_1 and σ_0 for on and off channels, respectively), two Gaussian curves are plot in Figure 7.5 for the on and off channels. The error bits are the points of on channels below and off channels above the crossing of the two curves. Thus, the statistical BER is the ratio between the shaded (green) area and the whole area under the two curves.

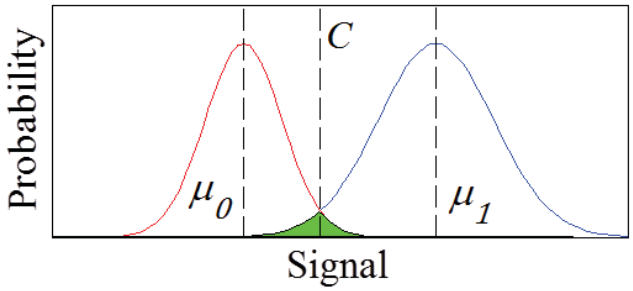


Figure 7.5: *Method used for BER calculation. The two curves are Gaussian with average μ_1 and μ_0 and standard deviation σ_1 and σ_0 for on (blue) and off (red) channels, respectively. C is the crossing of the two curves and is set as the criterion to judge if the signal is on or off. The error bits are on channels below C and off channels above C. The BER is given by the ratio of the green area and the area below the two curves.*

The effect of down-sampling on the BER is measured by varying the number of sensors in the receiver array between 8 and 68. These sensors form four rings with radii 5.4, 6.7, 8, and 9.3 wavelengths (Figure 7.6). For array with $N = 4n + r$ (n and r are integers and $r < 4$) sensors, the inner r rings have $n + 1$ equally spaced sensors and the outer $4 - r$ rings have n equally spaced sensors.

7.9 Design of Receiver Array

A receiver array with fewer sensors is usually desired for practical communications. To provide a design guideline for receiver arrays, we perform a down-sampling experiment to study the effect of receiver resolution on the communication performance. The receiver array contains sensors forming four-ring pattern with the number of microphones reducing from 68 to 8 (Section 7.8). The decreasing resolution increases the BER of the communication

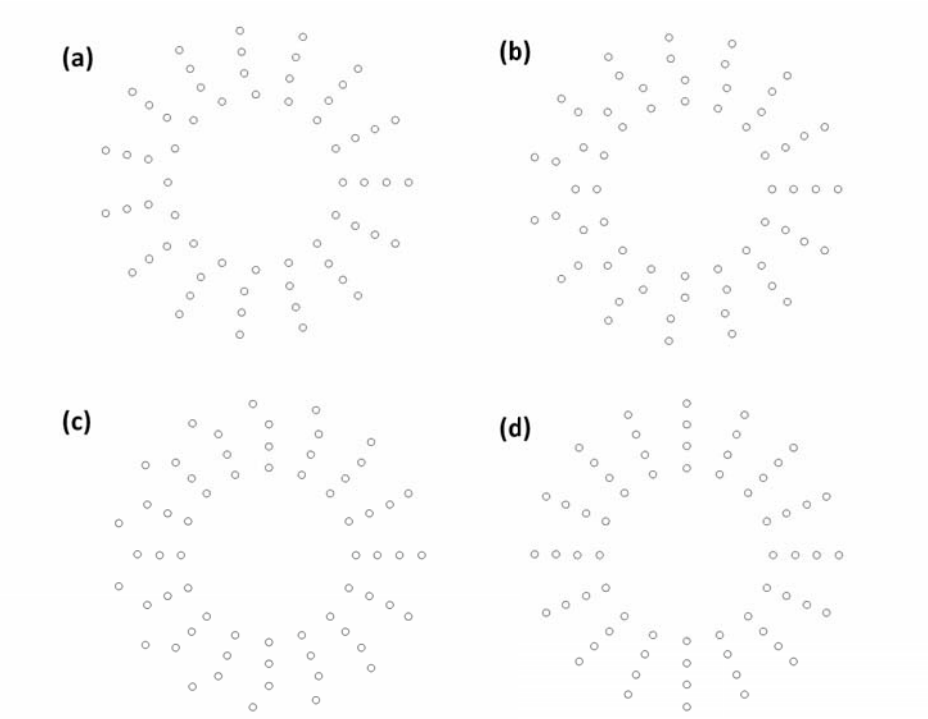


Figure 7.6: *Examples of receiver arrays used to measure the BER versus SNR response. Each circle represents a microphone. The array contains (a) 61, (b) 62, (c) 63, and (d) 64 microphones. These microphones form four rings with radii 5.4, 6.7, 8, and 9.3 wavelengths. For array with $N = 4n + r$ (n and r are integers and $r < 4$) sensors, the inner r rings have $n + 1$ equally spaced sensors and the outer $4 - r$ rings have n equally spaced sensors.*

system (Figure 7.7). A receiver array with 34 sensors results in BER $= 2 \times 10^{-3}$, marking the forward error correction (FEC) limit [152]. Communication errors below this limit can be corrected with standard FEC methods [152]. The BER of a system with 68 sensors for the identical byte total amplitude case is $10^{-6.3}$. Further increasing the number of sensors in the receiver array does not have a significant improvement in the BER (Figure 7.7). Thus, an optimized design of receiver array for practical applications can be realized by minimizing the number of sensors at the specified BER performance requirement.

7.10 Time Interval between Two Sequential Letters

To study the effect of using short pulse (i.e. short time interval between two sequential letters), we perform simulations with a three-cycle pulse, corresponding to 187.5 s interval between two sequential letters (Figure 7.8). The received patterns for the word “Berkly” at

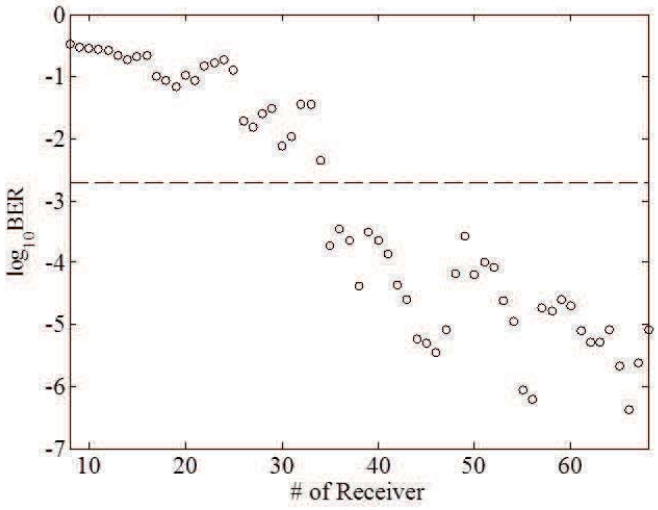


Figure 7.7: *Measured BER dependence of number of sensors. The circles are measured data with all bytes have the same total amplitude, which is equally distributed in the on-channels of the byte. The BER decreases with increasing number of sensors in the receiver array from 8 to 68 microphones with the pattern of the array shown in the Section 7.8. The dashed line marks the FEC limit which determines the maximum error rate that can still be corrected by standard FEC approaches, which is BER* $= 2 \times 10^{-}3$ *[152]. This BER limit corresponds to a minimal required receiver array with 34 sensors in our experiment. Further increasing the number of receivers will not improve the BER significantly.*

100-wavelength away from the source array are shown in Figure 7.8. It can be seen that the patterns obtained from this three-cycle pulse is the same as those shown in Figure 7.2 of the main text.

In order to account for a realistic broadband detection, we provide here new experimental results obtained with the shortest integration time available to our lock-in amplifier (SR-830). Figure 7.9 shows that a shorter integration time (300 s, 4.8 cycles at 16 kHz) provides the same performance as the 300 ms case reported in the manuscript.

7.11 Discussions

In conclusion, orthogonal acoustic vortex beams with different OAM topological charges provide more physical channels for information transmission. The direct multiplexing approach employed in this paper demonstrates the possibility of high rate acoustic communications using OAM. The spectral efficiency of our experiment with OAM charges between -4 and +4 reaches 8.0 ± 0.4 (bit/s)/Hz, which is the highest among the existing acoustic communication systems [128–132], and can be further increased by using more topological charges for data

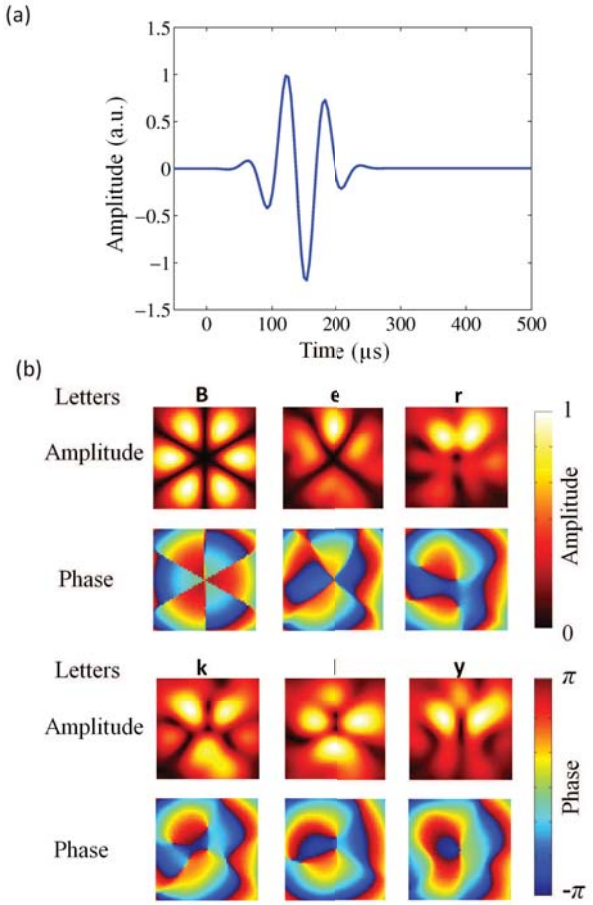


Figure 7.8: *Full wave simulation of acoustic communication with orbital angular momentum multiplexing with three-cycle pulse. (a) The pulse profile of the three-cycle pulse used for simulation. (b) Obtained amplitude and phase patterns for the word "Berkly" using the two-cycle pulse for communication.*

encoding. The OAM signal is readily demultiplexed using an inner product algorithm on the receiver side. The BER analysis confirms the reliability of acoustic communication with OAM, even with a reduced amount of receivers. This OAM communication method provides a new and independent basis for high throughput acoustic information exchange and data transmission, which can be readily extend to underwater environments where acoustics is the only method for long range sensing and communications.

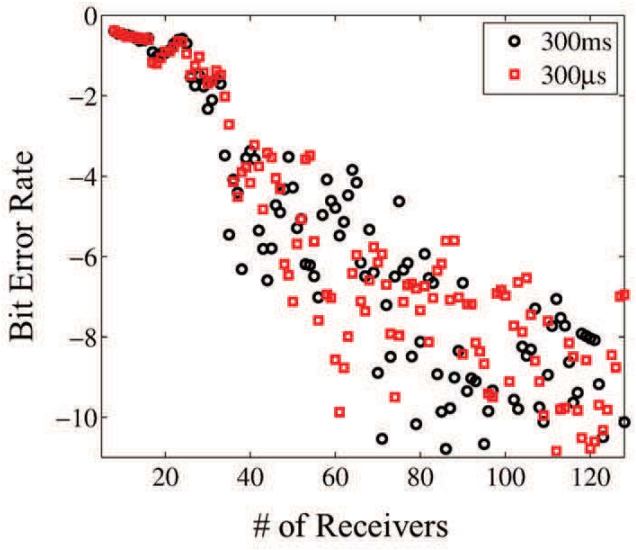


Figure 7.9: *Bit error rate (BER), which characterize the communication performance of the system, with varying number of receivers for the two integration time intervals. It can be seen that the BER performances for these two cases are the same.*

7.12 Methods

Our experimental setup contains 64 PUI AST-1532MR-R speakers forming the four rings of emitter array in Figure 7.3 on an acrylic frame fabricated by waterjet. These 64 speakers are modulated by a customized designed digital processor with 65 analog output channels from CNDLAB Inc. MATLAB program is used to drive this digital processor to control the emitter array. A CUI CME-1538-100LB microphone fixed on a VELMEX motor-controlled translational stage to mimic the receiver arrays. The received signal is amplified by a Reson VP2000 EC6081 voltage preamplifier and read by a Stanford Research Systems SR830 lock-in amplifier. Both amplitude and phase are recorded from the lock-in amplifier.

Chapter 8

Acoustic Spin

8.1 Introduction

Spin is a fundamental physical property, which describes the intrinsic angular momentum carried by particles and waves [153–155]. It provides an extra degree of freedom for the control of wave propagation, and wave matter interactions. Optical spin, as a result of the rotating electric vector field, has led to many interesting phenomena including spin orbital coupling and the quantum spin Hall effect [156–165]. Unlike optical waves, acoustic waves that propagate in fluids can usually be described by scalar pressure fields [166]. Therefore, acoustic spin was considered to be not possible [150, 167–169]. Here, we discover the existence of spin in free space acoustics as a result of the rotation of local particle velocity field created by two traveling acoustic beams oriented perpendicular to one another. We measured the acoustic spin angular momentum and the spin-induced torque that acts upon an absorptive meta-atom. Spin dependent propagation phenomenon was observed in evanescent waves guided by a metamaterial waveguide, where the propagation direction of the wave is locked to its spin. The discovery of acoustic spin opens a new door in acoustics and for applications in underwater communications and ultrasonic biomedical imaging.

Spin angular momentum is represented by the rotation of a vector field [153, 154], which provides an additional degree of freedom for controlling wave propagation and wave matter interactions. The spin angular momentum of light arises from the rotation of the electric fields polarization [155], which can be expressed both in circular polarization (when the axis of polarization rotation is parallel to the propagation direction) [156] and transverse spin [157] (when the axis of rotation is perpendicular to propagation). These two spin degrees of freedom have been foundational for the study of light-matter systems, for example with the discoveries of strong spin-orbit interactions and the quantum spin Hall effect with light [158–165].

Since acoustic waves in fluid, such as in air and in water, can usually be described by scalar pressure fields [166], the existence of a spin degree of freedom was considered impossible [150, 167–169]. Still similar to optical spin, one may consider acoustic spin as a rotating vector

field such as local particle velocity. A single acoustic plane wave propagating in free space has only a longitudinal velocity component, and any local particle will be confined to oscillate along the propagation direction without rotation [166]. Yet, the demonstration of a local rotation by acoustic waves would signify the observation of spin angular momentum. This spin angular momentum that we describe is different from the orbital angular momentum observed in acoustic vortices that represent the circulation of energy flux [150, 167–169] or helical shaped acoustic beams associated with a twisted wavefront [139–144].

8.2 Existence of Acoustic Spin

Here, we report the existence of spin angular momentum in free-space acoustics characterized by the rotation of a local particle velocity. A spinning local particle velocity $\mathbf{v}$ can be decomposed into two perpendicular components v_x and v_y that are the same in amplitude but with a 90 degrees difference in phase. The local particle velocity rotates clockwise or counterclockwise when facing the z axis depending on the relative phase difference of the components (Figure 8.1). For convenience, we define the clockwise or counterclockwise when facing the z axis acoustic spin as spin up or spin down, respectively. This rotating particle velocity field can be observed with the interference of two beams of equal amplitude propagating perpendicularly with respect to one another (Figure 8.1). Each beam contributes a component to the particle velocity field (v_x or v_y) in the interference pattern. The phase difference between these two orthogonal components is determined by the local particles position, which can produce either spin up or spin down rotation.

To quantify the strength of the acoustic spin, we define the angular momentum carried by the spinning acoustic field in a unit volume as $\mathbf{s} = \mathrm{Im}(\rho_0 \mathbf{v}^* \times \mathbf{v})/2\omega$, where ρ_0 is the density of air and ω is the frequency of the acoustic field (Supplementary Materials). We refer to $\mathbf{s}$ as the spin density. The nonzero cross-product of the complex conjugate particle velocity with itself characterizes the rotation of the particle velocity field. For a circularly rotating particle velocity field, the spin density reaches its maximum value, corresponding to the strongest angular momentum. For a linearly oscillating velocity field, both the spin density and the angular momentum reduce to zero and correspond to zero angular momentum.

8.3 Derivation of Acoustic Orbital and Spin Angular Momentum

The acoustic momentum flux density tensor is given by $\mathbf{M} = (p + P)\mathbf{I} + \rho_0(\mathbf{v}^*\mathbf{v})$, where p is the pressure field, P is the second order acoustic radiation pressure, $\mathbf{I}$ is the unit tensor, ρ_0 is the air density, and $\mathbf{v}$ is the particle velocity field [170]. The first term associated with the acoustic radiation force does not contribute to the angular momentum. The time averaged

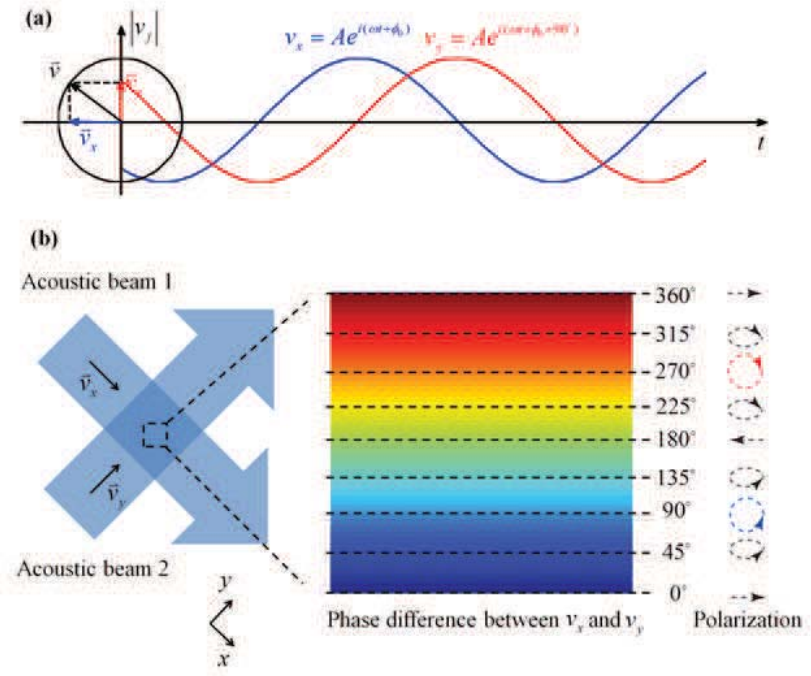


Figure 8.1: *Acoustic spin as a rotating particle velocity field. (a) A rotating particle velocity (black arrow) can be decomposed into two components v_x (blue arrow) and v_y (red arrow) along x and y directions. The two components shown as the blue and red lines are 90 degrees out-of-phase. (b) Acoustic spin in the interference of two acoustic beams. Two beams with equal amplitudes propagating along x and y directions contribute v_x and v_y components of the particle velocity field, respectively. The phase difference between v_x and v_y is the function of the position. The zoomed-in region shows an area where the phase difference between v_x and v_y changes from 0^o to 360^o. When the phase difference is 90 or 270 (equivalent to -90) degrees, the local particle velocity field is rotating circularly, resulting in spin up (blue) or spin down (red) acoustic field; When the phase difference is 0, 180, or 360 degrees, the particle velocity field is oscillating along a line. In other cases, the local particle velocity rotates elliptically.*

acoustic angular momentum in the xy plane is given by

$$\mathbf{J} = \mathrm{Im}\{\frac{1}{2\omega}\int \mathbf{r} \times (\rho_0 \mathbf{v}^* \mathbf{v}) dl\} = \mathrm{Im}\{\frac{1}{2\omega}\int \nabla \cdot [\mathbf{r} \times (\rho_0 \mathbf{v}^* \mathbf{v})] d^2\mathbf{r}\}, \tag{8.1}$$

where $\mathbf{r}$ is the position vector and ω is the frequency. Applying tensor calculus, the angular momentum becomes

$$\begin{aligned}\mathbf{J} &= -\mathrm{Im}\{\frac{\rho_0}{2\omega}\int[\nabla\cdot(\mathbf{v}\mathbf{v}^*)\times\mathbf{r}+\sum_{i=x,y}\mathbf{e}_i\cdot(\mathbf{v}\mathbf{v}^*)\times\mathbf{e}_i]d^2\mathbf{r}\}\\ &= \mathrm{Im}\{\frac{\rho_0}{2\omega}\int([\mathbf{r}\times\nabla\cdot(\mathbf{v}\mathbf{v}^*)]+\mathbf{v}^*\times\mathbf{v})d^2\mathbf{r}\},\end{aligned} \tag{8.2}$$

where $\mathbf{e}_x$ and $\mathbf{e}_y$ are unit vectors along x and y directions. The first term gives the orbital angular momentum of the acoustic field with its density to be $\mathbf{l} = \mathrm{Im}\rho_o[\mathbf{r}\times\nabla\cdot(\mathbf{v}\mathbf{v}^*)]/2\omega$. The second term yields the spin density as $\mathbf{s} = \mathrm{Im}(\rho_0\mathbf{v}^*\times\mathbf{v})/2\omega$. Similar separation of angular momentum into spin and orbital parts can be found in optics [155]. This spin density can also be written as $\mathbf{s} = \rho_0\mathbf{v}^*\sigma\mathbf{v}/2\omega$, where $\sigma = \begin{pmatrix}0 & -j\\ j & 0\end{pmatrix}$ is the spin operator. The physical differentiation between the spin and orbital angular momentum is that a probe meta-atom rotates around the particle center when placed at an arbitrary location in the acoustic spin field, while the rotation of the same meta-atom is around the center of the acoustic field when the wave possesses orbital angular momentum.

8.4 Generation of Acoustic Spin in Interference Pattern

In experiment, perpendicular acoustic beams are generated by two speakers placed at two neighboring sides of the setup (Figure 8.2). By measuring the time dependent pressure field p (Figure 8.2), the local particle velocity is given by $\mathbf{v} = -\nabla p/j\omega\rho_0$, where j is the imaginary unit. We found that the velocity rotates clockwise at the center, resulting in a spin up acoustic field (Figure 8.2). The measured pressure field and spin density shown in Figures 8.2d and 8.2e agrees with our simulations (Figures 8.2b and 8.2c). In contrast, no spin is observed when only one acoustic beam is generated (Figures 8.2f and 8.2g). It is important to notice that the acoustic spin is different from the vortexes induced by chiral or periodic structures [150, 167–169]. The vortexes possess particle velocity field rotates about the center of the wave, while the particle velocity vector spins about itself everywhere in the field with acoustic spin.

8.5 Acoustic Spin Induced Torque

The acoustic spin carries angular momentum, which can induce a torque through a spin-matter interaction. In our study, we placed an acoustic meta-atom that supports a dipole resonance in a spinning particle velocity field. If the meta-atom is lossy due to the viscosity of air or the mechanical deformation of the meta-atom, the excitation of the dipole moment is always slightly delayed compared to the exciting velocity field [171]. This means that the

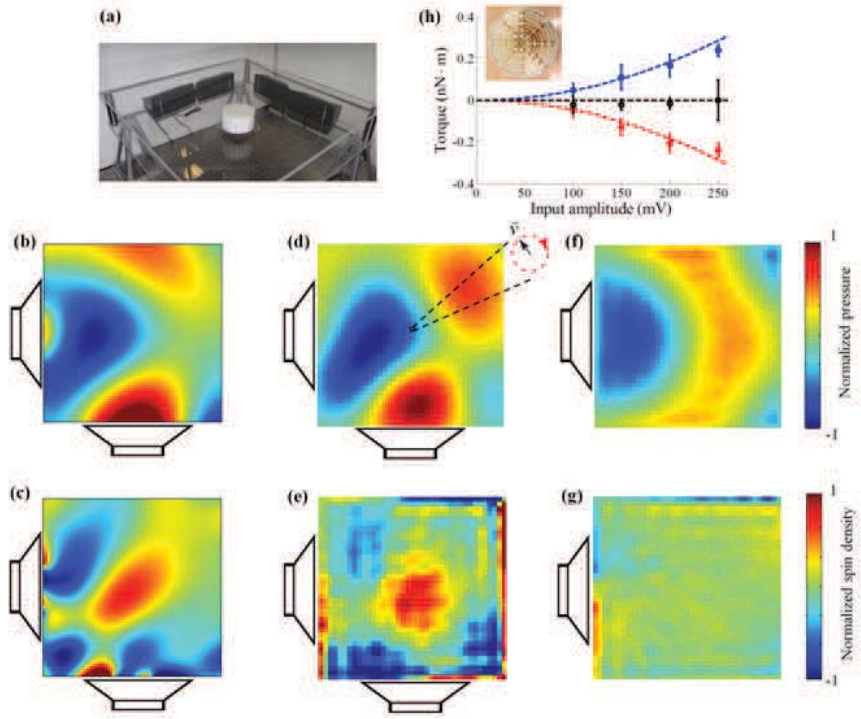


Figure 8.2: *Experimental observation of acoustic spin. (a) Experimental setup for the measurement of acoustic spin resulted from the interference of two perpendicular beams and the spin induced torque acting on a coiled space acoustic meta-atom. Two pairs of high power speakers at two neighboring edges emit at 870 Hz with a 90-degree phase difference. The transparent glass walls at the top and the bottom confine acoustic waves propagating at the fundamental mode, mimicking an ideal two-dimensional scenario extended infinitely in the perpendicular direction. The coiled space meta-atom is hanged at the center using a thin copper wire. (b) Simulated and (d) measured pressure fields show a 90-degree phase difference at the center of the interference pattern where the local particle velocity rotates clockwise, resulting in a spin up field. (c) Simulated and (e) measured spin density distributions show that the spin density reaches its local maximum at the center where the meta-atom is located. (f) Measured pressure field when only one speaker is on. (g) Measured spin density when only one speaker is on. No spin exists in this case. The measured area for (d), (e), (f), (g) is 40 cm × 40 cm. (h) Measured torques acting on the coiled space meta-atom (inset) versus input voltage amplitude loaded on the speakers. The spin up or spin down acoustic wave applies a negative or positive torque (with respect to z axis in Figure 8.1b) on the particle. The torques induced by the spin up and spin down waves are equal in amplitude and follow a quadratic relation with the input amplitude, in agreement with our theoretical prediction that the torque is proportional to the spin density.*

excited dipole moment is not parallel with the exciting velocity field. Since an acoustic dipole tends to align with the velocity field, the misalignment provides torque to drive the meta-atom rotation. In other words, the meta-atom obtains angular momentum by absorbing the spin angular momentum of the acoustic field.

To measure the spin induced torque, we made a coiled space meta-atom (the inset of Figure 8.2h and Section 8.6), which supports a dipole resonance at 870 Hz. The meta-atom is designed to be symmetric with a cylindrical shape to eliminate any possible torque due to the geometry itself. It is designed to be subwavelength in diameter so as to represent a probe to interact with the local spin. The meta-atom is hanged by a thin copper wire at the center of the interference fields (Figure 8.2a). A mirror is attached on the meta-atom to reflect a laser beam onto a ruler, which converts the rotation of the meta-atom into the deviation of laser spot. The value of the torque is obtained by multiplying the torsional spring constant with the measured rotation angle (Section 8.7).

The torques induced by spin up and spin down acoustic waves are of equal amplitude along Cz and $+z$ directions, respectively (Figure 8.2h). The measured torques follow a quadratic relation with the amplitude of the input voltage loaded on the speakers, which shows that the spin induced torque is linearly proportional to the spin density as predicted (Section 8.9). The noise is mainly contributed by environmental random vibrations. As a control experiment, the torque from one acoustic beam alone is undetectable, which means that a single beam without interference does not carry angular momentum. It is also shown that the orbital angular momentum density of the interfering beams is zero, indicating that the measured torque is a result of spin-matter interaction (Section 8.9).

8.6 Dipole Resonance of the Cylindrical Coiled Space Meta-Atom

Cylindrical coiled space meta-atom has the ability to slow sound speed and reduce the resonant frequency of dipole resonance [47]. However, previously design coiled space meta-atom is asymmetric along the azimuthal direction that can result in an applied torque when interact with acoustic plane waves [47]. To rule out this asymmetric effect, we design a symmetric coiled space meta-atom (Figure 8.3a) with its dipole mode shown in Figure S1b. This dipole resonance interacts with the rotating particle velocity of acoustic transverse spin through thermo-viscous effect. The full wave simulation of the transmission through the meta-atom considering the thermo-viscous effect [48] indicates that the dipole resonance occurs at 890 Hz (blue curve is Figure 8.3c). The experimental measurement of the transmission shows that this dipole resonance occurs at 870 Hz (black circles in Figure 8.3c), which is chosen as the frequency for the measurement of spin induced torque in Figure 8.2 of the main text to enhance the interaction.

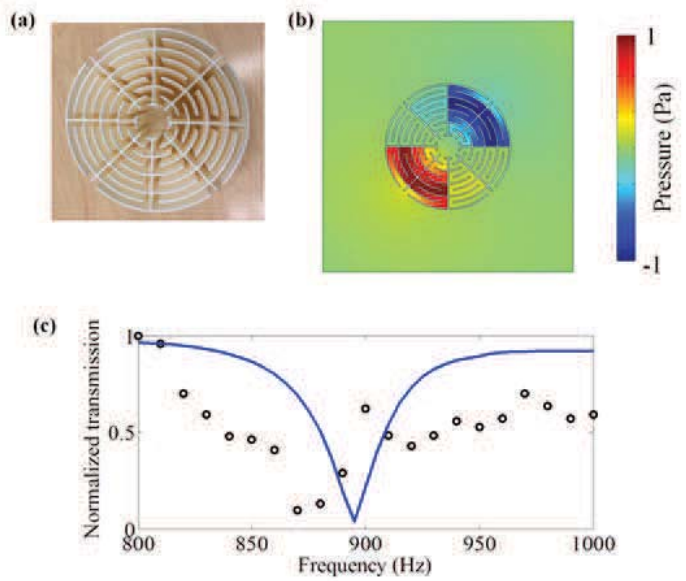


Figure 8.3: *Symmetric coiled space meta-atom. (a) The meta-atom fabricated by 3D printer with ABS plastic. (b) The pressure field of the dipole mode shape of the meta-atom. (c) Calculated with thermo-viscous effect (blue curve) [47] and measured (black circles) of the normalized transmission through the meta-atom. From the calculation, the dipole resonance occurs at 890 Hz. The experimental result shows that this dipole resonance occurs at 870 Hz, which is chose for the measurement of the spin induced torque.*

8.7 Measurement of the Spin Induced Torque

Because the spin induced torque is small, we apply Cavendishs method to amplify measurement of the rotation of the meta-atom θ with a laser beam [172]. The spin induced torque is given by

$$\tau = \kappa\theta, \tag{8.3}$$

where the rotational stiffness of the copper wire is given by

$$\kappa = (2\pi f_0)^2 I. \tag{8.4}$$

Here, the rotational resonant frequency of the suspended meta-atom with the copper wire is measured from the frequency response of the free rotational vibration of the meta-atom $f_0 = 0.02$ Hz and the moment of inertia of the meta-atom is given by

$$I = \frac{mr^2}{2}, \tag{8.5}$$

where the mass and the radius of the meta-atom are $m = 1.4$ g and $r = 5$ cm. When measuring the rotation of the meta-atom, rotational vibrations above 0.005 Hz are filtered

to avoid the strong influence of the rotational resonance on the torque measurements. The rotational vibrations of the suspended meta-atom due environmental thermal fluctuation and ground vibration contribute to the measurement error.

8.8 Response of the High Power Speakers Used for Torque Measurement

To characterize the effect of the high power speakers on the spin induced torque measurement, we perform the measurement of the response of the speakers with varying input voltage amplitude loaded on the speakers using a microphone (Figure 8.4). It can be observed that the speakers perform linearly before the saturation at 250 mV input voltage. Therefore, we choose the input voltage amplitude to be smaller than 250 mV for our spin induced torque measurement in Figure 8.2 of the main text.

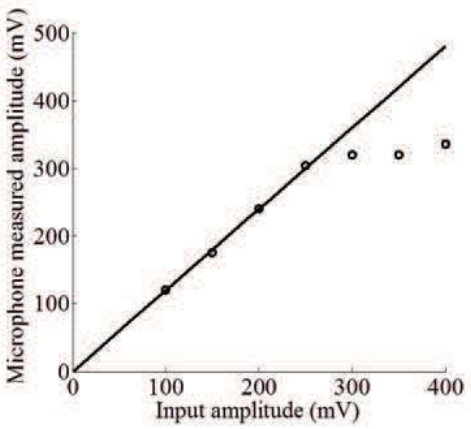


Figure 8.4: *Speaker response with varying input voltage amplitude of the high power speakers used for spin induced torque measurement. A microphone is fixed at a location far away from the speakers to avoid the saturation of the microphone response. The speakers behave linearly before the saturation occurs at 250 mV input voltage.*

8.9 Relations between the Torque, Input Amplitude, and Spin Density

As shown in Figure 8.2b of the main text, the measured torque and the input voltage amplitude follow a quadratic relation. From Figure 8.4, we observe the input amplitude is linearly related to the microphone measured amplitude, i.e. the amplitude of the pressure field. According to Eq. (8.9) in later discussion, the amplitude of the particle velocity is

proportional to the pressure field. Thus, the measured torque and the amplitude of the particle velocity field follow a quadratic relation. Because the spin density is given by $\mathbf{s} = \mathrm{Im}(\rho_0 \mathbf{v}^* \times \mathbf{v})/2\omega$, the spin density and the amplitude of the particle velocity field also satisfy a quadratic relation. Therefore, the measured torque is proportional to the spin density.

It can be further confirmed that the torque we measured is dominated by spin matter interaction because the orbital angular momentum of the interference pattern is tiny compared with the spin angular momentum. As derived by Eq. (8.2), the orbital angular momentum of the two interfering beams in Figure 8.2e of the main text is

$$\mathbf{L} = \mathrm{Im}[\frac{\rho_0}{2\omega} \int (\mathbf{r} \times \nabla \cdot (\mathbf{v}\mathbf{v}^*)) d^2\mathbf{r}] = 3.2 \times 10^{-9} \text{ kg} \cdot \text{m}^2/\text{s}. \tag{8.6}$$

The spin angular momentum of the two interfering beams is given by

$$\mathbf{S} = \mathrm{Im}[\frac{\rho_0}{2\omega} \int (\mathbf{v}^* \times \mathbf{v}) d^2\mathbf{r}] = 1.7 \times 10^{-5} \text{ kg} \cdot \text{m}^2/\text{s}. \tag{8.7}$$

Thus, the orbital angular momentum of the measured interference pattern is within numerical error. The measure torque in Figure 8.2 of the main text is dominantly contributed by spin matter interaction.

8.10 Acoustic Spin Dependent Propagation

Spin dependent propagation is a phenomenon where the wave propagation direction is determined by the rotation direction of the spin, which has important use in the realization of chiral quantum circulators and asymmetric wave transports [158–165] in optics. In order to experimentally observe acoustic spin dependent propagation, we exploit the evanescent field produced by a metamaterial waveguide composed of periodic grooves. In this metamaterial waveguide, the evanescent field of an acoustic wave propagates along the waveguide and decays exponentially in the perpendicular direction (Figure 8.5a). The two components of the particle velocity satisfy $v_x = \pm jkv_y/\tau$, where k is the wave number along the waveguide and τ is the decaying constant in the perpendicular direction (Section 8.8). The x and y components of the particle velocity are inherently 90 degrees out-of-phase everywhere. The $\pm$ sign ensures that the propagation direction is locked with the spin direction. The spin up wave propagates to the right and the spin down wave to the left.

The acoustic spin dependent propagation is demonstrated experimentally with the metamaterial waveguide confined by two rigid walls (Figure 8.5b). Four mini-speakers are packed together and mounted in the vicinity of the metamaterial waveguide with their phases aligned 90 degrees relative to each other to mimic a rotating acoustic dipole source (Section 8.12). When this dipole source rotates counterclockwise, it excites the spin down acoustic wave which propagates only towards Cx direction (Figures 8.5c (simulation) and 8.5e (experiment)). On the other hand, the clockwise rotating dipole source excites the spin up acoustic

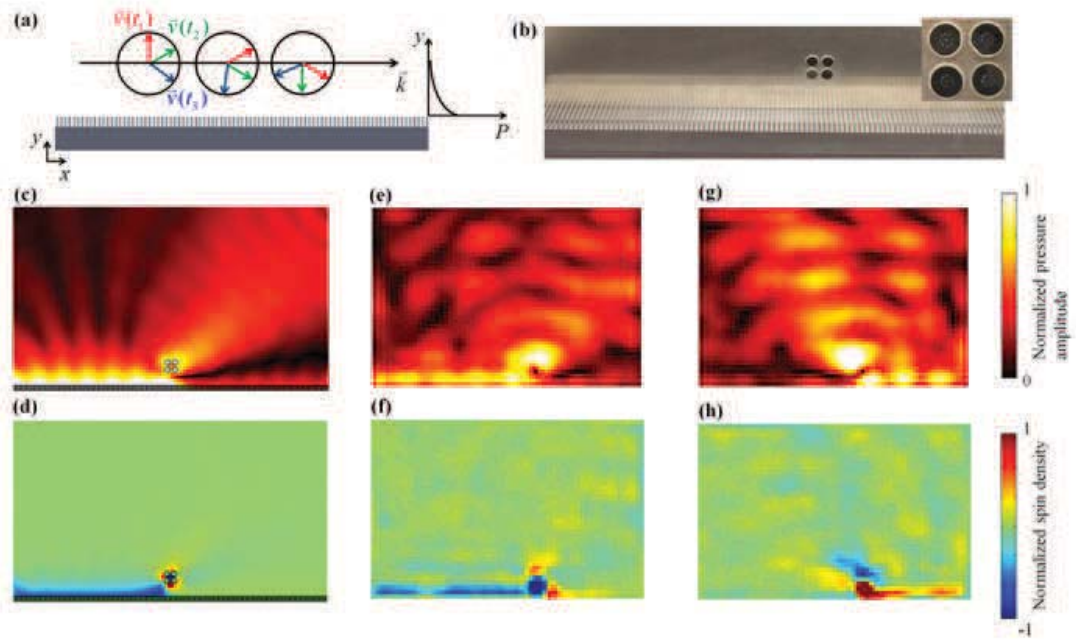


Figure 8.5: *Spin dependent propagation in acoustics. (a) Schematic of local particle velocity field of an evanescent acoustic wave supported by a metamaterial waveguide composed of periodic grooves. The acoustic field outside the waveguide decays exponentially along y axis and propagates along x axis.* $\mathbf{v}(t_1)$ *(red),* $\mathbf{v}(t_2)$ *(green), and* $\mathbf{v}(t_3)$ *(blue) represent the particle velocities at time* t_1*,* t_2*, and* t_3 *with* $0 < t_1 < t_2 < t_3$*, respectively. The local particle velocity rotates clockwise in time. The propagation direction is solely determined by the spin direction, resulting in spin dependent propagation. (b) Experimental setup for demonstrating the spin dependent propagation. Four mini-speakers (inset) are mounted near the acoustic waveguide. A rigid wall on each side confines the acoustic wave propagating in-plane. The four speakers emit at 2 kHz with a 90-degree phase difference between the neighboring speakers, mimicking a rotating acoustic dipole, which excites spin up or spin down acoustic wave determined by the relative phase difference among four speakers. (c), (e), (g) Normalized amplitudes of simulated and measured pressure fields. The acoustic metamaterial waveguide is at the bottom of each figure (not shown). The spin down and spin up acoustic waves are excited in (c), (e) and (g), respectively. The measured area of (e) and (g) is 60 cm* $\times$ *40 cm. The spin down acoustic wave propagates only towards left, while the spin up wave propagates towards right, demonstrating the phenomenon of spin dependent propagation. The thermal color scale is used for the pressure amplitude. (d), (f), (h) Normalized spin density for spin down and spin up acoustic waves in (c), (e) and (g), respectively, confirming the acoustic spin dependent propagation. The jet color scale is used for the spin density.*

wave propagating only towards $+x$ direction (Figure 8.5g). The calculated and measured spin densities further confirm the spin dependent propagation phenomenon (Figures 8.5d,

8.5f, and 8.5h). This spin dependent propagation phenomenon can be further applied to create acoustic circulators and asymmetric wave transport with a rotating meta-atom.

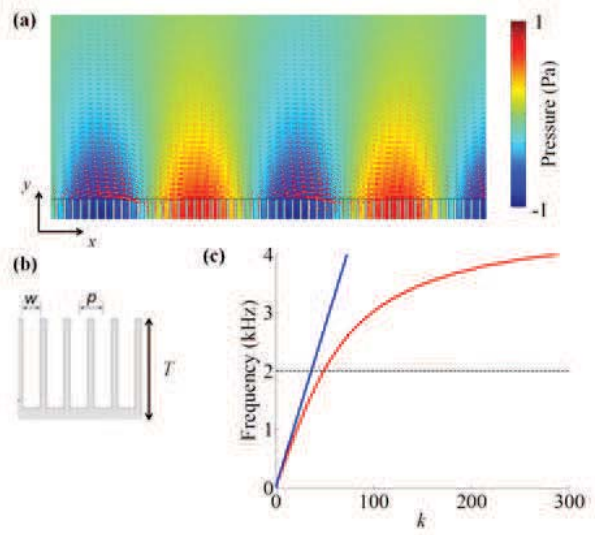


Figure 8.6: *Acoustic wave propagating along the metamaterial waveguide. (a) The pressure field (jet color scale) and particle velocity field (red arrows) of the acoustic wave propagating along the metamaterial waveguide. The wave is propagating along x-direction, while evanescently decaying along y-direction. (b) Geometry of the grooves. The period is* $p = 6.35$ *mm, width* $w = 4.76$ *mm, and depth* $T = 15.9$ *mm. (c) The dispersion relations of the metamaterial waveguide (red) and sound cone (blue).*

8.11 Wave Supported by the Acoustic Metamaterial Waveguide

The acoustic wave supported by the periodic grooves serving as an acoustic metamaterial waveguide in Figure 8.5a of the main text is propagating along x-direction, while decaying evanescently along y-direction (Figure 8.6a). Therefore, the pressure field of the acoustic wave can be expressed as

$$p = Ae^{-\tau y}e^{j(\omega t - kx)}, \tag{8.8}$$

where j is the imaginary unit, A is the amplitude of the pressure wave, ω is the angular frequency, k is the wave number along the propagation direction, and τ is the decaying constant perpendicular to the propagation direction. The particle velocity field is given by

$$\mathbf{v} = -\frac{1}{j\omega\rho_0}\nabla p, \tag{8.9}$$

where ρ_0 is the air density. Thus, the two components of the particle velocity field are

$$v_x = -\frac{1}{j\omega\rho_0}(-jk)p, \qquad v_y = -\frac{1}{j\omega\rho_0}(-\tau)p. \tag{8.10}$$

Thus, the two components of the particle velocity satisfy $v_x = jkv_y/\tau$, indicating they are 90 degrees out-of-phase and the particle velocity field is rotating.

This acoustic metamaterial waveguide has infinite effective density along the x-direction [173]. According to the derivation in [173], the dispersion relation of the acoustic wave propagating along the metamaterial waveguide satisfies

$$k = k_0\sqrt{1 + \frac{w^2}{p^2}\tan^2(k_0 T)}, \qquad k_0 = \omega\sqrt{\rho_y/\kappa_0}, \qquad \rho_y = (\frac{p}{w})\rho_0, \tag{8.11}$$

where κ_0 is the bulk modulus of air, $p = 6.35$ mm is the period, $w = 4.76$ mm is the width, and $T = 15.9$ mm is the depth of the grooves (Figure 8.6b). This dispersion relation is similar to spoof surface plasma and 2 kHz which is below the cut-off frequency is chosen for the demonstration (Figure 8.6c).

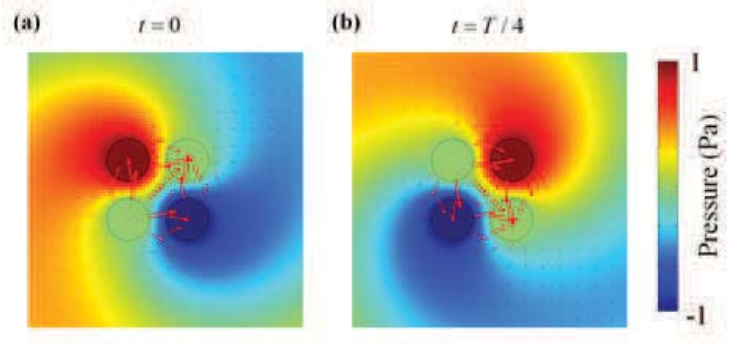


Figure 8.7: *Acoustic rotating dipole mimicked by four speakers. (a), (b) the pressure field (jet color scale) and particle velocity field (red arrows) of the four speakers emitting at 2 kHz with phase increasing by 90 degrees between the neighboring speakers in the clockwise direction at time 0 in (a) and a quarter period in (b), respectively. The acoustic dipole represented by the particle velocity direction is rotating in the clockwise direction.*

8.12 Rotating Acoustic Dipole Created by Four Speakers

The rotating acoustic dipole can be realized by modulating the phase relation of the four speakers in Figure 8.5b of the main text. This is done by tuning the phase of the speakers

such that the neighboring speaker has a phase increased by 90 degrees in the clockwise direction as shown in Figure 8.7. In this case, the particle velocity field (red arrows in Figure 8.7) representing the direction of the acoustic dipole is also rotating in the clockwise direction. To realize a rotating dipole in the counterclockwise direction, we need to tune the speakers such that their phases decrease by 90 degrees in the counterclockwise direction.

8.13 Discussions

In conclusion, we have discovered the existence of spin in acoustics. The spin induced torque is measured to be proportional to the spin density and the spin dependent propagation is demonstrated. The observation of acoustic transverse spin provides a fundamental platform for future studies on acoustic spin physics such as spin orbital interaction, acoustic spin Hall effect, and spin induced non-reciprocal acoustic physics which are important for applications such as wireless underwater communications, on-chip cell sorting, and biomedical imaging.

Chapter 9

Conclusions and Future Works

9.1 Summary of Results and Contributions

This dissertation investigates the design and realization of acoustic metamaterials with properties unprecedented in nature including simultaneous zero effective density and infinite effective bulk modulus, balanced loss and gain media with complex-valued refractive index, and ultrathin metasurfaces for phase front modulations. These nonexisting properties are realized by the judiciously designed resonating structures and active elements. Such new material properties enable unconventional controls of acoustic wave propagation and yield new functionalities such as cloaking, virtual diffusing, collimation, asymmetric wave transport, and subwavelength imaging. Meanwhile, acoustic metamaterials have the capability to control the angular momentum of sound, resulting in novel wave matter interactions. All of these controls of the acoustic wave propagation through metamaterials are critical for practical applications including high speed acoustic communications, high resolution biomedical imaging, non-invasive surgeries, target detections, architecture designs, etc. The detailed conclusions are as follows.

1. Mass density and bulk modulus are the two critical material parameters of media that determine the propagation of acoustic waves. The refractive index and acoustic impedance of a material that are key parameters in the acoustic Snell's law can be derived from the mass density and bulk modulus. The real part of mass density and bulk modulus can be modulated by the resonances of unit cells in the media. Dipolar resonances correspond to the vibration of the center of mass of each unit cell at which the oscillating amplitude is amplified. At a slightly higher frequency, the response of the center of mass of the elements is out-of-phase with the applied force. In this case, the effective mass density becomes negative. Because the mass density is a continuous function of frequency and there exists negative and positive density bands, zero crossings must exist in between these negative and positive density bands where the effective mass density becomes zero. Similarly, monopolar resonances correspond to the deformation of the volume of each unit cell. At frequencies slightly

higher than the resonances, the deformation of the volume is out-of-phase with the applied force, resulting in negative effective bulk modulus and compressibility. Because the compressibility is a continuous function of frequency, there exists zero crossings where the compressibility and inverse bulk modulus become zero. For the case when only one of the mass density and bulk modulus is negative, the refractive index is purely imaginary in which the acoustic waves decay throughout the media and cannot propagate, resulting in isolating frequency bands. These non-propagating frequency bands occur in between the zero crossings of mass density and inverse bulk modulus. In the frequency bands where both the mass density and inverse bulk modulus are negative, the refractive index becomes negative in which medium the acoustic waves propagate with a negative phase velocity. According to Snell's law, at the boundary of negative and positive index media, negative refraction occurs, forming an acoustic flat lens. One can also prove that such acoustic flat lens can be used to develop superlenses with which subwavelength resolution imaging can be realized. By designing the unit cells with special geometries where dipolar and monopolar resonances coexist and degenerate at the Brillouin zone center to form a Dirac-like cone, one can realize a metamaterial with simultaneous zero mass density and inverse bulk modulus where the refractive index becomes zero and the acoustic impedance can be designed to matched with the background. This double zero index metamaterial is used to collimate the cylindrical waves emitted by an acoustic point source and generate acoustic plane waves. For the frequencies above the degenerate point, the metamaterial has positive mass density and inverse bulk modulus. For the frequencies below the degenerate point, the metamaterial has simultaneous negative mass density and bulk modulus. No isolating frequency bandgap is observed in this double zero index metamaterial.

2. The imaginary parts of mass density and bulk modulus of media associate with the amplification and attenuation of acoustic waves propagating in the materials, referred as the gain and loss of the materials. When the gain and loss of the materials in an acoustic system balanced with each other, the system is parity-time (PT) symmetric, i.e. the Hamiltonian of the acoustic system is invariant when apply PT operator. Such PT symmetric acoustic systems possess two different phases: PT "exact" and "broken" phases with a transition point named exceptional point of the system. The eigenvalues of the Hamiltonian are real-valued in the PT "exact" phase and becomes imaginary in the PT "broken" phase. At the exceptional points, total transmission occurs when acoustic waves are incident from either side of the system, while the reflection for acoustic wave incident from one side is zero and the other side exhibits strong reflection. This unidirectional reflection is a result of the complex-valued grating vector introduced by the PT symmetric system that satisfies the phase matching condition of Bragg scattering at one side but not the other. Such unidirectional reflection property can be used for the design of directional detection and cloaking devices. Because the imaginary parts of material parameters are dispersive, the PT symmetric condition where the gain and loss materials balance exactly with each other and the exceptional

points rarely occur at the same frequency. Therefore, the observation of unidirectional reflection experimentally is challenging. This problem can be solved by introducing an additional control degree of freedom like the spacing between the gain and loss media. Once the gain and loss balance with each other, one can tune the spacing between the gain and loss materials to modulate the scattering inside the PT symmetric system, which enables the control of exceptional points and the realization of unidirectional reflection. With this control degree of freedom, one can access exceptional points at multiple frequencies, and flip the unidirectional response of the PT symmetric system.

3. Besides modulating the mass density and bulk modulus of bulk materials, acoustic resonating structures can also be used for the design of ultrathin metasurfaces through which the phase front of the propagating waves can be modulated to realize functionalities like wave steering, cloaking, and virtual diffusing. These metasurfaces consist of elements such as Helmholtz resonators resonating at different frequencies, such that the phase modulations of each element at the working frequency are different. These phase modulating elements are designed such that they cover the range from zero to 2π with suitable incremental steps. When designing a metasurface for a specific application, these resonating elements are arranged according to the designed phase modulation to reshape the phase front of propagating waves into the desired profiles. Conventionally, the phase modulation profile for reflected waves is designed based on the local height of the target object. Such design principle can be applied for the cloaking of any structural profiles and the virtual diffuser with smooth profiles. However, the reflection due to impedance mismatch of rapidly changing profiles needs to be considered in the design of virtual diffusers, in which case amplitude modulations and active elements are essential for the realization of the desired functions. These design principles of metasurfaces provide critical guidelines for their practical applications in architecture acoustics.

4. Angular momentum is an important degree of freedom for the control of acoustic wave propagation other than linear momentum associated with wave vector. With the abilities to modulate the wavefront of sound, metamaterials can be used to generate and modulate acoustic angular momentum. This acoustic angular momentum can be split into two parts: spin and orbital angular momentum (OAM). OAM of sound associates with the spatial distribution of the phase profile of sound waves, including the helical phase front of acoustic vortex beams and the circulation of energy flux in some phononic crystals. The acoustic vortex beams are well-studied sound waves carrying OAM generated by active phase arrays or phase modulating metamaterials that have many important applications such as particle rotation control and high speed communications. Different OAM carried by vortex beams can be characterized by topological charge indicating the quantity of the OAM. Acoustic OAM with different topological charges are orthogonal to each other and can serve as independent signal channels in a multiplexed single acoustic beam to enhance the information capacity

and communication speed. This information encoding degree of freedom is a spatial degree of freedom, which is independent from the frequency degree of freedom, enabling high speed acoustic communication especially for underwater applications where the available frequency band is limited and the carrier frequency is extremely low. Spin, on the other hand, characterizes the rotation of acoustic wave polarization defined as the local particle velocity vector of the field. In most cases, sound waves are longitudinal waves whose polarization always align with the propagation direction that never rotates and can be described by scalar pressure fields. Therefore, acoustic spin was considered to be impossible. However, one can observe the rotation of acoustic polarization in the interference of two perpendicular acoustic beams and acoustic evanescent waves, demonstrating the existence of acoustic spin. When a probe is placed in the interference of the two acoustic beams, a spin induced torque can be measured as a result of spin matter interaction. In acoustic evanescent waves, the propagation direction of sound is determined by the spin direction, resulting in spin dependent propagation. This newly discovered acoustic spin provide a novel control degree of freedom for the manipulation of acoustic wave propagation.

9.2 Recommendations for Future Works

This dissertation has accomplished the study of design and realization of acoustic metamaterials based on the resonances of unit cells. These acoustic metamaterials possess the capability to control the propagation of sound waves which is critical in the realization of acoustic illusion, subwavelength imaging, high-speed communications, and other important applications. However, the working frequency bandwidth of the metamaterials is usually narrow due to the resonance nature of the unit cells. This narrow frequency bandwidth limits their applications for scenarios where broadband effect is required such as architectural acoustics. Therefore, the application of acoustic metamaterials in these scenarios requires a new design principle that support the broadband feature. On the other hand, the narrow band property of the resonance based metamaterials makes them practically important in the cases where the modulation of single frequency is necessary like tomographic imaging, cell manipulations with surface acoustic waves (SAWs), etc. Here, several recommendations for future works are listed as follows.

1. For applications where broadband effect is critical like architectural acoustics, the acoustic metamaterials cannot be designed based on resonance effect. Other design principles that can work over a large frequency band should be developed for practical applications in these cases. Such designs may include active elements like the realization of the acoustic gain element in Chapter 5 whose frequency response can be adjusted by computer programs and digital control circuits in order to provide the broadband property. One can also consider to use the relation between different physical properties of materials to control the mass density and bulk modulus critical to

acoustic wave propagation. For example, the mass density and bulk modulus of water vary with temperature and salinity forming sound fixing and ranging (SOFAR) channel to guide sound waves propagating through the ocean. These other physical properties including temperature and salinity of the material can be judiciously designed to modulate the local mass density and bulk modulus in order to control the propagation of sound waves.

2. The narrow band effect of resonance based metamaterials can be applied to cases where single frequency modulation of acoustic waves is crucial. Such practical applications include tomographic imaging which is essential for biomedical imaging where single frequency ultrasound is used to image organs inside human and animal bodies. The subwavelength imaging property of metamaterials is important for the application of high resolution imaging using ultrasound. These metamaterials can also be applied to improve the performance of non-invasive surgeries using high intensity focused ultrasound (HIFU). Besides these biomedical applications, metamaterials can also be used to control cell motions in microfluidic channels. The radiation force of SAWs is widely used in microfluidic channels for cell diagnosis. The ability of metamaterials to control the acoustic wave propagation enables the control of the corresponding radiation force and cell motions in the microfluidic channels.

3. The capability of metamaterials to manipulate SAWs on on-chip devices can be crucial for the development of on-chip communication, memory, and computation. SAWs have been used in the development of qubits on on-chip devices because of their relatively shorter wavelengths compared with electromagnetic waves at the same frequency. The application of metamaterials in these devices will enhance the information storage capacity for quantum computing through these micro/nano-chips. In addition, the modulation of SAWs provides multiple orthogonal modes which can serve as independent information channels for on-chip communications.

Bibliography

1. Veselago, V. G. The electrodynamics of substances with simultaneously negative values of ϵ and μ. *Sov. Phys. Ups.* **10,** 509–514 (1968).
2. Pendry, J. B. Negative refraction makes a perfect lens. *Phys. Rev. Lett.* **85** (2000).
3. Liu, Z., Zhang, X., Mao, Y., Zhu, Y. Y., Yang, Z., Chan, C. T. & Sheng, P. Locally resonant sonic materials. *Science* **289,** 1734–1736 (2000).
4. Fang, N., Xi, D., Xu, J., Ambati, M., Srituravanich, W., Sun, C. & Zhang, X. Ultrasonic metamaterials with negative modulus. *Nature Mater.* **5,** 452–456 (2006).
5. Lee, S. H., Park, C. M., Seo, Y. M., Wang, Z. G. & Kim, C. K. Composite acoustic medium with simultaneously negative density and modulus. *Phys. Rev. Lett.* **104,** 054301 (2010).
6. Brunet, T., Merlin, A., Mascaro, B., Zimny, K., Leng, J., Poncelet, O., Aristegui, C. & Mondain-Monval, O. Soft 3D acoustic metamaterial with negative index. *Nature Mater.* **14,** 384–388 (2015).
7. Li, J., Fok, L., Yin, X., Bartal, G. & Zhang, X. Experimental demonstration of an acoustic magnifying hyperlens. *Nature Mater.* **8,** 931–934 (2009).
8. Zhu, J., Christensen, J., Jung, J., Martin-Moreno, L., Yin, X., Fok, L., Zhang, X. & Garcia-Vidal, F. J. A holey-structured metamaterial for deep-subwavelength imaging. *Nature Phys.* **7,** 52–55 (2010).
9. Lemoult, F., Fink, M. & Lerosey, G. Acoustic resonators for far-field control of sound on a subwavelength scale. *Phys. Rev. Lett.* **107,** 064301 (2011).
10. Engheta, N. Pursuing near-zero response. *Science* **340,** 286–287 (2013).
11. Zheng, L.-Y., Wu, Y., Ni, X., Chen, Z.-G., Lu, M.-H. & Chen, Y.-F. Acoustic cloaking by a near-zero-index phononic crystal. *Appl. Phys. Lett.* **104,** 161904 (2014).
12. Gu, Y., Cheng, Y., Wang, J. & Liu, X. Controlling sound transmission with density-near-zero acoustic membrane network. *J. Appl. Phys.* **118,** 024505 (2015).
13. Liu, F., Huang, X. & Chan, C. T. Dirac cones at $\mathbf{k} = 0$ in acoustic crystals and zero refractive index acoustic materials. *Appl. Phys. Lett.* **100,** 071911 (2012).
14. Dubois, M., Shi, C., Zhu, X., Wang, Y. & Zhang, X. Observation of acoustic Dirac-like cone and double zero refractive index. *Nature Comm.* **8,** 14871 (2017).

15. Chen, H. & Chan, C. T. Acoustic cloaking and transformation acoustics. *J. Phys. D Appl. Phys.* **43,** 113001 (2010).

16. Zhang, S., Xia, C. & Fang, N. Broadband acoustic cloak for ultrasound waves. *Phys. Rev. Lett.* **106,** 024301 (2011).

17. Popa, B.-I., Zigoneanu, L. & Cummer, S. A. Experimental acoustic ground cloak in air. *Phys. Rev. Lett.* **106,** 253901 (2011).

18. Zigoneanu, L., Popa, B.-I. & Cummer, S. A. Three-dimensional broadband omnidirectional acoustic ground cloak. *Nature Mater.* **13,** 352–355 (2014).

19. Li, Y., Liang, B., Tao, X., Zhu, X., Zou, X. & Cheng, J. Acoustic focusing by coiling up space. *Appl. Phys. Lett.* **101,** 233508 (2012).

20. Xie, Y., Wang, W., Chen, H., Konneker, A., Popa, B.-I. & Cummer, S. A. Wavefront modulation and subwavelength diffractive acoustics with an acoustic metasurface. *Nature Comm.* **5,** 5553 (2014).

21. Ma, G., Yang, M., Xiao, S., Yang, Z. & Sheng, P. Acoustic metasurface with hybrid resonances. *Nature Mater.* **13,** 873–878 (2014).

22. Faure, C., Richoux, O., Felix, S. & Pagneux, V. Experiments on metasurface carpet cloaking for audible acoustics. *Appl. Phys. Lett.* **108,** 064103 (2016).

23. Dubois, M., Shi, C., Wang, Y. & Zhang, X. A thin and conformal metasurface for illusion acoustics of rapidly changing profiles. *Appl. Phys. Lett.* **110,** 151902 (2017).

24. Fleury, R., Sounas, D. L., Sieck, C. F., Haberman, M. R. & Alu, A. Sound isolation and giant linear nonreciprocity in a compact acoustic circulator. *Science* **343,** 516–519 (2014).

25. Popa, B.-I. & Cummer, S. A. Non-reciprocal and highly nonlinear active acoustic metamaterials. *Nature Comm.* **5,** 3398 (2014).

26. Zhu, X., Ramezani, H., Shi, C., Zhu, J. & Zhang, X. PT-symmetric acoustics. *Phys. Rev. X* **4,** 031042 (2014).

27. Fleury, R., Sounas, D. & Alu, A. An invisible acoustic sensor based on parity-time symmetry. *Nature Comm.* **6,** 5905 (2015).

28. Shi, C., Dubois, M., Chen, Y., Cheng, L., Ramezani, H., Wang, Y. & Zhang, X. Accessing the exceptional points of parity-time symmetric acoustics. *Nature Comm.* **7,** 11110 (2016).

29. Shi, C., Dubois, M., Wang, Y. & Zhang, X. High-speed acoustic communication by multiplexing orbital angular momentum. *PNAS* **114,** 7250–7253 (2017).

30. Kaina, N., Lemoult, F., Fink, M. & Lerosey, G. Negative refractive index and acoustic superlens from multiple scattering in single negative metamaterials. *Nature* **525,** 77–81 (2015).

31. Ding, Y., Liu, Z., Qiu, C. & Shi, J. Metamaterial with simultaneously negative bulk modulus and mass density. *Phys. Rev. Lett.* **99,** 093904 (2007).

32. Zhu, X., Liang, B., Kan, W., Zou, X. & Cheng, J. Acoustic cloaking by a superlens with single-negative materials. *Phys. Rev. Lett.* **106,** 014301 (2011).

33. Zhang, S., Yin, L. & Fang, N. Focusing ultrasound with an acoustic metamaterial network. *Phys. Rev. Lett.* **102,** 194301 (2009).

34. Christensen, J. & de Abajo, F. J. G. Anisotropic metamaterials for full control of acoustic waves. *Phys. Rev. Lett.* **108,** 124301 (2012).

35. Chen, Y., Liu, H., Reilly, M., Bae, H. & Yu, M. Enhanced acoustic sensing through wave compression and pressure amplification in anisotropic metamaterials. *Nature Comm.* **5,** 5247 (2014).

36. Bongard, F., Lissek, H. & Mosig, J. R. Acoustic transmission line metamaterial with negative/zero/positive refractive index. *Phys. Rev. B* **82,** 094302 (2010).

37. Liang, Z. & Li, J. Extreme acoustic metamaterial by coiling up space. *Phys. Rev. Lett.* **118,** 114301 (2012).

38. Liang, Z., Feng, T., Lok, S., Liu, F., Ng, K. B., Chan, C. H., Wang, J., Han, S., Lee, S. & Li, J. Space-coiling metamaterials with double negative and conical dispersion. *Sci. Rep.* **3,** 1614 (2013).

39. Xie, Y., Popa, B.-I., Zigoneanu, L. & Cummer, S. A. Measurement of broadband negative index with space-coiling acoustic metamaterials. *Phys. Rev. Lett.* **110,** 175501 (2013).

40. Silveirinha, M. G. & Engheta, N. Tunneling of electromagnetic energy through subwavelength channels and bends using ϵ-near-zero materials. *Phys. Rev. Lett.* **97,** 157402 (2006).

41. Edwards, B., Alu, A., Young, M. E., Silveirinha, M. G. & Engheta, N. Experimental verification of epsilon-near-zero metamaterial coupling and energy squeezing using a microwave waveguide. *Phys. Rev. Lett.* **100,** 033903 (2008).

42. Cummer, S. A., Christensen, J. & Alu, A. Controlling sound with acoustic metamaterials. *Nature Rev. Mater.* **1,** 16001 (2016).

43. Fleury, R. & Alu, A. Extraordinary sound transmission through density-near-zero ultranarrow channel. *Phys. Rev. Lett.* **111,** 055501 (2013).

44. Huang, X., Lai, Y., Hang, Z. H., Zheng, H. & Chan, C. T. Dirac cones induced by accidental degeneracy in photonic crystals and zero-refractive-index materials. *Nature Mater.* **10,** 582–586 (2011).

45. Moitra, P., Yang, Y., Anderson, Z., Kravchenko, I. I., Briggs, D. P. & Valentine, J. Realization of an all-dielectric zero-index optical metamaterial. *Nature Photon.* **7,** 791–795 (2013).

46. Li, Y., Kita, S., Munoz, P., Reshef, O., Vulis, D. I., Yin, M., Loncar, M. & Mazur, E. On-chip zero-index metamaterials. *Nature Photon.* **9,** 738–742 (2015).

47. Cheng, Y., Zhou, C., Yuan, B. G., Wu, D. J., Wei, Q. & Liu, X. J. Ultra-sparse metasurface for high reflection of low frequency sound based on artificial Mie resonances. *Nature Mater.* **14,** 1013–1019 (2015).

48. Ward, G. P., Lovelock, R. K., Murray, A. R. J., Hibbins, A. P., Sambles, J. R. & Smith, J. D. Boundary-layer effects on acoustic transmission through narrow slit cavitites. *Phys. Rev. Lett.* **115,** 044302 (2015).

49. Montalda, G., Tanter, M., Bercoff, J., Benech, N. & Fink, M. Coherent plane-wave compounding for very high frame rate ultrasonography and transient elastography. *IEEE Trans. on U. F. F. C.* **56,** 489–506 (2009).

50. Alu, A., Silveirinha, M. G., Salandrino, A. & Engheta, N. Epsilon-near-zero metamaterials and electromagnetic sources: Tailoring the radiation phase pattern. *Phys. Rev. B* **75,** 155410 (2007).

51. Jing, Y., Xu, J. & Fang, N. X. Numerical study of a near-zero-index acoustic metamaterial. *Phys. Lett. A* **376,** 2834–2837 (2012).

52. Fokin, V., Ambati, M., Sun, C. & Zhang, X. Method for retrieving effective properties of locally resonant acoustic metamaterials. *Phys. Rev. B* **76,** 14432 (2007).

53. Kushwaha, M. S., Halevi, P., Martinez, G., Dobrzynski, L. & Djafari-Rouhani, B. Theory of acoustic band structure of periodic elastic composites. *Phys. Rev. B* **49,** 2313–2322 (1994).

54. Martinez-Sala, R., Sancho, J., Sanchez, J. V., Gomez, V., Llinares, J. & Meseguer, F. Sound-attenuation by sculpture. *Nature* **378,** 241–241 (1995).

55. Sigalas, M. & Economou, E. N. Band structure of elastic waves in two dimensional systems. *Solid State Comm.* **86,** 141–143 (1993).

56. Lu, M.-H., Zhang, C., Feng, L., Zhao, J., Chen, Y.-F., Mao, Y.-W., Zi, J., Zhu, Y.-Y., Zhu, S.-N. & Ming, N.-B. Negative birefraction of acoustic waves in a sonic crystal. *Nature Mater.* **6,** 744–748 (2007).

57. Yang, S., Page, J. H., Liu, Z., Cowan, M. L., Chan, C. T. & Sheng, P. Ultrasound tunneling through 3D phononic crystals. *Phys. Rev. Lett.* **88,** 104301 (2002).

58. Condat, C. A. & Kirkpatrick, T. R. Resonant scattering and Anderson localization of acoustic waves. *Phys. Rev. B* **36,** 6782–6793 (1987).

59. Ruter, C. E., Makris, K. G., El-Ganainy, R., Christodoulides, D. N., Segev, M. & Kip, D. Observation of parity-time symmetry in optics. *Nature Phys.* **6,** 192–195 (2010).

60. Regensburger, A., Bersch, C., Miri, M.-A., Onishchukov, G., Christodoulides, D. N. & Peschel, U. Parity-time synthetic photonic lattices. *Nature* **488,** 167–171 (2010).

61. Peng, B., Ozdemir, S. K., Lei, F., Monifi, F., Gianfreda, M., Long, G. L., Fan, S., Nori, F., Bender, C. M. & Yang, L. Parity-time-symmetric whispering-gallery microcavities. *Nature Phys.* **10,** 394–398 (2014).

62. Feng, L., Xu, Y.-L., Fegadolli, W. S., Lu, M.-H., Oliveira, J. E. B., Almeida, V. R., Chen, Y.-F. & Scherer, A. Experimental demonstration of a unidirectional reflectionless parity-time metamaterial at optical frequencies. *Nature Mater.* **12,** 108–113 (2013).

63. Schindler, J., Li, A., Zheng, M. C., Ellis, F. M. & Kottos, T. Experimental study of active LRC circuits with PT symmetries. *Phys. Rev. A* **84,** 040101 (2011).

64. Ramezani, H., Schindler, J., Ellis, F. M., Gunther, U. & Kottos, T. Bypassing the bandwidth theorem with PT symmetry. *Phys. Rev. A* **85,** 062122 (2012).

65. Makris, K. G., El-Ganainy, R., Christodoulides, D. N. & Musslimani, Z. H. Beam Dynamics in PT Symmetric Optical Lattices. *Phys. Rev. Lett.* **100,** 103904 (2008).

66. Lin, Z., Ramezani, H., Elchelkraut, T., Kottos, T., Cao, H. & Christodoulides, D. N. Unidirectional invisibility induced by PT-symmetric periodic structures. *Phys. Rev. Lett.* **106,** 213901 (2011).

67. Zhu, X., Feng, L., Zhang, P., Yin, X. & Zhang, X. One-way invisible cloak using parity-time symmetric transformation optics. *Opt. Lett.* **38,** 2821–2824 (2013).

68. Ramezani, H., Christodoulides, D. N., Kovanis, V., Vitebskiy, I. & Kottos, T. PT-symmetric talbot effects. *Phys. Rev. Lett.* **109,** 033902 (2012).

69. Ramezani, H., Kottos, T., Kovanis, V. & Christodoulides, D. N. Exceptional-point dynamics in photonic honeycomb lattices with PT symmetry. *Phys. Rev. A* **85,** 013818 (2012).

70. Bender, N., Factor, S., Bodyfelt, J. D., Ramezani, H., Christodoulides, D. N., Ellis, F. M. & Kottos, T. Observation of asymmetric transport in structures with active nonlinearities. *Phys. Rev. Lett.* **110,** 234101 (2013).

71. Chong, Y. D., Ge, L., Cao, H. & Stone, A. D. Coherent perfect absorbers: time-reversed lasers. *Phys. Rev. Lett.* **105,** 053901 (2010).

72. Schindler, J., Lin, Z., Lee, J. M., Ramezani, H., Ellis, F. M. & Kottos, T. PT symmetric electronics. *J. Phys. A* **45,** 444029 (2012).

73. Ge, L., Chong, Y. D. & Stone, A. D. Conservation relations and anisotropic transmission resonances in one-dimensional PT-symmetric photonic heterostructures. *Phys. Rev. A* **85,** 023802 (2012).

74. Lin, Z., Schindler, J., Ellis, F. M. & Kottos, T. Experimental observation of the dual behavior of PT-symmetric scattering. *Phys. Rev. A* **85,** 050101 (2012).

75. Leonhardt, U. Optical conformal mapping. *Science* **312,** 1777–1780 (2006).

76. Pendry, J. B., Schurig, D. & Smith, D. R. Controlling electromagnetic fields. *Science* **312,** 1780–1782 (2006).

77. Cheng, Y. & Liu, X. J. Resonance effects in broadband acoustic cloak with multilayered homogeneous isotropic materials. *Appl. Phys. Lett.* **93,** 071903 (2008).

78. Kundtz, N., Gaultney, D. & Smith, D. R. Scattering cross-section of a transformation optics-based metamaterial cloak. *New J. Phys.* **12,** 043039 (2010).

79. Yu, Z. & Fan, S. Complete optical isolation created by indirect interband photonic transitions. *Nature Photon.* **3,** 91–94 (2008).

80. Kang, M. S., Butsch, A. & Russell, P. S. J. Reconfigurable light-driven opto-acoustic isolators in photonic crystal fiber. *Nature Photon.* **5,** 549–553 (2011).

81. Manipatruni, S., Robinson, J. T. & Lipson, M. Optical nonreciprocity in optomechanical structures. *Phys. Rev. Lett.* **102,** 213903 (2009).

82. Li, X.-F., Ni, X., Feng, L., Lu, M.-H., He, C. & Chen, Y.-F. Tunable unidirectional sound propagation through a sonic-crystal-based acoustic diode. *Phys. Rev. Lett.* **106,** 084301 (2011).

83. Liang, B., Guo, X. S., Tu, J., Zhang, D. & Cheng, J. An acoustic rectifier. *Nature Mater.* **9,** 989–992 (2010).

84. Boechler, N., Theocharis, G. & Daraio, C. Bifurcation-based acoustic switching and rectification. *Nature Mater.* **10,** 665–668 (2011).

85. Chang, L., Jiang, X., Hua, S., Yang, C., Wen, J., Jiang, L., Li, G., Wang, G. & Xiao, M. Parity-time symmetry and variable optical isolation in active-passive-coupled resonators. *Nature Photon.* **8,** 524–529 (2014).

86. Nazari, F., Bender, N., Ramezani, H., Marovvej-Farshi, M. K., Chistodoulides, D. N. & Kottos, T. Optical isolation via PT-symmetric nonlinear Fano resonances. *Opt. Exp.* **22,** 9574 (2014).

87. Ramezani, H., Li, H. K., Wang, Y. & Zhang, X. Unidirectional spectral singularities. *Phys. Rev. Lett.* **113,** 263905 (2014).

88. Fleury, R., Sounas, D. & Alu, A. An invisible acoustic sensor based on parity-time symmetry. *Nature Comm.* **6,** 5905 (2014).

89. Peng, B., Ozdemir, S. K., Rotter, S., Yilmaz, H., Liertzer, M., Monifi, F., Bender, C. M., Nori, F. & Yang, L. Loss-induced suppression and revival of lasing. *Science* **346,** 328–332 (2014).

90. Feng, L., Wong, Z. J., Ma, R. M., Wang, Y. & Zhang, X. Single-mode laser by parity-time symmetry breaking. *Science* **346,** 972–975 (2014).

91. Hodaei, H., Miri, M. A., Heinrich, M., Christodoulides, D. N. & Khajavikhan, M. Parity-time-symmetric microring lasers. *Science* **346,** 975–978 (2014).

92. Bender, C. M. & Boettcher, S. Real spectra in non-Hermitian Hamiltonians having PT symmetry. *Phys. Rev. Lett.* **80,** 5243–5246 (1998).

93. Bender, C. M., Boettcher, S. & Meisinger, R. N. PT-symmetric quantum mechanics. *J. Math. Phys.* **40,** 2201–2229 (1999).

94. Wan, W., Chong, Y. D., Ge, L., Noh, H., Stone, A. D. & Cao, H. Time-reversed lasing and interferometric control of absorption. *Science* **331,** 889–892 (2011).

95. Chong, Y. D., Ge, L. & Stone, A. D. PT-symmetry breaking and laser absorber modes in optical scattering systems. *Phys. Rev. Lett.* **106,** 093902 (2011).

96. Longhi, S. PT-symmetric laser absorber. *Phys. Rev. A* **82,** 031801 (2010).

97. Popar, B.-I., Zigoneanu, L. & Cummer, S. A. Tunable active acoustic metamaterials. *Phys. Rev. B* **88,** 024303 (2013).

98. Rathsam, J. & Wang, L. M. A review of diffuse reflections in architecture acoustics. *Build. Integ. Sol.* **190,** 23 (2006).

99. Cox, T. J. & D'Antonio, P. *A review of diffuse reflections in architecture acoustics* 2nd edition (Taylor and Francis Group, New York, NY, USA, 2009).

100. Yu, N., Genevet, P., Kats, M. A., Aieta, F., Tetienne, J.-P., Capasso, F. & Gaburro, Z. Light propagation with phase discontinuities: generalized laws of reflection and refraction. *Science* **334,** 333–337 (2011).

101. Ni, X., Emani, N. K., Kildishev, A. V., Boltasseva, A. & Shalaev, V. M. Broadband light bending with plasmonic nanoantennas. *Science* **335,** 427–427 (2012).

102. Meinzer, N., Barnes, W. L. & Hooper, I. R. Plasmonic meta-atoms and metasurfaces. *Nature Photon.* **8,** 889–898 (2014).

103. Ni, X., Wong, Z. J., Mrejen, M., Wang, Y. & Zhang, X. An ultrathin invisibility skin cloak for visible light. *Science* **349,** 1310–1314 (2015).

104. Lin, D., Fan, P., Hasman, E. & Brongersma, M. L. Dielectric gradient metasurface optical elements. *Science* **345,** 298–302 (2014).

105. Khorasaninejad, M., Chen, W. T., Devlin, R. C., Oh, J., Zhu, A. Y. & Capasso, F. Metalenses at visible wavelengths: diffraction-limited focusing and subwavelength resolution imaging. *Science* **352,** 1190–1194 (2014).

106. Ni, X., Kildishev, A. V. & Shalaev, V. M. Metasurface holograms for visible light. *Nature Comm.* **4,** 2807 (2013).

107. Huang, L., Chen, X., Muhlenbern, H., Zhang, H., Chen, S., Bai, B., Tan, Q., Jin, G., Cheah, K.-W., Qiu, C.-W., Li, J., Zentgraf, T. & Zhang, S. Three-dimensional optical holography using a plasmonic metasurface. *Nature Comm.* **4,** 2808 (2013).

108. Zheng, G., Muhlenbern, H., Kenney, M., Li, G., Zentgraf, T. & Zhang, S. Metasurface holograms reaching 80% efficiency. *Nature Photon.* **10,** 308–312 (2015).

109. Maurya, S. K., Pandey, A., Shukla, S. & Saxena, S. Double negativity in 3D coiling metamaterials. *Sci. Rep.* **6,** 33683 (2016).

110. Li, Y., Liang, B., Zou, X. & Cheng, J. Extraordinary acoustic transmission through ultrathin acoustic metamaterials by coiling up space. *Appl. Phys. Lett.* **103,** 063509 (2013).

111. Li, Y., Jiang, X., Li, R., Liang, B., Zou, X. & Cheng, J. Experimental realization of full control of reflected waves with subwavelength acoustic metasurfaces. *Phys. Rev. Appl.* **2,** 064002 (2014).

112. Shen, C., Xie, Y., Li, J., Cummer, S. A. & Jing, Y. Asymmetric acoustic transmission through near-zero-index and gradient-index metasurfaces. *Appl. Phys. Lett.* **108,** 223502 (2016).

113. Song, K., Kim, J., Hur, S., Kwak, J.-H., Lee, S.-H. & Kim, T. Directional reflective surface formed via gradient-impeding acoustic meta-surfaces. *Sci. Rep.* **6,** 32300 (2016).

114. Yang, M., Ma, G., Yang, Z. & Sheng, P. Coupled membranes with doubly negative mass density and bulk modulus. *Phys. Rev. Lett.* **110,** 134301 (2013).

115. Zhai, S., Cheng, H., Ding, C., Li, L., Shen, F., Luo, C. & Zhao, X. Ultrathin skin cloaks with metasurfaces for audible sound. *J. Phys. D: Appl. Phys.* **49,** 225302 (2016).

116. Esfahlani, H., Karkar, S., Lissek, H. & Mossig, J. R. Acoustic carpet cloak based on an ultrathin metasurface. *Phys. Rev. B* **94,** 014302 (2016).

117. Xie, Y., Shen, C., Wang, W., Li, J., Suo, D., Popa, B.-I., Jing, Y. & Cummer, S. A. Acoustic holographic rendering with two-dimensional metamaterial based passive phased array. *Sci. Rep.* **6,** 35437 (2016).

118. Melde, K., Mark, A. G., Qiu, T. & Fischer, P. Holograms for acoustics. *Nature* **537,** 518–522 (2016).

119. Bass, H. E., Sutherland, L. C. & Zuckerwar, A. J. Atmospheric absorption of sound: update. *J. Acoust. Soc. Am.* **88,** 2019 (1990).

120. Hale, G. M. & Querry, M. R. Optical constants of water in the 200 nm to 200 μm wavelength region. *Appl. Opt.* **12,** 555–563 (1973).

121. Quickenden, T. I. & Irvine, J. A. The ultraviolet absorption spectrum of liquid water. *J. Chem. Phys.* **72,** 4416 (1980).

122. Warren, S. G. Optical-constants of ice from the ultraviolet to the microwave. *Appl. Opt.* **23,** 1206–1225 (1984).

123. Buiteveld, H., Hakvoort, J. H. M. & Donze, M. Optical properties of pure water. *Proc. SPIE Ocean Opt. XII* **2285,** 174 (1994).

124. Funk, C. J. Multiple scattering calculations of light propagation in ocean water. *Appl. Opt.* **12,** 310–313 (1973).

125. Mullen, L., Laux, A. & Cochenour, B. Propagation of modulated light in water: implications for imaging and communications systems. *Appl. Opt.* **14,** 2607–2612 (2009).

126. Mullen, L., Alley, D. & Cochenour, B. Investigation of the effect of scattering agent and scattering albedo on modulated light propagation in water. *Appl. Opt.* **50,** 1396–1404 (2011).

127. Friedman, N. *The naval institute guide to world naval weapons systems* (Naval Institute Press, Annapolis, MD, USA, 2006).

128. Basagni, S., Conti, M., Giodano, S. & Stojmenovic, I. *Mobile ad hoc networking: cutting edge directions* 2nd edition (Wiley, Hoboken, NJ, USA, 2013).

129. Dhanak, M. R. & Xiros, N. I. *Springer handbook of ocean engineering* (Springer, New York, NY, USA, 2016).

130. Stojanovic, M. Recent advances in high-speed underwater communications. *IEEE J. Ocean. Eng.* **21,** 125–136 (2002).

131. Freitag, L., Stojanovic, Y. M., Grund, M. & Singh, I. Acoustic communications for regional undersea observatories. *In Proc. Oceanology Intl.* (2002).

132. Song, H. C. & Hodgkiss, W. S. Efficient use of bandwidth for underwater acoustic communication. *J. Acoust. Soc. Am.* **134,** 905 (2013).

133. Wang, J., Yang, J.-Y., Fazal, I. M., Ahmed, N., Yan, Y., Huang, H., Ren, Y., Yue, Y., Dolinar, S., Tur, M. & Willner, A. E. Terabit free-space data transmission employing orbital angular momentum multiplexing. *Nature Photon.* **6,** 488–496 (2012).

134. Bozinovic, N., Yue, Y., Ren, Y., Tur, M., Kristensen, P., Huang, H., Willner, A. E. & Ramachandran, S. Terabit-scale orbital angular momentum mode division multiplexing in fibers. *Science* **340,** 1545–1548 (2013).

135. Yan, Y., Xie, G., Lavery, M. P. J., Huang, H., Ahmed, N., Bao, C., Ren, Y., Cao, Y., Li, L., Zhao, Z., Molisch, A. F., Tur, M., Padgett, M. J. & Willner, A. E. High-capacity millimetre-wave communications with orbital angular momentum multiplexing. *Nature Comm.* **5,** 4876 (2014).

136. Ren, H., Li, X., Zhang, Q. & Gu, M. On-chip noninterference angular momentum multiplexing of broadband light. *Science* **352,** 805–809 (2016).

137. Miao, G., Zander, J., Sung, K. W. & Slimane, S. B. *Fundamentals of mobile data networks* (Cambridge University Press, Cambridge, UK, 2016).

138. Maguid, E., Yulevich, I., Veksler, D., Kleiner, V., Brongersma, M. L. & Hasman, E. Photonic spin-controlled multifunctional shared-aperture antenna array. *Science* **352,** 1202–1206 (2016).

139. Hefner, B. T. & Marston, P. L. An acoustical helicoidal wave transducer with applications for alignment of ultrasonic and underwater systems. *J. Acoust. Soc. Am.* **106,** 3313–3316 (1999).

140. Brunet, T., Thomas, J.-L., Machiano, R. & Coulouvrat, F. Experimental observation of azimuthal shock waves on nonlinear acoustic vortices. *New J. Phys.* **11,** 013002 (2009).

141. Jiang, X., Li, Y., Liang, B., Cheng, J.-C. & Zhang, L. Convert acoustic resonances to orbital angular momentum. *Phys. Rev. Lett.* **117,** 034301 (2016).

142. Jiang, X., Zhao, J., Liu, S.-L., Liang, B., Zou, X.-Y., Yang, J. & Cheng, J.-C. Broadband and stable acoustic vortex emitter with multi-arm coiling slits. *Appl. Phys. Lett.* **108,** 203510 (2016).

143. Naify, C. J., Rodhe, C. A., Martin, T. P., Nicholas, M., Guild, M. D. & Orris, G. J. Generation of topologically diverse acoustic vortex beams using a compact metamaterial aperture. *Appl. Phys. Lett.* **108,** 223503 (2016).

144. Ye, L., Qiu, C., Lu, J., Tang, K., Jia, H., Ke, M., Peng, S. & Liu, Z. Making sound vortices by metasurfaces. *AIP Adv.* **6,** 085007 (2016).

145. Demore, C. E. M., Yang, Z., Volovick, A., Cochran, S., MacDonald, M. P. & Spalding, G. C. Mechanical evidence of the orbital angular momentum to energy ratio of vortex beams. *Phys. Rev. Lett.* **108,** 194301 (2012).

146. Anhauser, A., Wunenburger, R. & Brasselet, E. Acoustic rotational manipulation using orbital angular momentum transfer. *Phys. Rev. Lett.* **109,** 034301 (2012).

147. Hong, Z., Thomas, J.-L. & Drinkwater, B. W. Observation of orbital angular momentum transfer from Bessel-shaped acoustic vortices to diphasic liquid-microparticle mixture. *Phys. Rev. Lett.* **114,** 214301 (2015).

148. Marzo, A., Seah, S. A., Drinkwater, B. W., Sahoo, D. R., Long, B. & Subramanian, S. Holographic acoustic elements for manipulation of levitated objects. *Nature Comm.* **6,** 8661 (2015).

149. Baresch, D., Thomas, J.-L. & Marchiano, R. Observation of a single-beam gradient force acoustic trap for elastic particles: acoustical tweezers. *Phys. Rev. Lett.* **116,** 024301 (2016).

150. Lu, J., Qiu, C., Ke, M. & Liu, Z. Valley vortex states in sonic crystals. *Phys. Rev. Lett.* **116,** 093901 (2016).

151. Heegard, C. & Wicher, S. B. *Turbo coding* (Kluwer Academic Publisher, Norwell, MA, USA, 1999).

152. Nakazawa, M., Kikuchi, K. & Miyazaki, T. *High spectral density optical communication technologies* (Springer, Berlin Heidelberg, Germany, 2010).

153. Belinfante, F. J. On the spin angular momentum of mesons. *Physica* **6,** 887–898 (1939).

154. Ohanian, H. C. What is spin. *Am. J. Phys.* **54,** 500–505 (1986).

155. Belinfante, F. J. On the current and the density of the electric charge, the energy, the linear momentum and the angular momentum of arbitrary fields. *Physica* **7,** 449–474 (1940).

156. Andrews, D. L. & Babiker, M. *The angular momentum of light* (Cambridge University Press, Cambridge, UK, 2013).

157. Aiello, A., Banzer, P., Neugebauer, M. & Leuchs, G. From transverse angular momentum to photonic wheels. *Nature Photon.* **9,** 789–795 (2015).

158. Rodriguez-Fortuno, F. J., Marino, G., Ginzburg, P., O'Connor, D., Martinez, A., Wurtz, G. A. & Zayats, A. V. Near-field interference for the unidirectional excitation of electromagnetic guided mode. *Science* **340,** 328–330 (2013).

159. Petersen, J., Volz, J. & Rauschenbeutel, A. Chiral nanophotonic waveguide interface based on spin-orbital interaction of light. *Science* **346,** 67–71 (2014).

160. Bliokh, K. Y., Smirnova, D. & Nori, F. Quantum spin Hall effect of light. *Science* **348,** 1448–1451 (2015).

161. Lodahl, P., Mahmoondian, S., Stobbe, S., Rauschenbeutel, A., Schneeweiss, P., Volz, J., Pichler, H. & Zoller, P. Chiral quantum optics. *Nature* **541,** 473–480 (2017).

162. Shomroni, I., Rosenbrum, S., Lovsky, Y., Bechler, O., Guendelman, G. & Dayan, B. All-optical routing of single photons by a one-atom switch controlled by a single photon. *Science* **345,** 903–906 (2014).

163. Sollner, I., Mahmoodian, S., Hansen, S. L., Midolo, L., Javadi, A., Kirsanske, G., Pregnolato, T., El-Ella, H., Lee, E. H., Song, J. D., Stobbe, S. & Lodahl, P. Deterministic photon-emitter coupling in chiral photonic circuits. *Nature Nano.* **10,** 775–778 (2015).

164. Rosenblum, S., Bechler, O., Shomroni, I., Lovsky, Y., Guendelman, G. & Dayan, B. Extraction of a single photon from an optical pulse. *Nature Photon.* **10,** 19–22 (2016).

165. Scheucher, M., Hilico, A., Will, E., Volz, J. & Rauschenbeutel, A. Quantum optical circulator controlled by a single chirally coupled atom. *Science* **354,** 1577–1580 (2016).

166. Crocker, M. J. *Handbook of acoustics* (John Willey and Sons Inc., New York, NY, USA, 1998).

167. He, C., Ni, X., Ge, H., Sun, X.-C., Chen, Y.-B., Lu, M.-H., Liu, X.-P. & Chen, Y.-F. Acoustic topological insulator and robust one-way sound transport. *Nature Phys.* **12,** 1124–1129 (2016).

168. Zhang, Z., Wei, Q., Cheng, Y., Zhang, T., Wu, D. & Liu, X. Topological creation of acoustic pseudospin multipoles in flow-free symmetry-broken metamaterial lattice. *Phys. Rev. Lett.* **118,** 084303 (2017).

169. Li, F., Huang, X., Lu, J., Ma, J. & Liu, Z. Weyl points and Fermi arcs in a chiral phononic crystal. *Nature Phys.* **14,** 30–34 (2018).

170. Zhang, L. & Marston, P. L. Acoustic radiation torque and the conservation of angular momentum. *J. Acoust. Soc. Am.* **129,** 1679–1680 (2011).

171. Zhao, R., Manjavacas, A., de Abajo, F. J. G. & Pendry, J. B. Rotational quantum friction. *Phys. Rev. Lett.* **109,** 123604 (2012).

172. Cavendish, H. Experiments to determine the density of the Earth. *Philosophical Trans. Royal Soc. London* **88,** 469–526 (1798).

173. Zhu, J., Chen, Y., Zhu, X., Carcia-Vidal, F. J., Yin, X., Zhang, W. & Zhang, X. Acoustic rainbow trapping. *Sci. Rep.* **3,** 1728 (2013).